https://ntrs.nasa.gov/search.jsp?R=19700018280 2020-03-12T02:09:41+00:00Z

N 70 27590

NASA CR-54858

SRI-R-25

# REVIEW OF METEOROID-BUMPER INTERACTION STUDIES AT McGILL UNIVERSITY

by

W. H. FRIEND, C. L. MURPHY and P. S. GOUGH

Prepared for

NATIONAL AERONAUTICS AND SPACE ADMINISTRATION

September 1969

Contract NAS 3-7946

CASE FILE COPY

SPACE RESEARCH INSTITUTE
2055 Peel Street Suite 175
Montreal, Canada

NASA CR-54858

SRI-R-25

# REVIEW OF METEOROID-BUMPER INTERACTION STUDIES AT McGILL UNIVERSITY

by

W.H. FRIEND, C.L. MURPHY and P.S. GOUGH

Prepared for

NATIONAL AERONAUTICS AND SPACE ADMINISTRATION

September 1969

Contract NAS3-7946

SPACE RESEARCH INSTITUTE

2055 Peel Street, Suite 175

Montreal, Canada

## FOREWORD

This report summarizes the continuing research program at the Space Research Institute* in hypervelocity impact and meteoroid-bumper interaction phenomena, conducted during the period December 1965 through June 1967. The program was sponsored by the National Aeronautics and Space Administration under contract NAS3-7946 "Meteoroid-Bumper Interaction Program". The technical monitor for the program was Mr. Gordon T. Smith of NASA Lewis Research Center, Liquid Rocket Technology Branch.

The research program included both theoretical and experimental investigations of meteoroid-bumper interaction pheonomena, and, as has been the practice under previous contracts (NAS3-4190, NASW-615 and NAS5.664), the theoretical programs have been published separately in topical reports. The principal results of the theoretical program are summarized without detailed analysis; the experimental program is reviewed in more detail. Both theoretical and experimental phases of this program are continuations and extensions of work commenced under contract NAS3-4190 and reviewed in the final report of that contract (NASA CR-54857).

The authors are indebted to Dr. G.V. Bull, for his continued support and guidance throughout the program, to Mr. I. Shanfield for his assistance in the experimental work and to Mr. W.A. Watkins for his assistance in preparing this report.

.....

*This work was conducted at the Space Research Institute during its affiliation with McGill University. A continuation research program is currently in progress at SRI(Que) Inc. under contract NAS3-10229. The authors wish to express their thanks to the directors of SRI(Que) Inc. for making its facilities and personnel available for the preparation of this report.

SUMMARY

Two theoretical programs and an experimental investigation of meteoroid-bumper impact, debris cloud expansion, and second surface pressure loading have been conducted. Particular emphasis has been placed on developing a firm theoretical and experimental base from which a realistic projection to the meteoroid regime can be made.

On of the theoretical models, the strip model, has been developed to the stage wherein predictions of secondary surface loadings from actual meteoroid-bumper interactions can be made for a realistic space mission. The second theoretical approach, based on finite difference solutions to the fundamental relations governing the impact process, has been restricted to a one-dimensional analysis of the processes involved in the region of the bumper and near the second surface. The experimental program covered a broad range of separate experiments, some to obtain experimental verification of assumptions made in the theoretical models, and others to obtain experimental data to be used as a basis for projection to the meteoroid regime. Specific areas investigated were bumper thickness effects, projectile shape effects, second surface pressure distribution for various impact conditions and bumper stand-off distances, shock Hugoniots for the impact materials utilized, shock decay data, secondary surface response, and a special study of the multiple skin or multifoil protection system.

Towards the latter part of the program, a modification to the normal thin sheet bumper was introduced in order to permit integration of the meteoroid bumper shield concept with the super insulation system proposed for cryogenic fuel storage tanks without upsetting the system thermal radiation balance. The scant experimental data available for the grid-bumper concept at the end of this contract was inadequate for the presentation of conclusive results. However, a possible improvement in protection capability was observed. The grid-bumper appeared to offer superior meteoroid defeating (vaporization) potential than an equivalent weight solid sheet bumper.

## TABLE OF CONTENTS


| | | Page |
|---|---|---|
| 1.0 | INTRODUCTION | 1 |
| 2.0 | RANGE AND INSTRUMENTATION DEVELOPMENT | 5 |
| | 2.1 Test Tankage System | 5 |
| | 2.2 Piezo Bar Gauge | 10 |
| 3.0 | EXPERIMENTAL TESTS AND ANALYSIS | 17 |
| | 3.1 Multifoil Witness Sheets | 17 |
| | 3.2 Bumper Thickness Effect | 36 |
| | 3.3 Impulse Loading on Secondary Surface | 44 |
| | 3.4 Bar and Disc Impacts | 55 |
| | 3.5 Pellet Shape Effects | 75 |
| 4.0 | THEORY | 78 |
| | 4.1 Impact Shock and Expansion States | 78 |
| | 4.2 Finite Difference Model | 95 |
| | 4.3 Strip Model | 115 |
| 5.0 | THE GRID BUMPER | 120 |
| 6.0 | CONCLUDING REMARKS | 130 |
| | REFERENCES | 132 |

## LIST OF FIGURES


| | | Page |
|---|---|---|
| 2.1a | Photograph of Swing Door on Impact Tank (closed) | 6 |
| 2.1b | Photograph of Swing Door on Impact Tank (open) | 6 |
| 2.2 | Photograph of Modified X-Ray Port | 7 |
| 2.3a | Drawing of Experimental X-Ray System | 8 |
| 2.3b | X-Ray Picture of Pellet Leaving Muzzle | 8 |
| 2.4a | Piezo-Bar Output Trace Shot 279 | 11 |
| 2.4b | Five-Frame STL Camera Sequence Shot 279 | 11 |
| 2.5 | Drawing of Piezo-Bar Gauge and Filter Probe | 13 |
| 2.6a | Piezo-Bar and Filter Probe Traces Shot 280 | 15 |
| 2.6b | Five-Frame STL Camera Sequence Shot 280 | 15 |
| 3.1a | Sketch of Multi-Foil Witness Sheets | 18 |
| 3.1b | Photograph of Multi-Foil Witness Sheets | 19 |
| 3.2a | Photographs of Bumper Shot 260 | 20 |
| 3.2b | Photographs of Multi-Foil Sheets Shot 260 | 20 |
| 3.2c-f | Photographs of Individual Aluminum Sheets Shot 260 | 21 |
| 3.3 | Photographs of Complete (Frames 1 to 70) B and W 192 Framing Camera Coverage of Shot 260 | 22-26 |
| 3.4 | Photographs of Frames 1 to 12, B and W 192 Framing Camera Coverage of Shot 269 | 27-29 |
| 3.5a | Five-Frame STL Camera Sequence Shot 253 | 30 |
| 3.5b | Five-Frame STL Camera Sequence Shot 269 | 30 |
| 3.6 | Piezo-Bar Traces for Spacings of 3, 6, 9 and 12 inches Shots 296, 297, 298 and 302 | 38 |
| 3.7 | Piezo-Bar Traces Showing Effect of Bumper Thickness Shots 104, 296, 306 and 311 | 39 |
| 3.8 | Theoretical Plot of Shocked Energy vs Impact Velocity | 41 |

| | | Page |
|---|---|---|
| 3.9 | Theoretical Plot of Shocked Energy Decay vs Distance Along Pellet | 42 |
| 3.10 | Theoretical Pellet Shock Decay by Interaction with One - Dimensional Axial Rarefaction Waves | 43 |
| 3.11 | Piezo-Bar Traces for Shots 299 to 300 | 45 |
| 3.12 | Drawing of Pressure Probe Locations in Secondary Surface | 47 |
| 3.13a | Piezo-Bar Traces for Off-Center Locations Shot 391 | 48 |
| 3.13b | Photographs of B and W 192 Coverage (Frames 1-39) Shot 391 | 49 |
| 3.14 | Carpet Plot of Pressure Distribution in Impact Cloud | 50 |
| 3.15 | Photographs of B and W 300 Coverage of a Pellet Impact on a Disc Shot | 56 |
| 3.16 | Photographs of B and W 300 Coverage of a Pellet Impact on a Bar Shot | 57 |
| 3.17 | Schematic Wave Diagram for Impact Process | 58 |
| 3.18 to 3.23 | Experimental Distance Time Diagrams for Shots 528, 529 533, 538, 539 and 544 | 59-64 |
| 3.24 | Non-Dimensional Shock Velocity and Escape Velocity vs Polytropic Exponent | 68 |
| 3.25 | Polytropic Exponent vs Impact Velocity | 72 |
| 3.26 | Hugoniot for Lexan | 73 |
| 3.27 | Shock Velocity vs Particle Velocity for Lexan | 74 |
| 3.28 | Piezo-Bar Traces Showing Shape Effects Shots 340, 341, 356, 364, 337 | 76 |
| 4.1 | Proportional Energy States during Impact | 82 |
| 4.2 | Distance-Time Shock and Expansion Wave Diagram | 83 |
| 4.3 | Non-Dimensional Escape Velocity vs Expansion $\gamma$ for Different Values of Shocked $\gamma$'s | 93 |
| 4.4 | One-Dimensional Wave Diagram of Impact Process | 97 |
| 4.5 | Pressure vs Ratio of Mass of Pellet Shocked to Mass of Bumper | 111 |

| | | Page |
|---|---|---|
| 4.6 | Comparison of Pressure at a Secondary Surface with that of the Undisturbed Flow | 114 |
| 4.7 | Strip Model Meteoroid Predictions of Pressure, Density and Velocity vs Axial Distance for Three Time Increments after Impact | 118 |
| 5.1 | Grid Bumper Characteristics Equivalent to a .001" Lead Sheet Bumper | 128 |
| 5.2 | Photographs of B and W Coverage of Impact of Lexan Projectile Impacting on Lead Wire Grid | 129 |

## LIST OF SYMBOLS

| | |
|---|---|
| $a$ | isentropic sound speed |
| $c$ | isentropic sound speed |
| $c_p$, $c_v$ | specific heats at constant pressure, volume |
| $e$ | specific internal energy |
| $\ell$ | pellet length |
| $p$ | pressure |
| $q$ | artificial viscosity |
| $R$ | universal gas constant |
| $r$ | radial coordinate |
| Rp, Rb | pellet and bumper rarefaction waves |
| $\overleftarrow{Sp}$, $\overrightarrow{Sb}$ | pellet and bumper shock waves |
| $u$ | particle velocity |
| $V$ | pellet velocity |
| $w$ | shock velocity |
| $x$ | axial coordinate |
| $\alpha, \beta$ | constants in Gaussian representation of pressure |
| $\gamma$ | polytropic gas exponent |
| $\delta$ | bumper thickness |
| $\Delta x, \Delta t$ | space & time increments |
| $\Delta$ | shock thickness |
| $\nu$ | smoothing coefficient |
| $\rho$ | density |

## LIST OF SYMBOLS

Subscripts

| | |
|---|---|
| B | bumper |
| e | expansion |
| es | escape |
| i | increment |
| 0 | unshocked or initial |
| p | pellet |
| s | compression or shocked state |

## 1.0 INTRODUCTION

A continuing hypervelocity impact research program, directed towards meteoroid protection systems for space vehicles, has been carried out since 1961 at McGill University, the Space Research Institute of McGill University, and presently the Space Research Institute (Quebec) Inc.

The previous final report (Reference 1) was submitted in August, 1966 and covers the period June 15, 1964 to September 15, 1965 under contract NAS3-4190. The early development of the impact research from the spring of 1961 to the spring of 1964 is outlined in the introduction of this report (Reference 1). The report presented here covers the period December, 1965 to June, 1967 under contract NAS3-7946.

During the contract period some modifications were made to the firing range facilities and instrumentation (Section 2.0). Specifically, the range vacuum chambers were modified to meet the specific objectives of the program and to facilitate installation of instrumentation. The piezo-bar pressure probe was improved by adding a by-pass filter to eliminate electronic interference due to ionization of the gas cloud.

A number of experimental test series were carried out in order to understand the impact phenomena, and to test space vehicle protection systems. The experimental results obtained from photographs, pressure traces, and visual inspection were analyzed for each test series. The degree of theoretical analysis involved varied considerably from one series to another.

The effect of the impact expansion cloud on multifoil thin aluminum witness sheets was analyzed on a visual basis from experimental photographs, and inspection of the sheets after impact. Much information was obtained on the mode of failure for the individual sheets of the witness plate (Section 3.1). However, more specific experimental investigations and a more detailed theoretical analysis would be required before detailed conclusions of the precise failure modes could be made.

A series of impact pressure traces were obtained in order to determine the nature of the double pressure pulse observed experimentally. By varying the bumper thickness and the spacing of the probe behind the bumper, experimental verification that the second pulse was due to unvaporized pellet material was obtained (Section 3.2). This was further verified by considering the theoretical one-dimensional shock decay data obtained previously (Reference 2).

Two test series were carried out to determine experimentally the impulse loading on a secondary surface. A Lexan pellet and Lexan bumper were used for one series, and a Lexan pellet and lead bumper were used for the other. For each shot the loading history on the witness plate was obtained from four flush mounted piezo-bar probes, three of which were displaced radially from the center axis of the expansion cloud. By varying the spacing of the piezo-bar probes behind the bumper for each shot, an experimental pressure distribution within the expansion cloud was obtained (Section 3.3). The total momentum communicated to the secondary

surface was determined by a direct numerical integration of the pressure distribution and also by integration of an analytical representation of the distribution. The results for eight test shots, four from each series, are presented in Section 3.3.

In the absence of experimentally determined Hugoniot data for Lexan it is difficult to predict accurately the initial shock state properties. However, the pellet and bumper shock velocities, and escape velocities, can be obtained experimentally with a B & W 300 framing camera. From a theoretical analysis of these velocities some shock state properties can be obtained. In Section 3.4 photographic records of six impacts of pellets onto discs and bars are analysed. A good correlation was obtained between polytropic exponents determined from shock velocities and from material compressions, justifying the use of a one-dimensional analysis to establish Hugoniot data. However, little or no correlation was found for the observed escape velocities and shock properties in terms of an ideal gas relation.

Five different pellet shapes were impacted onto lead bumpers and measurements of the pressure in the expansion cloud were made. The shape of the pellet was observed to have a marked effect on the pressure in the expansion cloud downstream of the bumper. However, it was felt that at meteoroid velocities the energy generated on impact would be so great as to obliterate shape effects several meteoroid diameters downstream.

Some theoretical effort has been devoted to understanding the initial impact process during the time the pellet is being shocked (Section 4.1).

The net result of the study was the inclusion into the model of two polytropic exponents, one to describe the shocked states and one to describe the expansion process. By incorporating the two polytropic exponents into the strip model (Section 4.3), the experimental expansion front velocities are satisfied as well as experimental shock Hugoniot data. Some other modifications were made to the strip model, such as allowance for reflected shock waves from the probe tip and a variable shock $\gamma_s$ to allow for the shock decay process. The inability of the strip model to predict the large upstream expansion flow experimentally observed was recognized. The results of a calculation at a typical meteoroid impact velocity are presented in Section 4.3. However, the accuracy of the calculation is questionable to the extent that no allowance is made for ionization effects.

The one-dimensional finite difference model was reported in Reference 8. The model is summarized in Section 4.2. The mathematical difficulties encountered in the long term stability associated with Von Neuman's artificial viscosity were surmounted by incorporating a smoothing routine. Results show that the pellet shock pressure decay is not as rapid as the decay obtained neglecting entropy changes at the shock front (Reference 2). Results obtained for the pressure on a secondary surface allowing for a secondary reflected shock are also presented.

Near the end of the contract period a few experimental impacts on a grid bumper were carried out. Piezo-bar pressure traces showed that for the same mass of bumper in grid form rather than in solid form the axial pressure would be reduced in amplitude and spread out in time. In Section 5 the possibilities of the grid bumper used as a meteoroid protection system are outlined, along with preliminary results and analyses.

## 2.0 RANGE AND INSTRUMENTATION DEVELOPMENT

The impact range and instrumentation have remained essentially unchanged from that described in Reference 1. Modifications to the tankage system have been confined to an increase in the length of the muzzle x-ray port and the addition of a swing door at the aft end of the main horizontal section of the impact tank. The piezo-bar pressure gauge developed during the last contract period (NAS3-4190) has been improved considerably by the addition of a by-pass filter to eliminate electronic interference caused by ionization effects of the gas cloud.

### 2.1 TEST RANGE SYSTEM

The swing door which has been added to the rear end of the test tank is shown in Figure 2.1a. This modification was made so that the piezo-bar pressure gauges and the thin bumper could be completely assembled in the new mount system outside the impact tank. Because of this, the entire instrument system can be tested and checked during the pre-firing check test of the range and then inserted intact and unchanged into the impact tank. This procedure prevents inadvertent alteration to the spacings during installation of the equipment into the test chamber, thereby improving experimental accuracy (Figure 2.1b).

The enlarged muzzle x-ray port is shown in Figure 2.2. This modification was made to improve the accuracy and reliability of the muzzle trigger and x-ray photographic system, and to provide an additional mechanism for projectile velocity determination. Figure 2.3a shows a schematic diagram

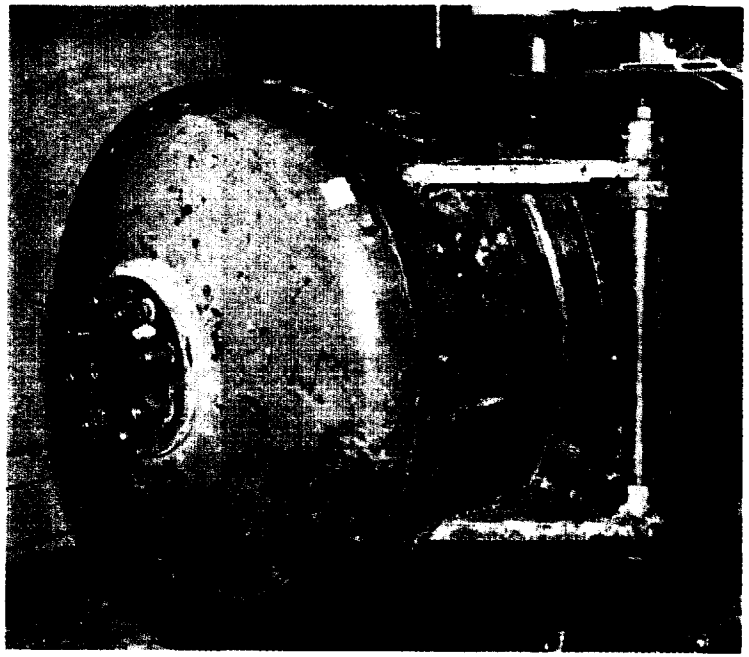

Fig. 2.1a SWING DOOR ON MODIFIED IMPACT TANK

Fig. 2.1b GAUGE MOUNT WITH PROBES PLACED IN IMPACT TANK THROUGH SWING DOOR

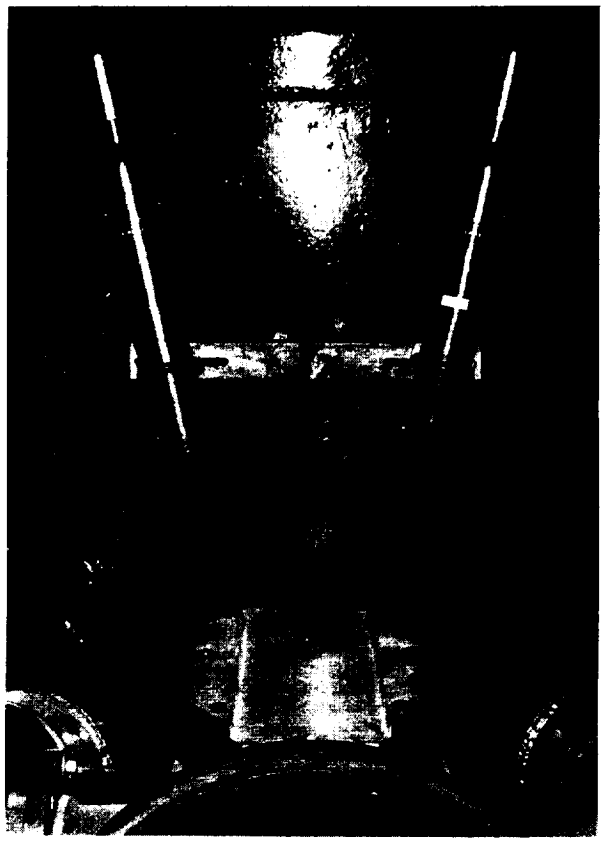

Fig. 2.2 MODIFIED X-RAY PORT ON IMPACT TANK

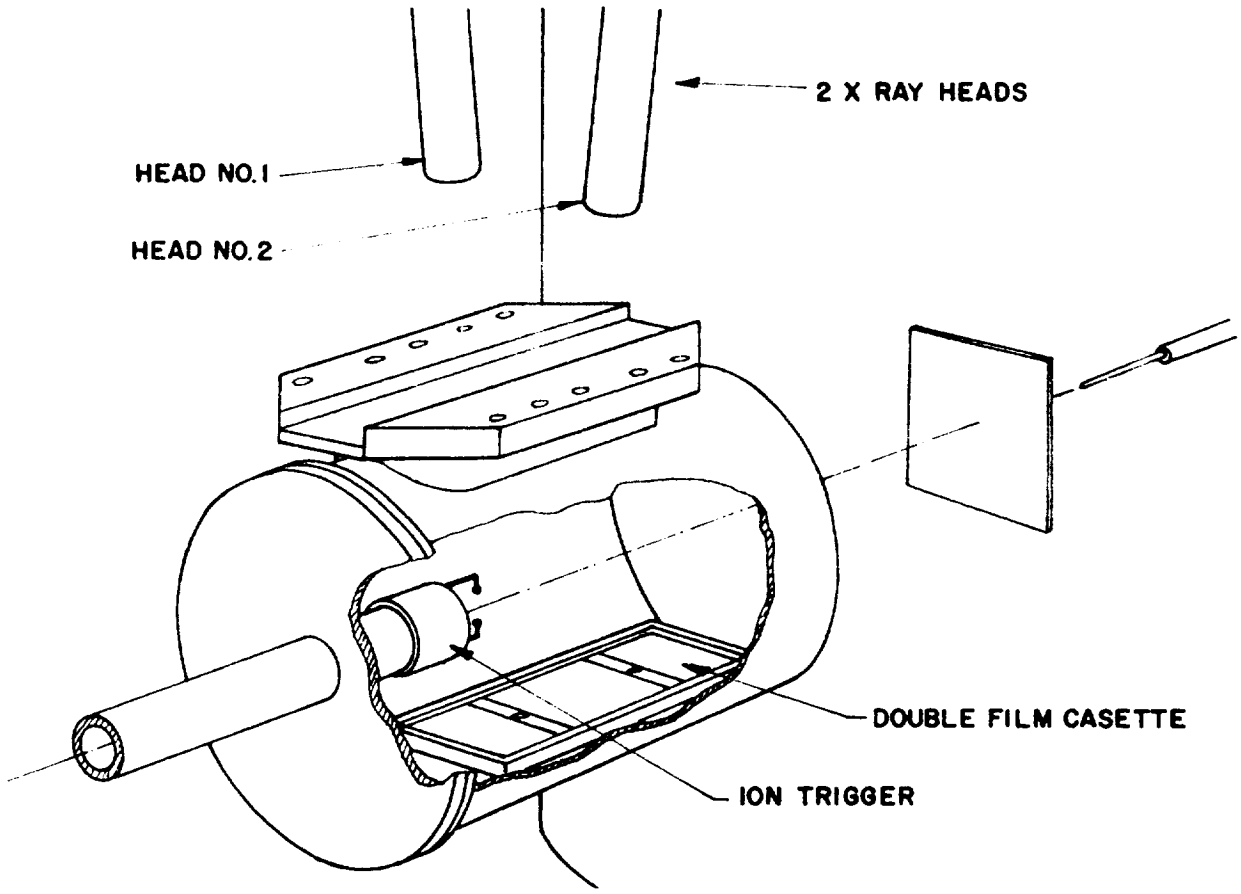


Fig. 2.3a DRAWING OF EXPERIMENTAL ARRANGEMENT USED TO OBTAIN X-RAY CONFIRMATION OF PELLET VELOCITY

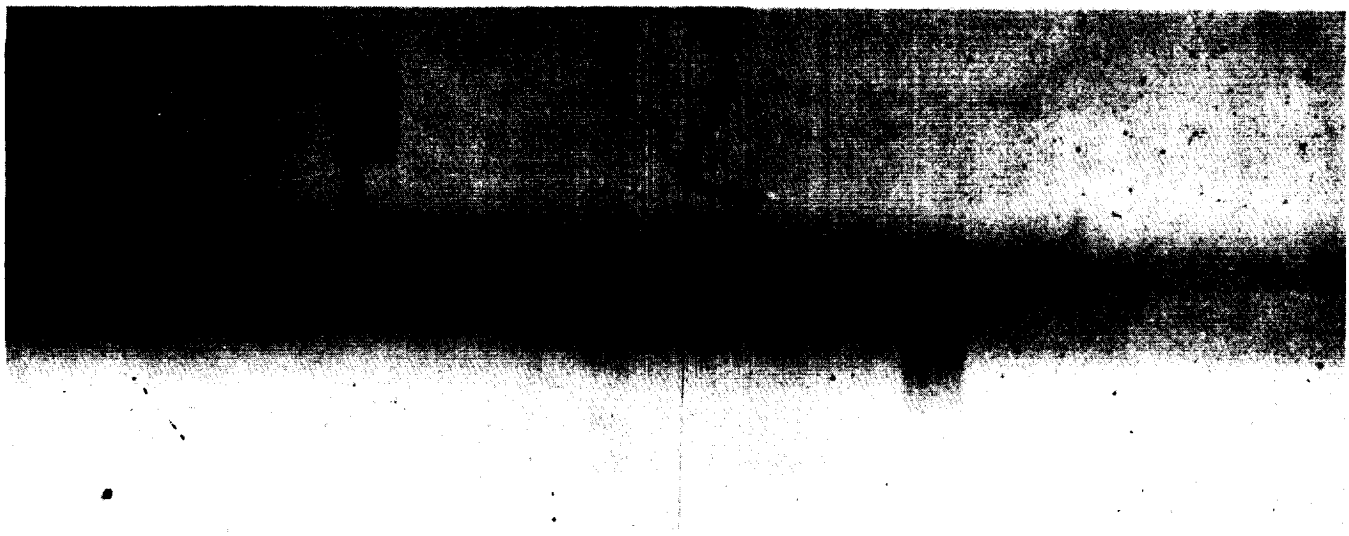

Fig. 2.3b X-RAY PHOTOGRAPH OBTAINED USING THE EXPERIMENTAL ARRANGEMENT OF Fig. 2.3a

of the muzzle x-ray arrangement and in Figure 2.3b, the muzzle x-ray record of laboratory shot No. 283 is presented.

The photograph shows the projectile in two positions on the plate, one approximately four inches from the gun muzzle, and the other approximately sixteen inches. The double exposure was obtained by pulsing one x-ray head (in this case No. 2) some 10 μsec after the muzzle ion trigger pulse, and in other (No. 1) some 45 μsec after the ion trigger pulse. The projectile velocity may be computed directly from this record since the distance travelled by the projectile between the two x-ray pulses may be obtained from the film record and the predetermined relation between the real projectile position and its shadow cast on the film plate by the x-ray beam.

## 2.2 PIEZO-BAR GAUGE DEVELOPMENT

The piezo-bar pressure gauge system developed during the contract period NAS3-4190, has proven a reliable instrument for the measurement of pressure in a plasma. An important feature of the gauge which has made reliable pressure measurements possible in the highly ionized impact gas clouds has been the separation of the pressure signal from an electrical input from the cloud (Langmuir effect) by the inherent acoustic delay in the pressure bar. The Langmuir signal is produced by a transfer of electrons from the gas cloud to the metallic portions of the gauge, wetted by the cloud, due to the relatively greater mobility of electrons in the metal. If the Langmuir effect persists for a period of time greater than the acoustic delay time of the front bar of the probe, it will combine with the

signal resulting from the compression of the piezo-electric element of the gauge since the recording and amplifying instruments cannot differentiate between the charge output from the crystal and an electron transfer from the cloud.

Careful grounding and insulation of the metallic parts of the gauge from direct contact with the gas cloud eliminates much of the Langmuir effect signal. However, the erosive nature of the cloud produced by hypervelocity thin sheet impact precludes absolute elimination of this effect by insulation alone. The high input impedance of the charge amplifiers used in conjunction with the bar gauge aids in the reduction of the effect, but in practice, complete elimination of the Langmuir effect is not achieved by either method.

The effect of the electron transfer from the gas cloud to the gauge is shown on the oscilloscope trace of Figure 2.4a. For this record, the probe was placed on the flight axis, 6 ins (15.2 cms) downstream of the bumper, and the impact velocity was 26,100 ft/sec (7.95 km/sec). The trace was initiated by the bumper impact trigger (confirmed by the STL image converter record of Figure 2.4b) and the impact cloud made initial contact with the probe tip at 14 μsec after impact (determined from the B & W 192 high speed framing camera records). Inspection of the pressure record trace shows that the first output signal from the gauge system coincides with the first contact between the cloud leading edge and the probe tip (i.e. at I+14 μsec) and is the result of the Langmuir effect. (The spike pulses observed immediately after the start of the sweep are the five STL image converter frame trigger pulses which are recorded on this trace by "pick-up" in the control signal cables.)

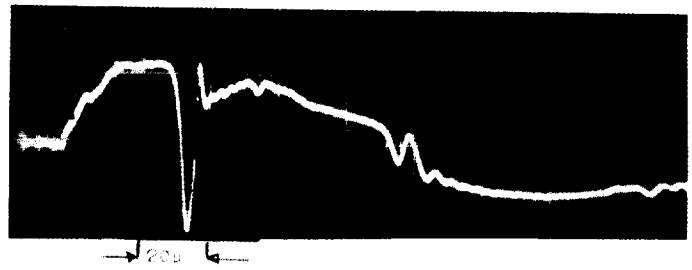

Fig. 2.4a Piezo-Bar Output Trace for Shot Number 279. The Impact is that of a 0.5 in.-Dia. by 0.285 in.-Long Lexan Pellet on a 0.010 in. - Thick Bumper at a Velocity of 26,100 ft/sec(7.95 km/sec). The Probe was Located a Distance of 6 ins.(15.2 cm) Behind the Bumper. The Horizontal Scale is 20 μsecs/cm

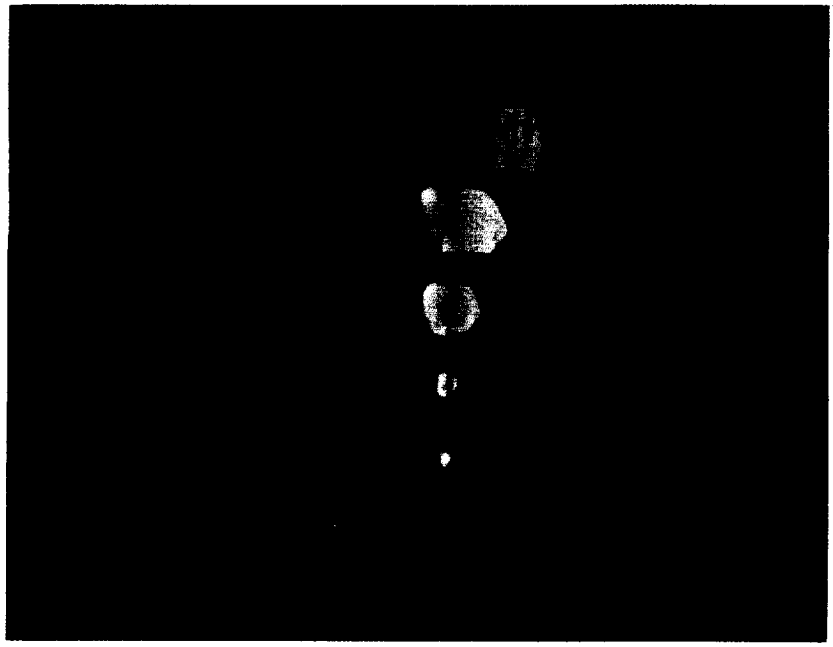

Fig. 2.4b Five-Frame STL Camera Sequence of Shot Number 279 (Same as in Fig. 2.10a). The Frames, From Bottom to Top, are Taken at 0, 2, 7, 12 and 32 μsecs After Impact.

The pressure pulse record measured by the piezo-bar gauge is delayed approximately 31 μsec by the acoustic delay in the pressure bar, and appears on this trace as the negative pulse commencing some 45 μsec after impact. The interference from the Langmuir effect, which produced the marked deflection of the oscilloscope beam prior to the arrival of the pressure signal from the gauge, makes accurate interpretation of the pressure record difficult. The characteristic pressure signal is clearly visible (as is an indication of the reflected signal pulse 62 μsec after the commencement of the primary signal.) However, without a constant "zero pressure" reference, accurate measurement of the magnitude of the pressure signal is clearly impossible.

At the lower impact velocities, insulation and grounding appeared to confine the Langmuir effect signal to an acceptably low level on many firings. However, as pressure measurements were attempted at higher and higher impact velocities, it became apparent that the Langmuir effect was increasing in magnitude to the extent that the pressure measurements obtained on many shots were meaningless. This phenomenon is undoubtedly due to the fact that the impact-generated cloud is more highly ionized at the higher impact velocities. In many cases the effect was so large that the oscilloscope trace was deflected completely off scale.

To overcome this problem, the piezo-bar gauge was modified to provide an independent but identical electrical path (filter probe) for the recording of the Langmuir effect signal without interfering with the system as an instrument for recording pressure. The modified gauge system, shown in Figure 2.5, has

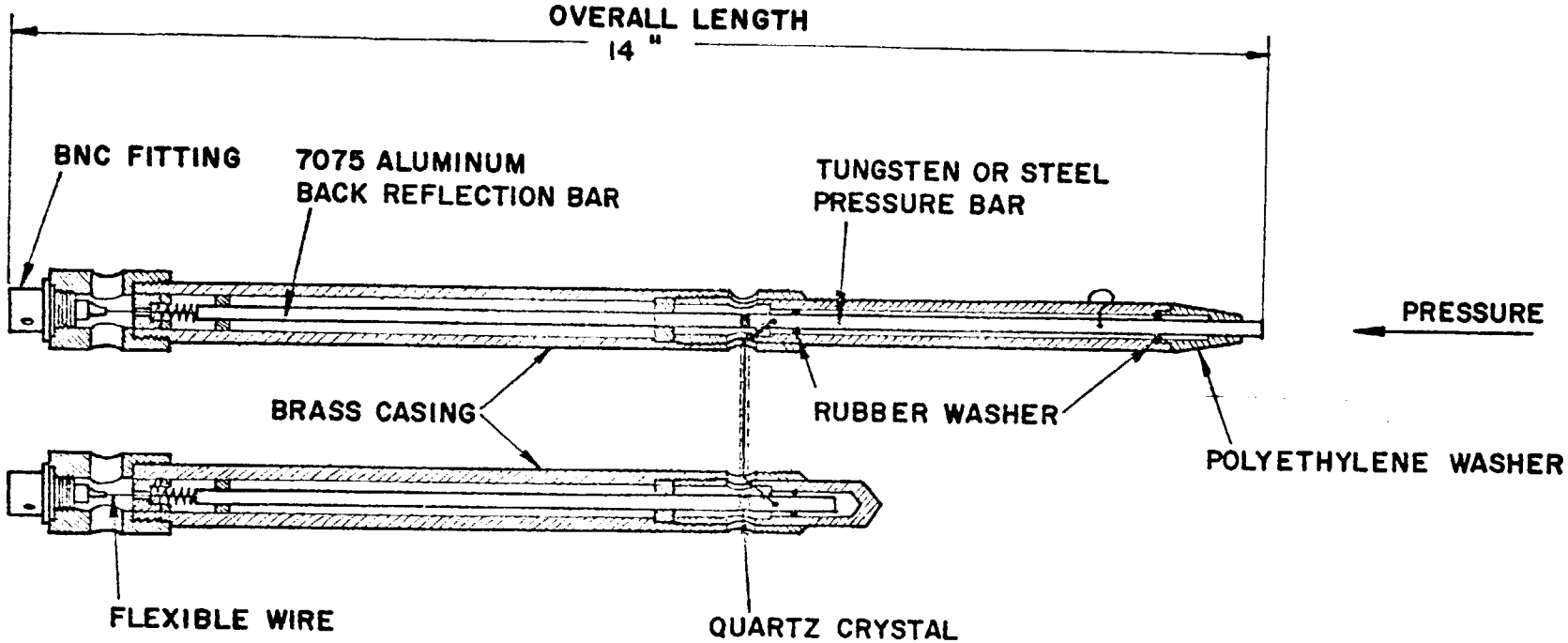


Fig. 2.5 PIEZO-BAR PRESSURE GAUGE AND FILTER PROBE

two output terminals, one for monitoring the total output of the gauge system (i.e. charge output from the piezo-electric crystal and electron transfer from the impact cloud) and the other for monitoring electron transfer only. As may be seen from the figure, the front bar of the filter probe is connected electrically to the pressure bar of the main probe (through a low impedance flexible wire). The potential of both front bars is thereby maintained at essentially the same level, neglecting losses in the wire.

The result of this modification to the gauge system is demonstrated in Figure 2.6. The shot conditions which produced the records shown in this figure are identical to those of Figure 2.4, with the exception of a slightly lower impact velocity (25,500 ft/sec (7.77 km/sec)). On the oscilloscope record of this figure, the upper trace is the output of the main pressure probe and the lower trace that of the filter probe. Using the filter probe output as a guide, the Langmuir effect signal and the piezo-electric pressure signal which combine to form the upper trace may now be separated.

The filter gauge output is seen to be approximately 20% lower than the corresponding signal for the main gauge. In a "static" test of the modified gauge system prior to range testing, a 100 kc square wave test signal was found to suffer the same reduction through the filter probe.

The charge amplifiers used in conjunction with the piezo-bar gauge system have continuously variable gain, so that in future tests the "total gain" of the filter probe plus charge amplifier may be made equal to the total gain of the main gauge system. Once the Langmuir effect response of the two sections of

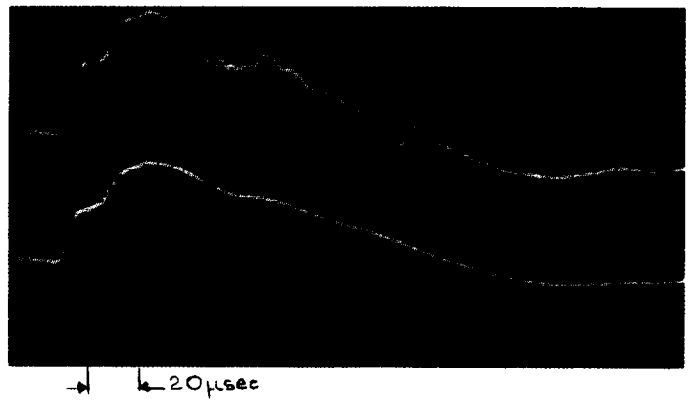


FIG. 2.6a PIEZO-BAR OUTPUT TRACE (UPPER BEAM) AND FILTER PROBE OUTPUT TRACE (LOWER BEAM) FOR SHOT NUMBER 280.

The impact is that of a 0.5-in.(1.27 cm) dia. by 0.285-in.(0.725 cm) long Lexan pellet on a 0.010-in.(0.025 cm) thick lead bumper at a velocity of 25,500 ft/sec (7.77 km/sec). The probe was located a distance of 6-in.(15.2 cm) behind the bumper. The horizontal scale is 20 μsec/cm.

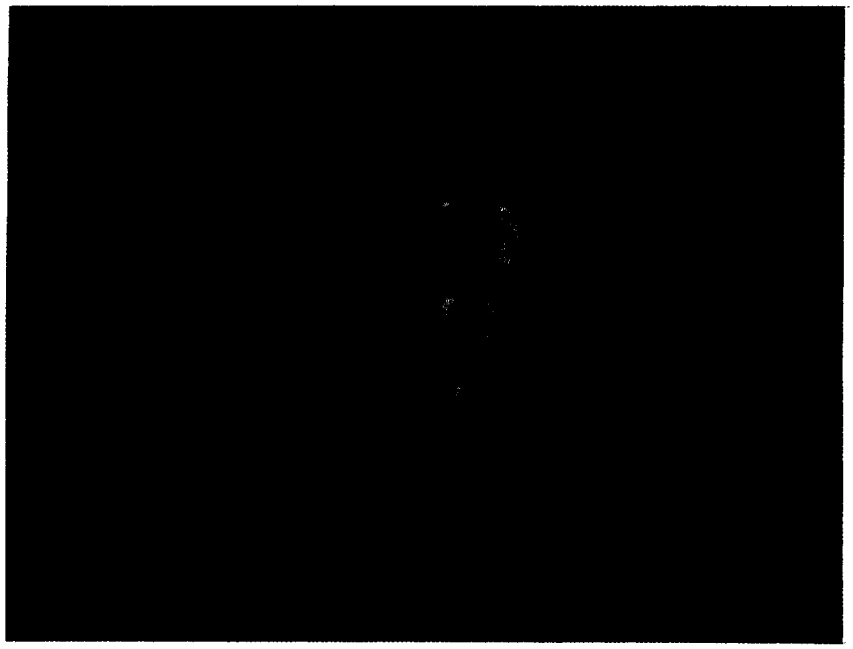

FIG. 2.6b FIVE-FRAME STL CAMERA SEQUENCE OF SHOT NUMBER 280

The frames, from bottom to top, are taken at 0, 2, 7, 12 and 32 μsec after impact.

the gauge system have been equalized, the two output signals from the gauge system may be passed through a differential amplifier and subtracted electronically. The resulting signal displayed on an oscilloscope beam will then be the output of the piezo-electric crystal element alone, with all external electrical signals eliminated.

## 3.0 EXPERIMENTAL TESTS AND ANALYSIS

### 3.1 MULTIFOIL WITNESS SHEETS

In compliance with a specific request from the LeRC Project Monitor, a series of firings was conducted in which an 0.01 ins (0.025 cms) lead bumper sheet and six 0.050 ins (0.127 cms) 2024 aluminum witness sheets were arranged as shown in the sketch of Figure 3.1. The projectile in each case was a Lexan cylinder 0.50 ins (1.27 cms) in diameter and 0.285 ins (0.725 cms) long, impacting against the lead bumper at velocities between 20,000 and 30,000 ft/sec (6.1 and 9.15 km/sec). The specific configuration selected, viz 3 ins (7.61 cms) spacing between the bumper and first witness sheet and 2 ins (5.08 cms) between witness sheets, was specified by the LeRC Project Monitor.

A number of photographic records are presented in Figures 3.2 through 3.5 and the data from the test series are recorded in Table 3.1. Beckman and Whitley Model 192 framing camera and STL Model ID image converter camera records were obtained for the majority of the tests conducted in this series.

In Table 3.1, the witness sheet damage is tabulated; the numbers in the table ascribed to each witness sheet refer to the mean diameter of the perforation produced in each plate. In general, the damage to the witness sheets was not in the form of a circular hole punched in the sheet. The characteristic damage pattern consisted of a small amount of actual material loss from the witness sheets due to punch-out, spallation or erosion. The large hole was produced by the petalling of the plate along radial tears originating from the center of the damaged zone. The photograph of Figure 3.2b shows the characteristic

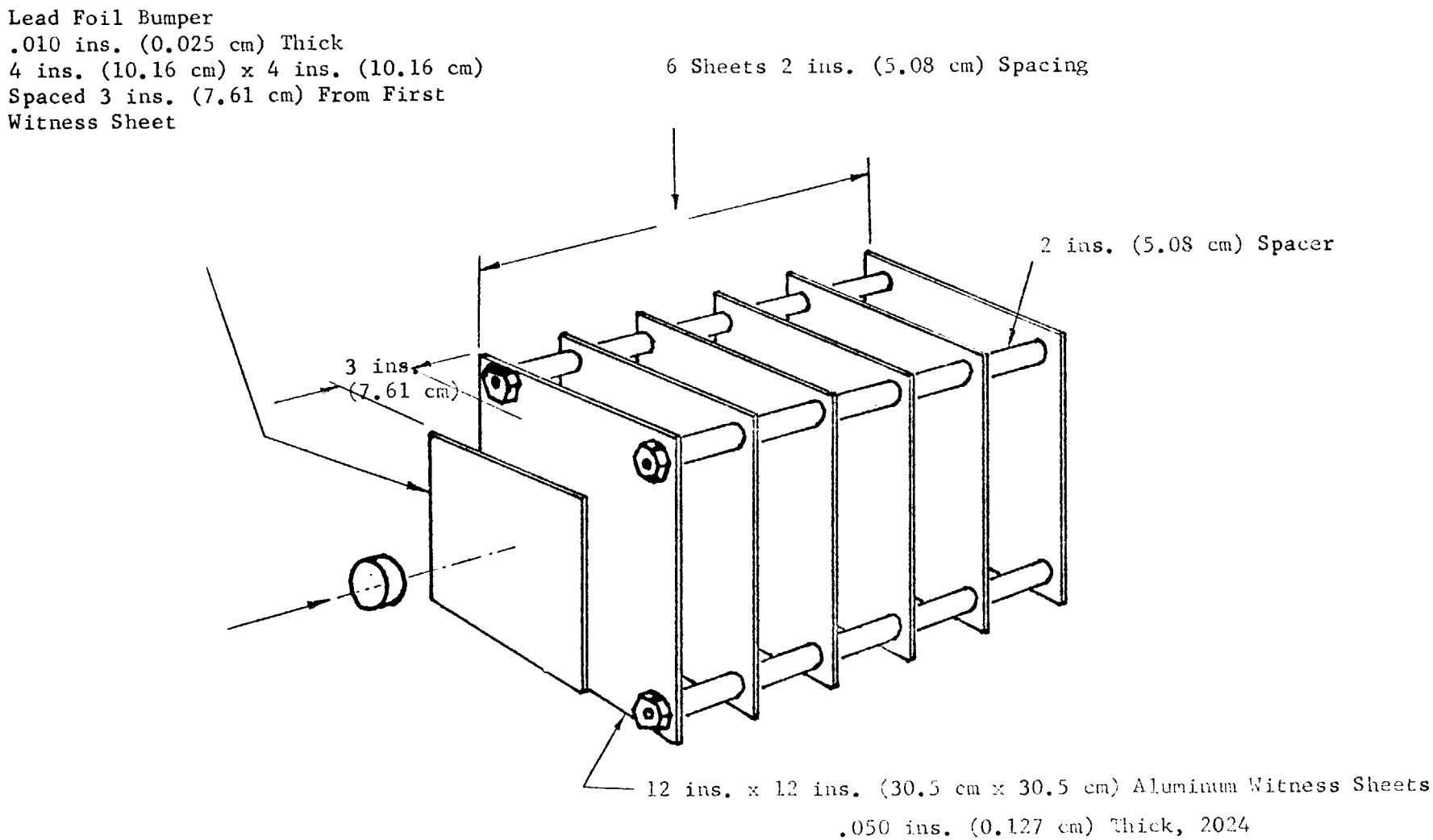


FIG. 3.1a Schematic Drawing of the Experimental Arrangement for the Multi-foil Experiments

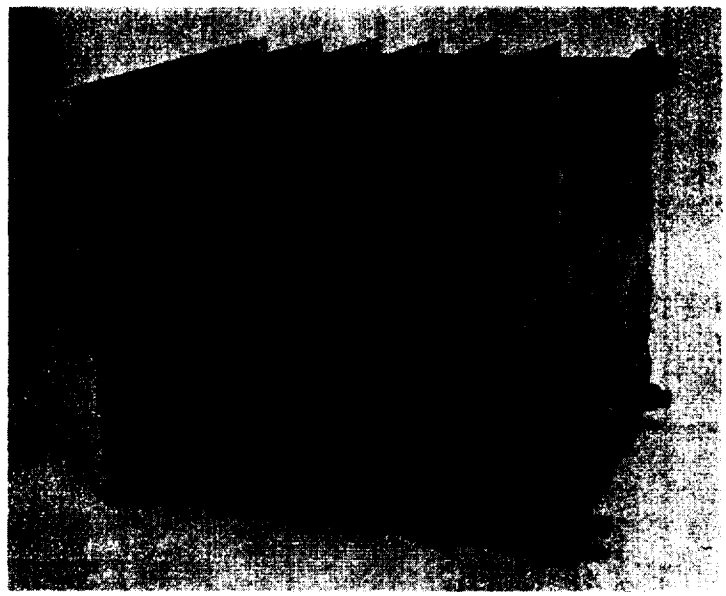

FIG. 3.1b Photograph of the Experimental Arrangement for the Multi-foil Experiments

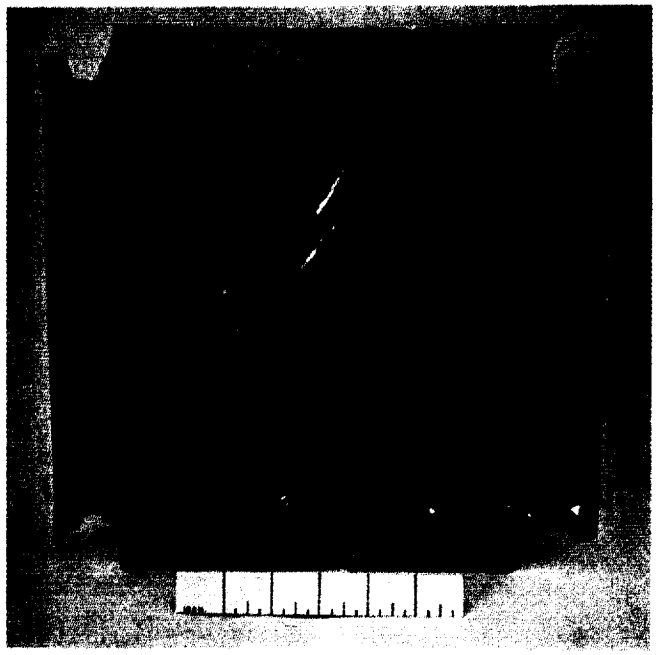

(a)

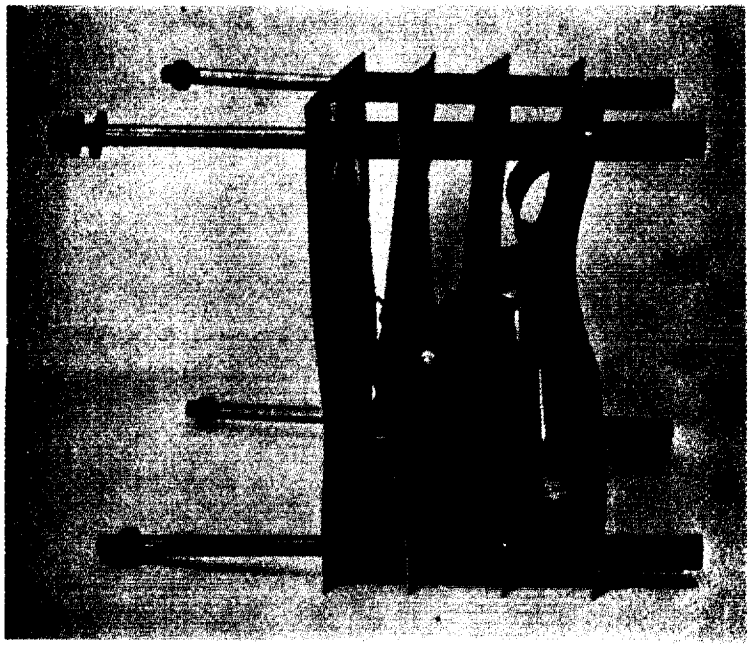

(b)

FIG. 3.2a and b PHOTOGRAPHS OF THE LEAD BUMPER AND THE FIRST FOUR ALUMINUM PLATES OF THE MULTI-FOIL ARRANGEMENT AFTER SHOT NUMBER 260.

The impact is that of a 0.50-in. (1.27 cm) dia. by 0.285-in. (0.725 cm) long Lexan pellet on a 0.010-in. (0.025 cm) thick lead bumper at a velocity of 25,050 ft/sec (7.77 km/sec).

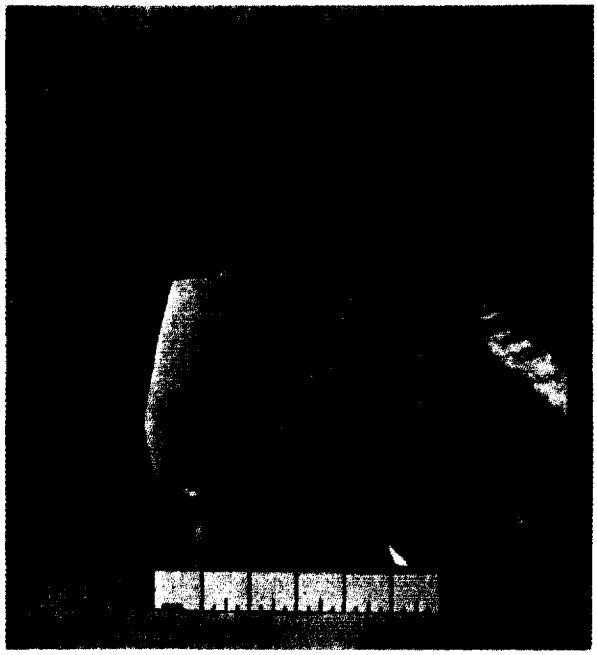

(c)

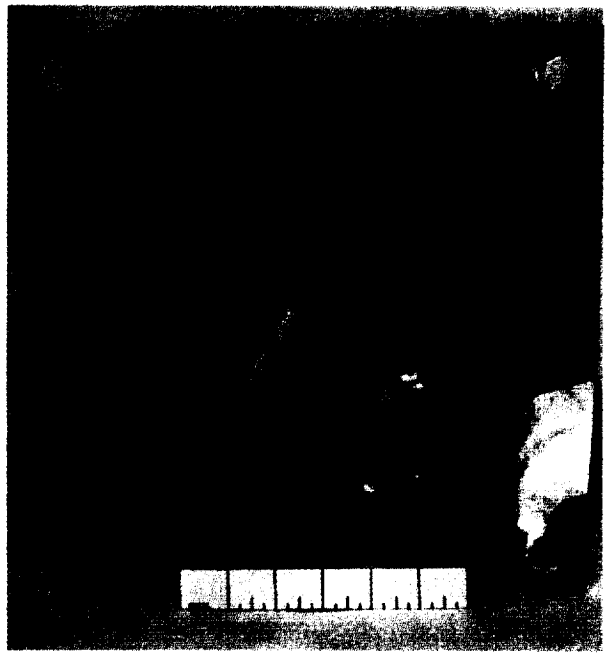

(d)

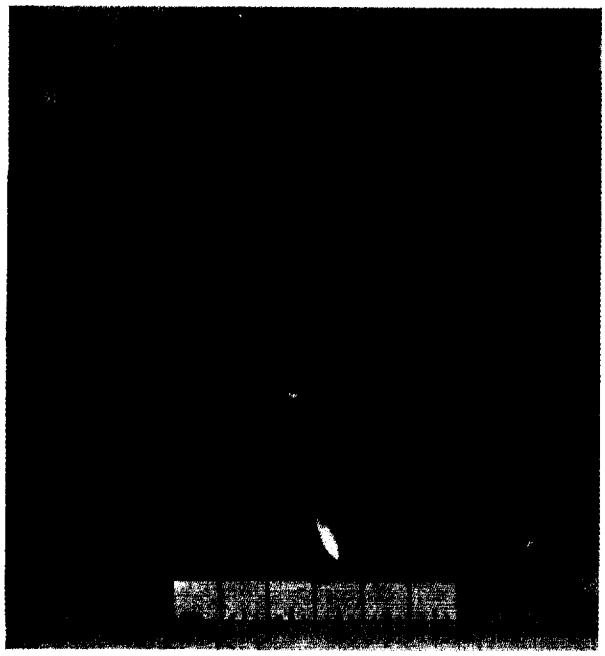

(e)

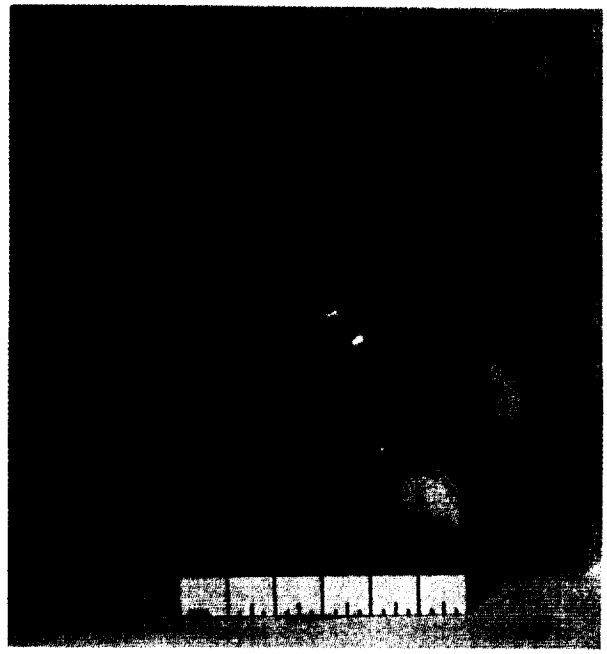

(f)

Fig. 3.2 c to f INDIVIDUAL PHOTOGRAPHS OF THE FIRST FOUR ALUMINUM PLATES OF SHOT NUMBER 260

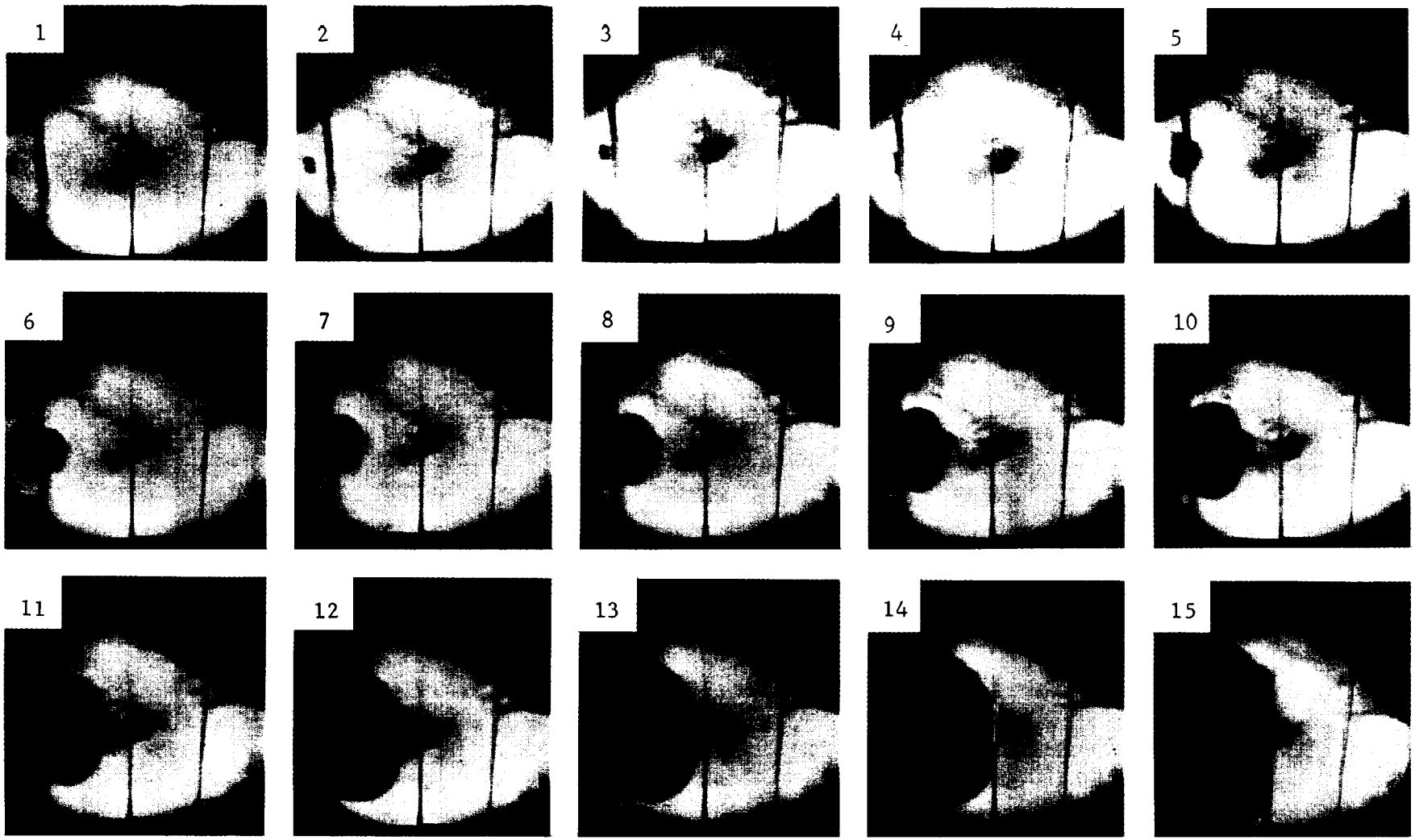


FIG. 3.3 Complete Beckman and Whitley Model 192 Framing Camera Sequence of Shot Number 260.

The impact is that of a 0.50-in. (1.27 cm) dia. by 0.285-in. (0.725 cm) long Lexan pellet on a 0.010-in. (0.025 cm) thick lead bumper at a velocity of 25,050 ft/sec (7.7 km/sec). The first two aluminum plates of the multi-foil arrangement are visible. The time between successive frames is 0.822 $\mu$sec.

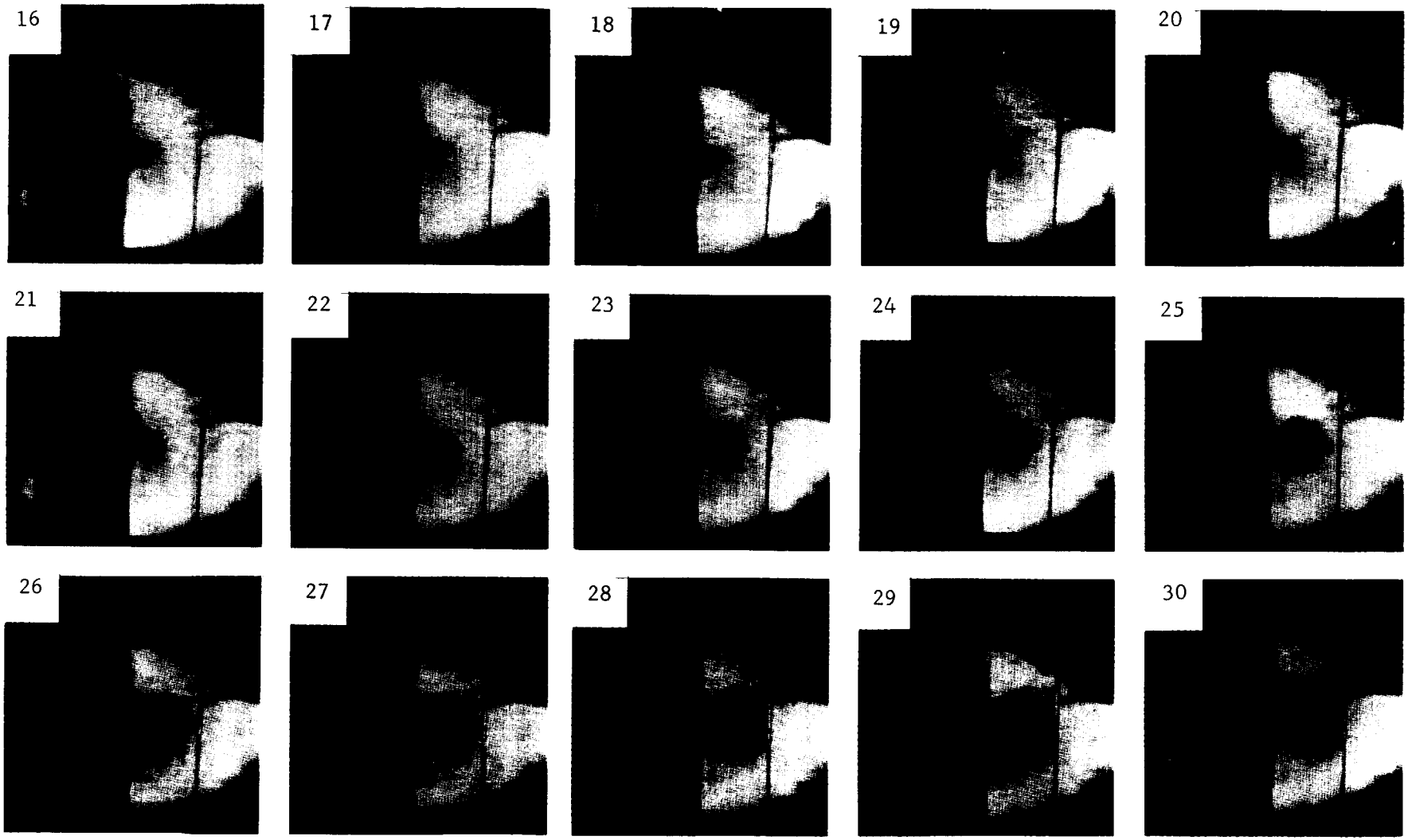


Fig. 3.3 continued

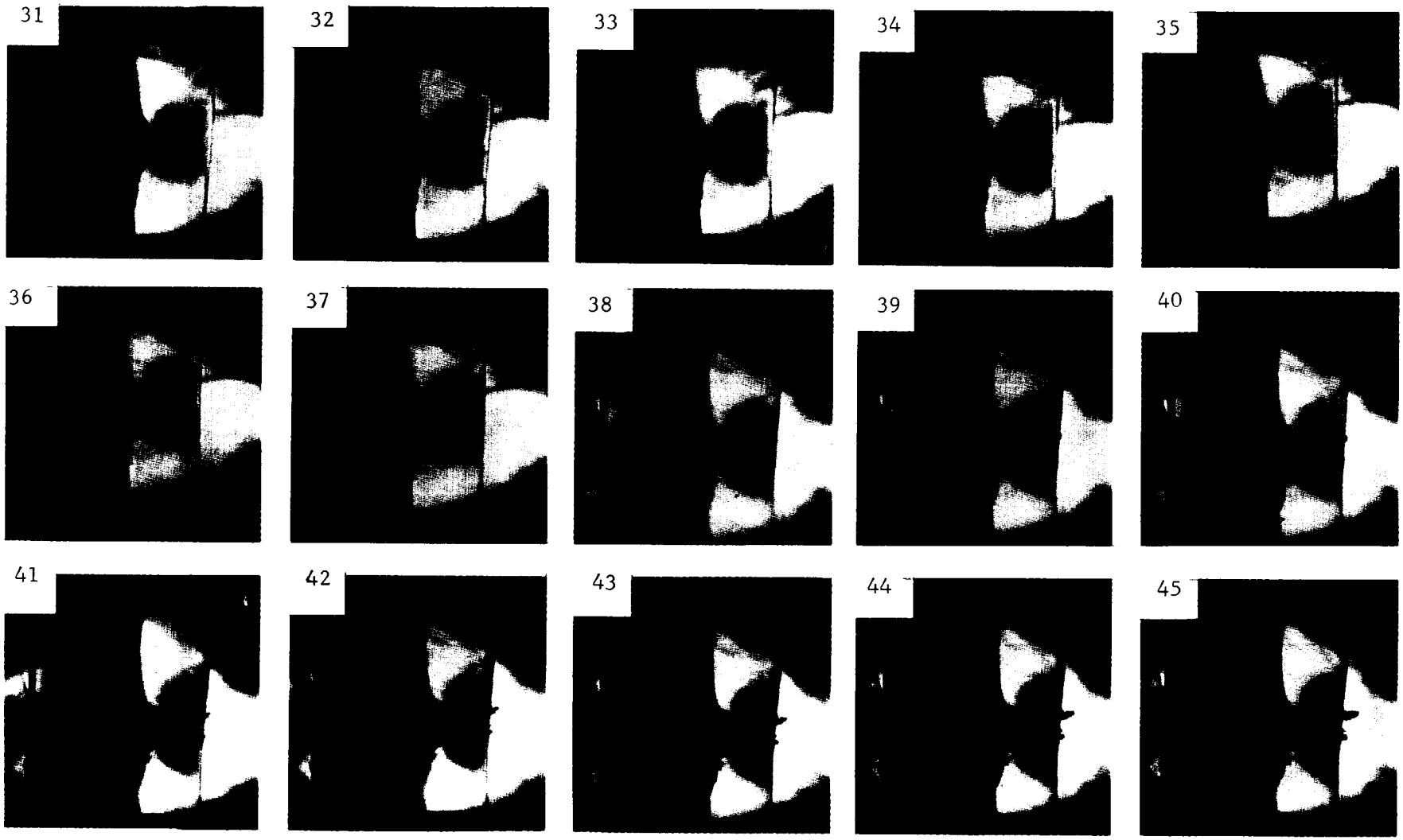


Fig. 3.3 continued

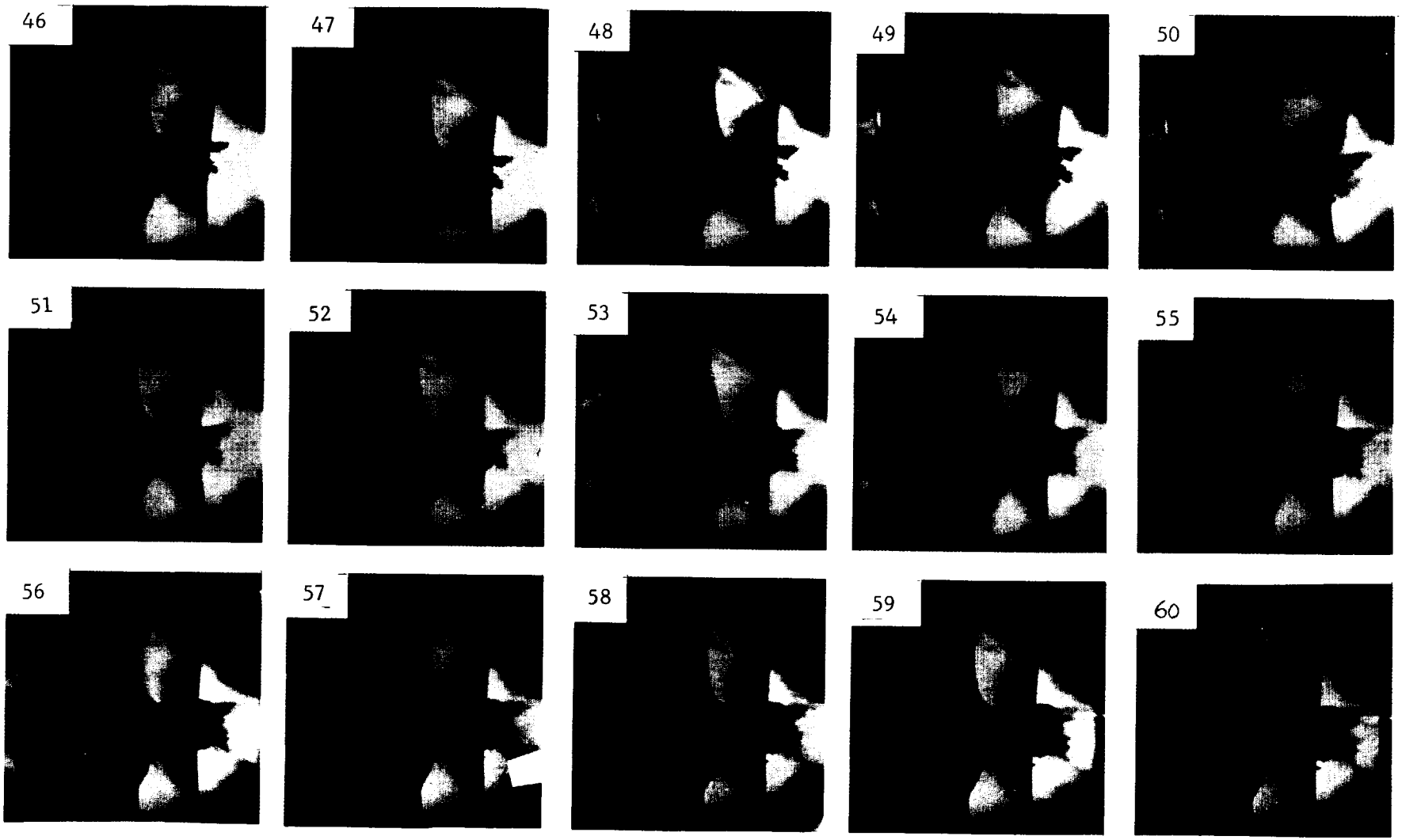


Fig. 3.3 continued

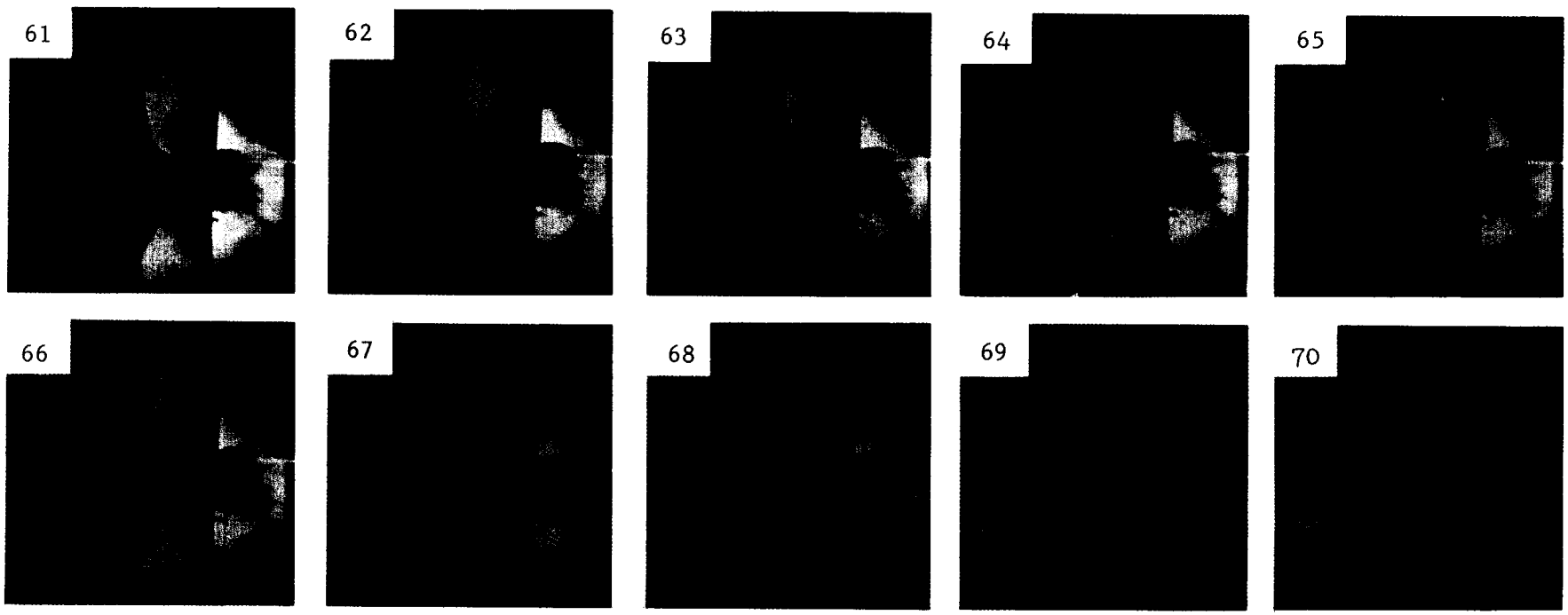


Fig. 3.3 continued

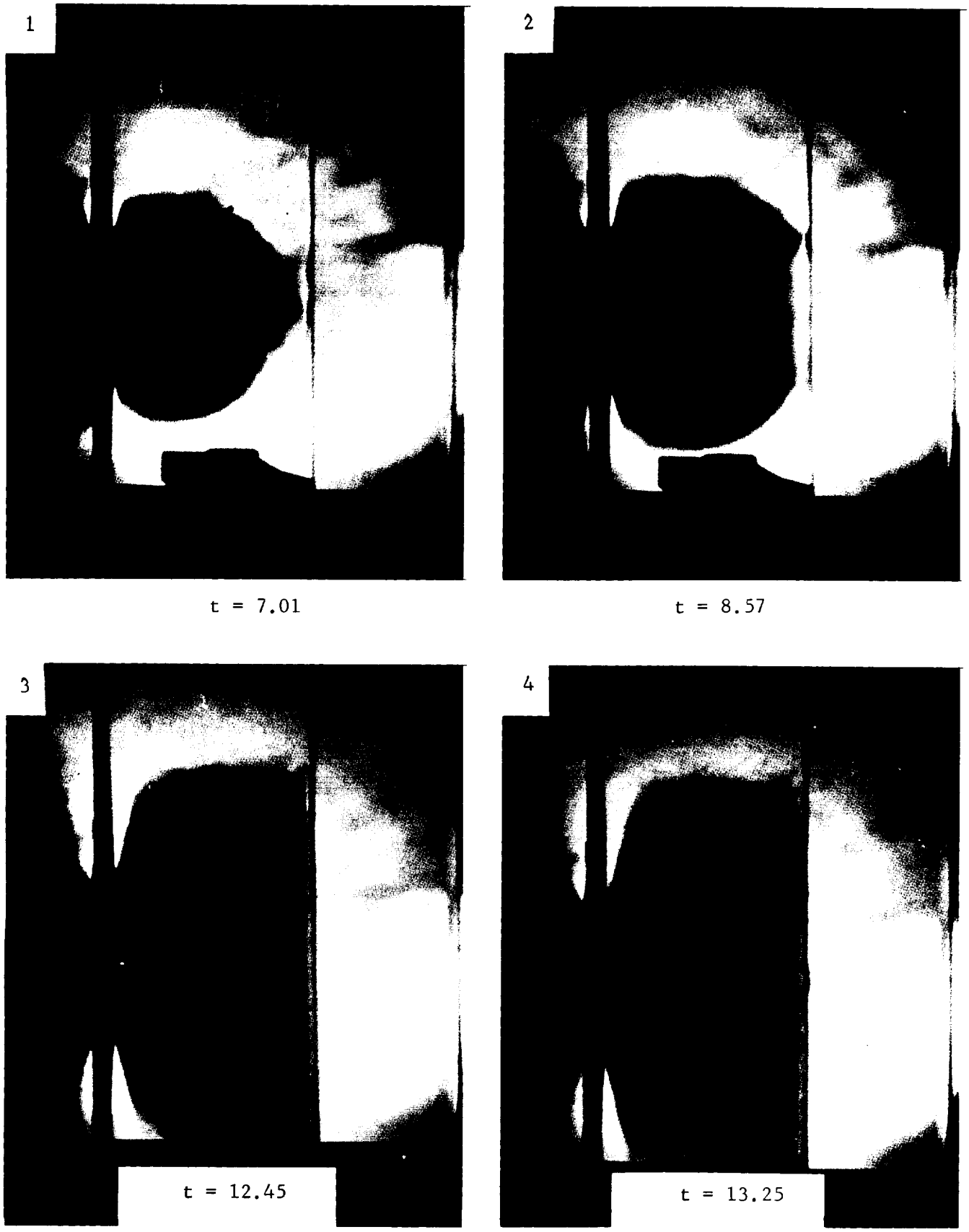


Fig. 3.4 Beckman and Whitley Model 192 Framing Camera Sequence of Shot Number 269

The impact is that of a 0.50-in.(1.27 cm) dia. by 0.285-in.(0.725 cm) long Lexan pellet on a 0.010-in.(0.025 cm) thick lead bumper at a velocity of 30,250 ft/sec (9.22 km/sec). The first two aluminum plates of the multi-foil arrangement are visible. The indicated times are in μsec after impact.

t = 14.8

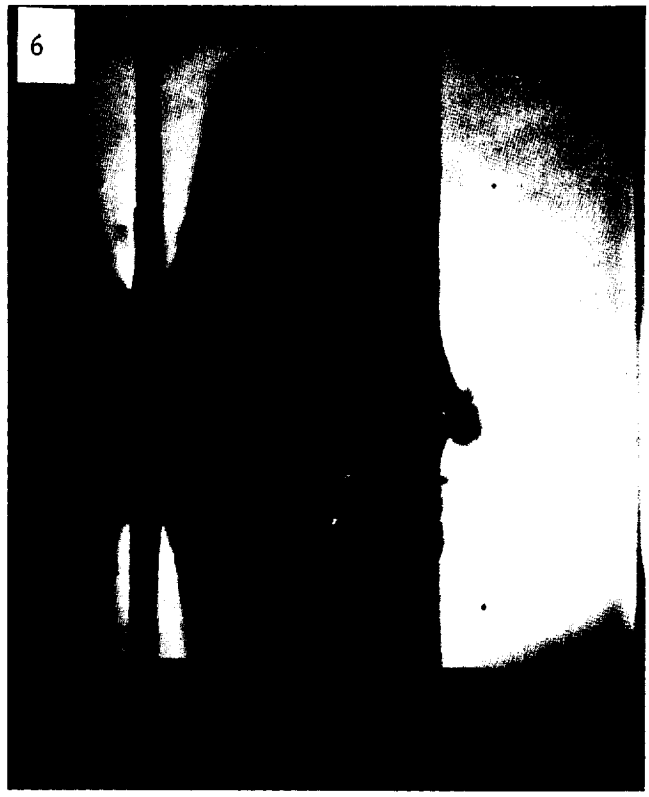


t = 17.1

t = 21.8

t = 24.2

Fig. 3.4 continued

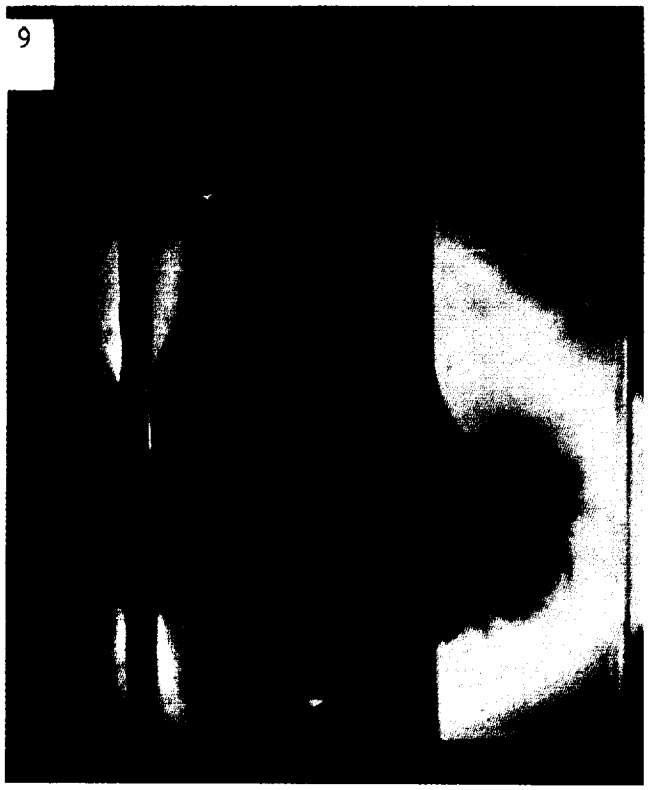


t = 25.7

t = 28.0

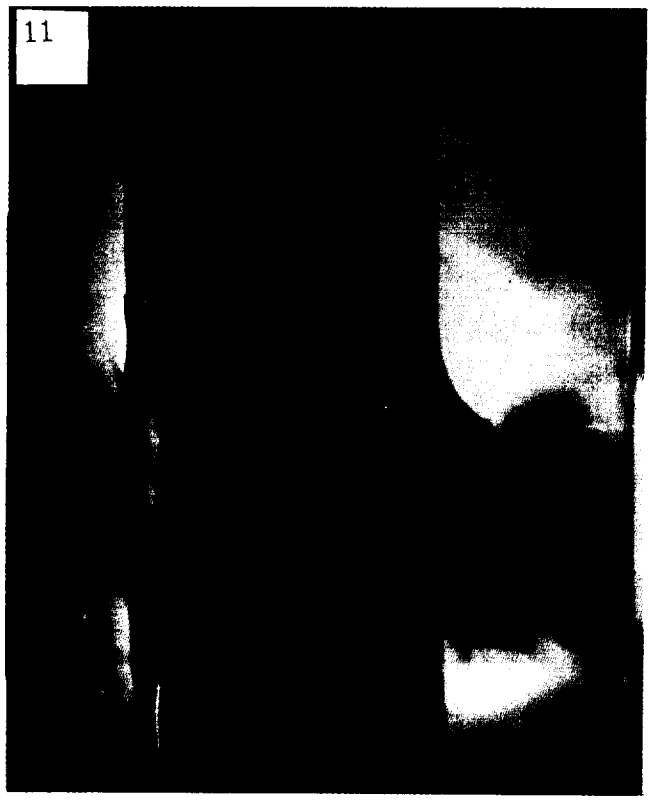


t = 31.9

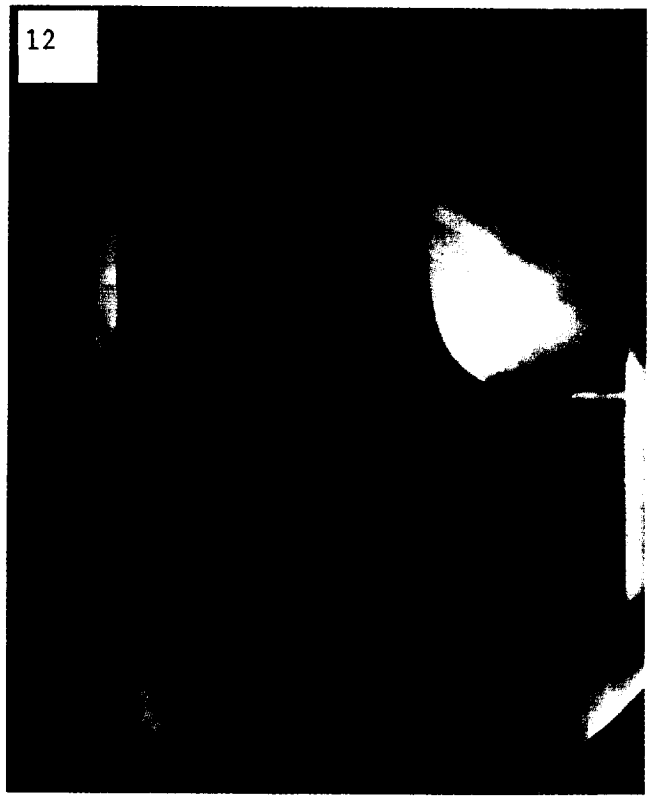


t = 38.9

Fig. 3.4 continued

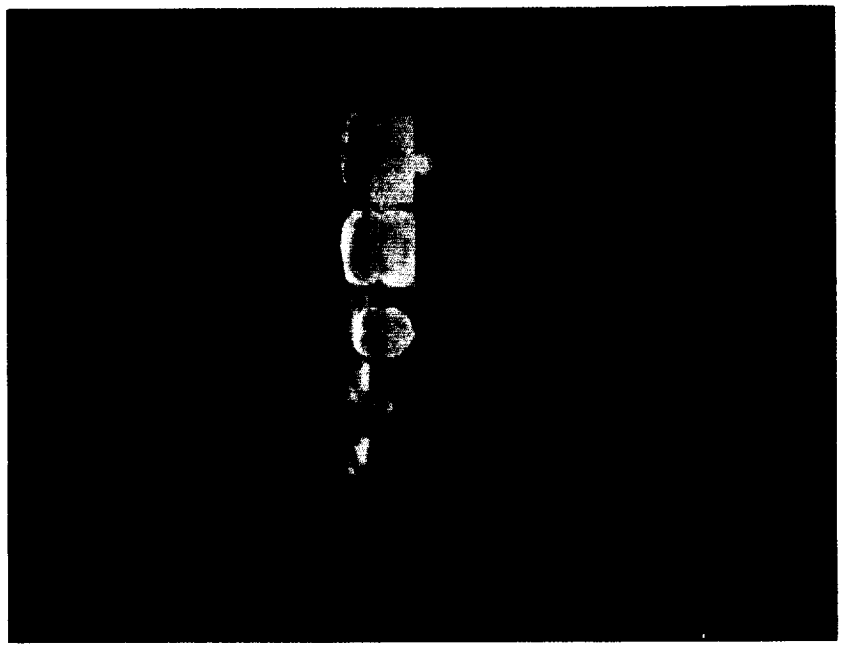

Fig. 3.5a Five-Frame STL Camera Sequence of Shot Number 253

The impact is that of a 0.50-in.(1.27 cm) dia. by 0.285-in.(0.725 cm) long Lexan pellet on a 0.010-in. (0.025 cm) thick lead bumper at a velocity of 23,750 ft/sec (7.24 km/sec). The first four aluminum plates of the multi-foil arrangement are visible. The frames, from bottom to top, are taken at 0, 1, 3, 8 and 13 sec after impact.

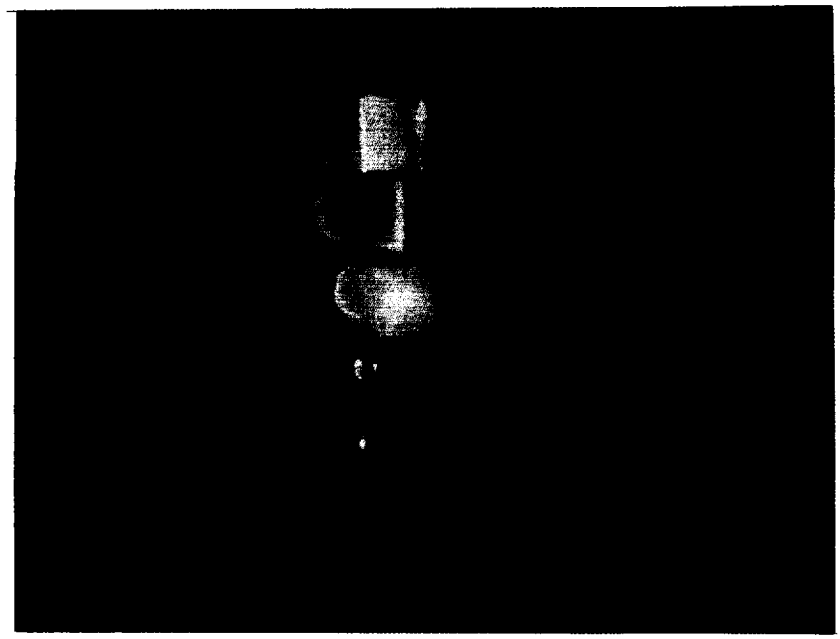

Fig. 3.5b Five-Frame STL Camera Sequence of Shot Number 269

The impact is that of a 0.50-in.(1.27 cm) dia. by 0.285-in.(0.725 cm) long Lexan pellet on a 0.010-in.(0.025 cm) thick lead bumper at a velocity of 30,250 ft/sec (9.22 km/sec). The first two aluminum plates of the multi-foil arrangement are visible. The frames, from bottom to top, are taken at 0, 2, 7, 12 and 32 sec after impact.

TABLE 3.1 Description Of Damage To Each Of The Six Aluminum Witness Sheets For Each Firing Against A Multiwall System

| SHOT NO. | VELOCITY ft/sec | VELOCITY km/sec | MEAN DIAMETER OF HOLE PLATE NO.1 in. | PLATE NO.1 cm | PLATE NO. 2 in | PLATE NO. 2 cm | PLATE NO. 3 in | PLATE NO. 3 cm | PLATE NO. 4 in | PLATE NO. 4 cm | PLATE NO. 5 in | PLATE NO. 5 cm | PLATE NO. 6 in | PLATE NO. 6 cm |
|---|---|---|---|---|---|---|---|---|---|---|---|---|---|---|
| 242 | not recorded | | $6\frac{1}{2}$ | $16\frac{1}{2}$ | $3\frac{1}{2}$ | 9 | 3 | $7\frac{1}{2}$ | 3 Bulge - molten Al. | $7\frac{1}{2}$ | no damage | | no damage | |
| 243 | not recorded | | 7 | $17\frac{3}{4}$ | $4\frac{1}{2}$ | $11\frac{1}{2}$ | $2\frac{1}{2}$ | $6\frac{1}{4}$ | 3 $\frac{1}{4}$-in. & bulge | $7\frac{1}{2}$ | indentation Molten Al. | | no damage | |
| 244 | not recorded | | 6 | $15\frac{1}{4}$ | $2\frac{1}{2}$ | $6\frac{1}{4}$ | $\frac{1}{2}$ & 1/8 | $1\frac{1}{4}$ 3/8 | indentation Molten Al. | | no damage | | no damage | |
| 254 | 19,640 | 5.99 | $4\frac{1}{2}$ | $11\frac{1}{2}$ | 4 | $10\frac{1}{4}$ | $2\frac{1}{2}$ | $6\frac{1}{4}$ | Bulge - Molten Al. | | no damage | | no damage | |
| 255 | | | 5 | $12\frac{3}{4}$ | $2\frac{3}{4}$ | 7 | 2 & $\frac{1}{2}$ | 5 $1\frac{1}{4}$ | indentation Molten Al. | | no damage | | no damage | |
| 256 | 20,000 | 6.10 | $5\frac{1}{2}$ | 14 | 4 | $10\frac{1}{4}$ | 2 & 2 | 5 5 | Bulge - Molten Al. | | no damage | | no damage | |
| 260 | 25,000 | 7.61 | $6\frac{1}{2}$ | $16\frac{1}{2}$ | $2\frac{3}{4}$ | 7 | 3 & 2 | $7\frac{1}{2}$ 5 | indentation Molten Al. | | no damage | | no damage | |
| 264 | 27,490 | 8.40 | $6\frac{1}{4}$ | $15\frac{3}{4}$ | $3\frac{1}{4}$ | $8\frac{1}{4}$ | $1\frac{1}{2}$ | $3\frac{3}{4}$ | slight bulge Molten Al. | | no damage | | no damage | |
| 269 | 30,250 | 9.22 | $5\frac{3}{4}$ | $14\frac{1}{2}$ | $3\frac{3}{4}$ | $9\frac{1}{2}$ | $1\frac{1}{2}$ | $3\frac{3}{4}$ | 1 | $2\frac{1}{2}$ | $1\frac{1}{2}$ Bulge - Molten Al. | $3\frac{3}{4}$ | no damage | |
| 270 | 30,200 | 9.20 | 7 | $17\frac{3}{4}$ | $4\frac{1}{2}$ | $11\frac{1}{2}$ | $2\frac{1}{4}$ | $5\frac{3}{4}$ | 2 1 & 4 bulge - molten Al. | 5 $2\frac{1}{2}$ $10\frac{1}{4}$ | several indentations Molten Al. | | no damage | |
| 271 | 31,250 | 9.54 | $6\frac{3}{4}$ | 17 | 5 | $12\frac{3}{4}$ | $2\frac{3}{4}$ | 7 | $1\frac{1}{4}$ | $3\frac{1}{4}$ | indentation Molten Al. | | no damage | |

damage pattern to the plate assembly. Damage to the individual sheets is shown (front view only) in the following four photographs of this figure. Figure 3.2a is a photograph of the lead bumper plate from this firing (260). The mean "hole" diameter in the first witness sheet from this series is seen to be approximately 6.5 ins (16.5 cms) (from Figure 3.2c and Table 2.1). However, if the petals forming the "hole" are flattened out, the resultant hole diameter involving actual material loss from the plate is less than about 2 ins (5 cms).

The complete series of photographs obtained with the B & W Model 192 camera from shot number 260 is presented in Figure 3.3. This figure consists of 70 individual photographs showing the impact of the projectile against the bumper plate, the formation and expansion of the "debris" cloud, and the subsequent interaction between the cloud and the first two witness sheets. As can be seen from this series, the impact cloud makes contact with the first bumper sheet (frame 13) some 7.6 μsec after the impact of the projectile against the bumper plate (frame 4), indicating an average cloud velocity of 34,000 ft/sec (10.4 km/sec). The first witness sheet is penetrated in the interval between frames 16 and 17, and the secondary expansion cloud contacts the second witness sheet at approximately frame 28 or 29. The mean cloud velocity in this interval is then approximately 17,000 ft/sec (5.2 km/sec) (assuming 2 ins (5.1 cms) spacing and 12 elapsed frames). Penetration of the second witness sheet by what appears to be a fragment from the first witness sheet, is seen to occur in the region of frame 39. Actual contact between the tertiary expansion clouds and

the third witness sheet is not seen in this series. By frame 70, the cloud appears to have travelled approximately 1 ins (2.5 cms) indicating that the average cloud velocity has been reduced to approximately 4,000 ft/sec (1.2 km/sec).

A more detailed picture of the flow characteristics of the primary and secondary expansion clouds may be seen in the selected and enlarged photographs of Figure 3.4. In this series, the experimental conditions were similar to those of Figure 3.3, except that the impact velocity was 30,000 ft/sec (9.15 km/sec) rather than the 25,000 ft/sec (7.61 km/sec) of the previous case. The first two frames of this series, 7.01 and 8.57 μsec after impact respectively, show contact between the primary cloud and the first witness sheet; the bright flash evident at the interface between the cloud and the sheet surface of the first witness sheet is seen to occur between frames 3 and 4, approximately 6 μsec after initial contact is made between the cloud and the first witness sheet. This latter observation implies that the peak pressure in the impact cloud occurs on the cloud centerline and, at the spacing, approximately at the center of the cloud. The pressure records obtained with the piezo-bar pressure gauge substantiate this observation.

The balance of the photographs in this series (Figure 3.4) shows the penetration of the first witness sheet, the reflection of the primary cloud from the first witness sheet, the early stages of the petalling failure mode, and the formation of the secondary expansion cloud. The observation is made that the reflected cloud is self-luminous (frames 6 to 8), and that an "impact flash" similar to that formed on the surface of the first witness sheet is formed on the back side of the bumper sheet by the reflected primary cloud.

Figure 3.5 is presented to show typical coverage of the multifoil firings

obtained with the STL Model ID image converter camera. Frames 3 and 4 of Figure 3.5b are of particular interest since they are photographs of the cloud shown in Figure 3.4 and correspond very closely in time to frames 1 and 3 of that figure.

The photographs presented in this series (Figures 3.2 to 3.5) are graphic examples of the importance of high speed camera coverage of the impact process. Figures 3.3 and 3.4, in particular, show the failure modes of the witness sheets. For example, Figure 3.4 indicates petalling angular velocities of the order of 40,000 radians per second in the first witness sheet (frames 4 through 11) after initial penetration of the plate. In Figure 3.3 (frames 31 through 48) evidence of penetration of the second witness sheet by fragments torn from the first sheet is seen. This latter observation is substantiated by inspection of the witness sheet assembly after a firing. In general, molten fragments of aluminum are found attached to the last one or two plates damaged by the process.

While no attempt has been made here to present a full analysis of the data obtained in this series, it is clear that even a cursory study of the data yields insight into the failure modes of the witness sheets. The mode of failure of the first witness sheet is seen to be that of initial penetration of the plate by the high pressure central core of the gas cloud, followed by extensive petalling. A much larger hole than that due to penetration alone is formed by the petalling action, as was observed in Figure 3.2b. During the petalling process, the individual petals are driven with such force that their angular velocity is sufficient to induce a tension failure in the material. A simplified

analysis, neglecting petal shearing forces, shows that a peak pressure of less than 10,000 psi acting over less than 20 μsec is sufficient to induce the observed petal angular velocity and angular displacement. The resulting centrifugal force in the petal is also shown to exceed the tensile strength of aluminum, thereby causing fragments to be torn from the petal tips.

A much more detailed analysis of the experimental findings, and more specific experimental investigations are required before detailed conclusions regarding the precise failure modes of the witness sheets can be made. The results presented in this section, however, should assist in the formulation of a theoretical model to predict the behaviour of a thin secondary surface, once the impulse from the primary expansion cloud has been specified.

As the multifoil system has been proposed as an alternative to the double wall structure it is important to comment on the relative merits of the two schemes. At low velocities such that the projectile will not be vaporized by the outer skin or shield, the multifoil system represents a viable concept. The penetrating power of a debris cloud consisting of small particles tends to remain constant with downstream spacing as damage is caused by individual punctures. Hence each thin sheet serves to dissipate the penetration capability of the debris, finally rendering it harmless.

A true vapor cloud, on the other hand, rapidly loses penetration capability with downstream spacing due to the decay of gas pressure occasioned by the radial expansion process. In round number 260, the multifoil system was penetrated up to plate number four, located 9 ins (22.9 cms) downstream of

the lead bumper. In an identical firing in which plates one, two and three were removed, integrity of plate number four was preserved. Thus no gain in protection has been achieved by the introduction of the additional upstream plates. It then appears that at impact velocities sufficiently high to create a true vapor cloud, the multifoil system represents an unnecessarily heavy protection scheme and that the double wall system is much to be preferred.

## 3.2 BUMPER THICKNESS EFFECTS

Pressure probe data from almost all impacts have revealed the presence of two distinct peaks in the center line profile. The previous final report (CR-54857) advanced two possible explanations for the existence of the second peak. The first explanation was the "engulfing theory". It was postulated that if a light material such as Lexan were to impact upon a dense material such as lead, the escape velocities of the shocked materials might be sufficiently different as to permit the more volatile Lexan to flow past and engulf the lead. Thus the first peak would correspond to the Lexan material while the second would correspond to the more slowly moving lead. Some substantation of this hypothesis was obtained in the form of good correlation between the calculated velocities of the two peaks and those determined experimentally.

Double peaks were observed, however, in like material impacts of Lexan on Lexan. In such a case the engulfing theory can offer no explanation in terms of mismatch. Consequently we have turned to the second hypothesis which suggests that the first peak is due to vapourized material while the second, slower peak corresponds to a particle-dominated flow resulting from incompletely vapourized

portions of the projectile. Thus we visualize the debris cloud as consisting of several material phases, i.e. a volatile gas phase capable of rapid free expansion and an inertia dominated mixture of solid and liquid phases. The gas phase will correspond to projectile and bumper material that has been processed by the initially strong wave system while the solid and liquid phases will correspond to material processed by a wave system that has been weakened by radial and axial rarefactions. We then expect that the rapidly expanding gas phase will cause the first pressure peak to decay with downstream spacing while the solid/liquid debris will be characterized by a pressure peak that depends only weakly on downstream spacing. Exactly such behaviour is observed in Figure 3.6. This series of photographs depicts pressure traces recorded at probe spacings of 3 ins. (7.61 cms), 6 ins. (15.24 cms), 9 ins. (77.86 cms) and 12 ins. (30.5 cms). The cloud was produced in each case by the impact of a Lexan projectile onto an 0.005 ins. (0.0127 cms) lead bumper at 25,000 ft/sec (7.6 km/sec).

It would be expected that utilization of a thicker bumper would sustain the initial high impact pressure for a longer time, thus reducing the amount of unvapourized material. In order to verify this conclusion we conducted a series of firings of Lexan projectiles into lead bumpers whose thicknesses varied between 0.002 ins. (0.005 cms) and 0.020 ins. (0.051 cms). The impact velocity was 25,000 ft/sec (7.7 km/sec) and the probe spacing was 6 ins. (15.2 cms). The pressure profiles are shown in Figure 3.7.

We see that the second peak is not present for the thicker bumper sheets. As the bumper thickness decreases the second peak increases in magnitude, and

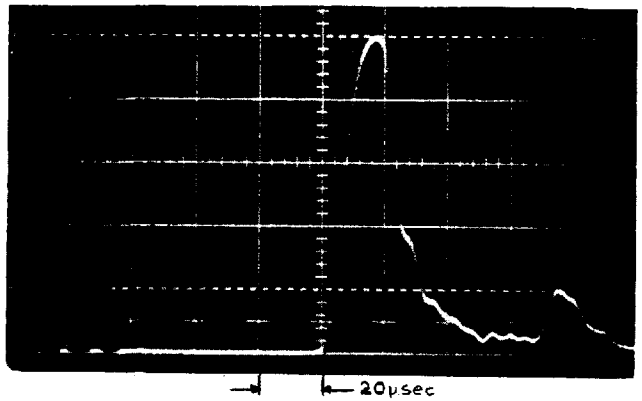


Subtracted Pressure Signal for Shot Number 302. The Impact is that of a 0.5 in.- Dia.(1.27 cm) by 0.285 in.(0.725 cm)- Long Lexan Pellet on a 0.005 in.(.127 mm) - Thick Lead Bumper at a Velocity of 25,880 ft/sec. (7.89 km/sec). The Probe was Located a Distance of 3 ins. Behind the Bumper. The Vertical Scale is 30,500 psi/cm and the Horizontal Scale is 20 μsecs./cm.

Piezo-Bar Output Trace (Upper Beam) for Shot Number 296. The Impact is that of a 0.5 in. - Dia. by 0.285 in.- Long Lexan Pellet on a 0.005 in. - Thick Lead Bumper at a Velocity of 25,800 ft/sec (7.86 km/sec). The Probe was Located a Distance of 6 ins. Behind the Bumper. The Vertical Scale is 25,000 psi/cm and the Horizontal Scale is 20 μsecs./cm.

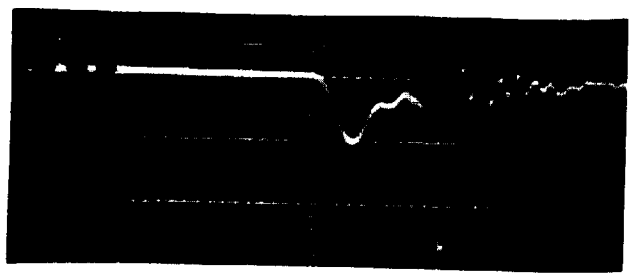

Subtracted Pressure Signal for Shot Number 297. The Impact is that of a 0.5 in. - Dia. by 0.285 in. - Long Lexan Pellet on a 0.005 in. - Thick Lead Bumper at a Velocity of 26,663 ft/sec (8.11 km/sec). The Probe was Located a Distance of 9 ins. Behind the Bumper. The Vertical Scale is 10,000 psi/cm and the Horizontal Scale is 20 μsecs/cm.

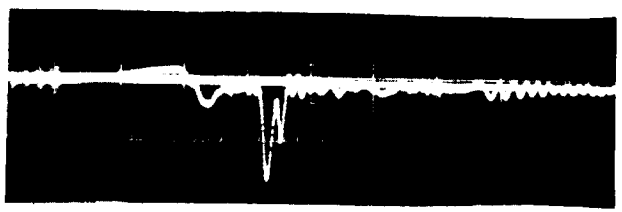

Piezo-Bar Output Trace (Upper Beam) for Shot Number 298. The Impact is that of a 0.5 in.- Dia. by 0.285 in. - Long Lexan Pellet on a 0.005 in. - Thick Lead Bumper at a Velocity of 25,900 ft/sec (7.8 km/sec). The Probe was Located a Distance of 12 ins. Behind the Bumper. The Vertical Scale is 10,000 psi/cm and the Horizontal Scale is 20 μsecs./cm.

FIG. 3.6 Piezo-Bar Traces for Spacings of 3, 6, 9 and 12 inches Shots 296, 297, 298 and 302

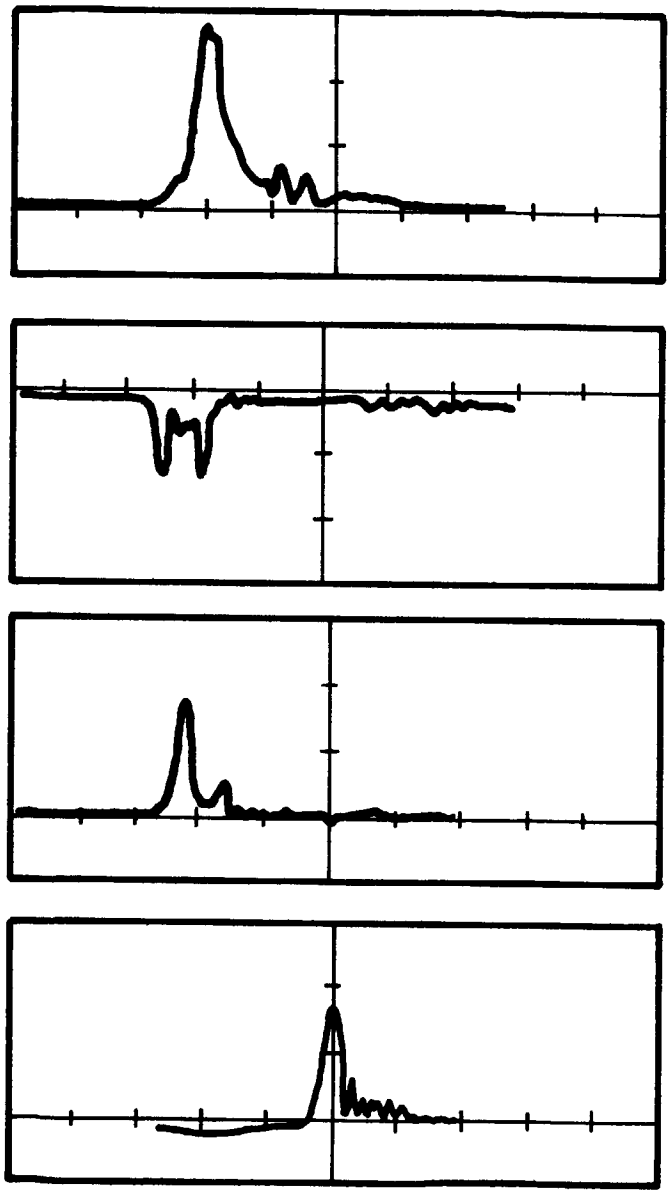

Shot No. 311 .00275 in. Lead Bumper

Peak Pressure 70,000 psi

Impact Velocity 22,000 ft/sec (6.71 km/sec)

Shot No. 296 .005 in. Lead Bumper (0.12 cm)

Peak Pressure 30,000 psi

Impact Velocity 25,300 ft/sec (7.71 km/sec)

Shot No. 104 .010 in. Lead Bumper (0.025 cm)

Peak Pressure 33,000 psi

Impact Velocity 24,600 ft/sec (7.49 km/sec)

Shot No. 306 .015 in. Lead Bumper (0.038 cm)

Peak Pressure 30,000 psi

Impact Velocity 24,100 ft/sec (7.34 km/sec)

FIG. 3.7 Effect of Bumper Thickness on Pressure for Impact of Lexan Cylinder on Lead Bumper. Probe Located 6 ins. (15.24 cm) Downstream.

at the minimum thickness bumper it essentially dominates the flow.

Additional evidence in support of the argument that the second peak is due to incomplete vaporization of the projectile can be found in the nature and apparent velocity of the second peak. The pressure records of Figure 3.6 show the second pressure pulse to be the result of a disturbance travelling at approximately 20,000 ft/sec (6.1 km/sec), 5,000 ft/sec (1.5 km/sec), less than the mean impact velocity. In addition, the pulse shape remains essentially sharp, indicating little or no expansion over the 12 ins. (30.5 cms) spacing covered by the pressure probes.

The experimental observations are in good agreement with the one-dimensional analysis of the projectile shock decay due to axial relaxation of the shocked projectile material (Reference 3.4). In this analysis it was shown that the Lexan projectile impacting against a 0.005 ins. (0.012 cms) thick lead bumper at 25,000 ft/sec (7.6 km/sec) would be completely vaporized only if the projectile length did not exceed 0.18 ins. (0.46 cms). For a longer projectile the shocked state enthalpy was shown to fall below the material vaporization energy, resulting in incomplete vaporization and fragmentation of the balance of the projectile (Figures 3.8 to 3.10). The analysis also showed that a full strength projectile shock would act only on the first ten bumper thicknesses (.05 ins) (0.13 cms) of the projectile, after which the decay process would begin to weaken the shock. It was assumed in this analysis that $\gamma = 3$, and that the critical shocked state pressure for complete vaporization was $1.5 \times 10^6$ psi (the vaporization energy of Lexan plastic is not well known, it has been established only that it lies between the limits of $3 \times 10^{10}$ and

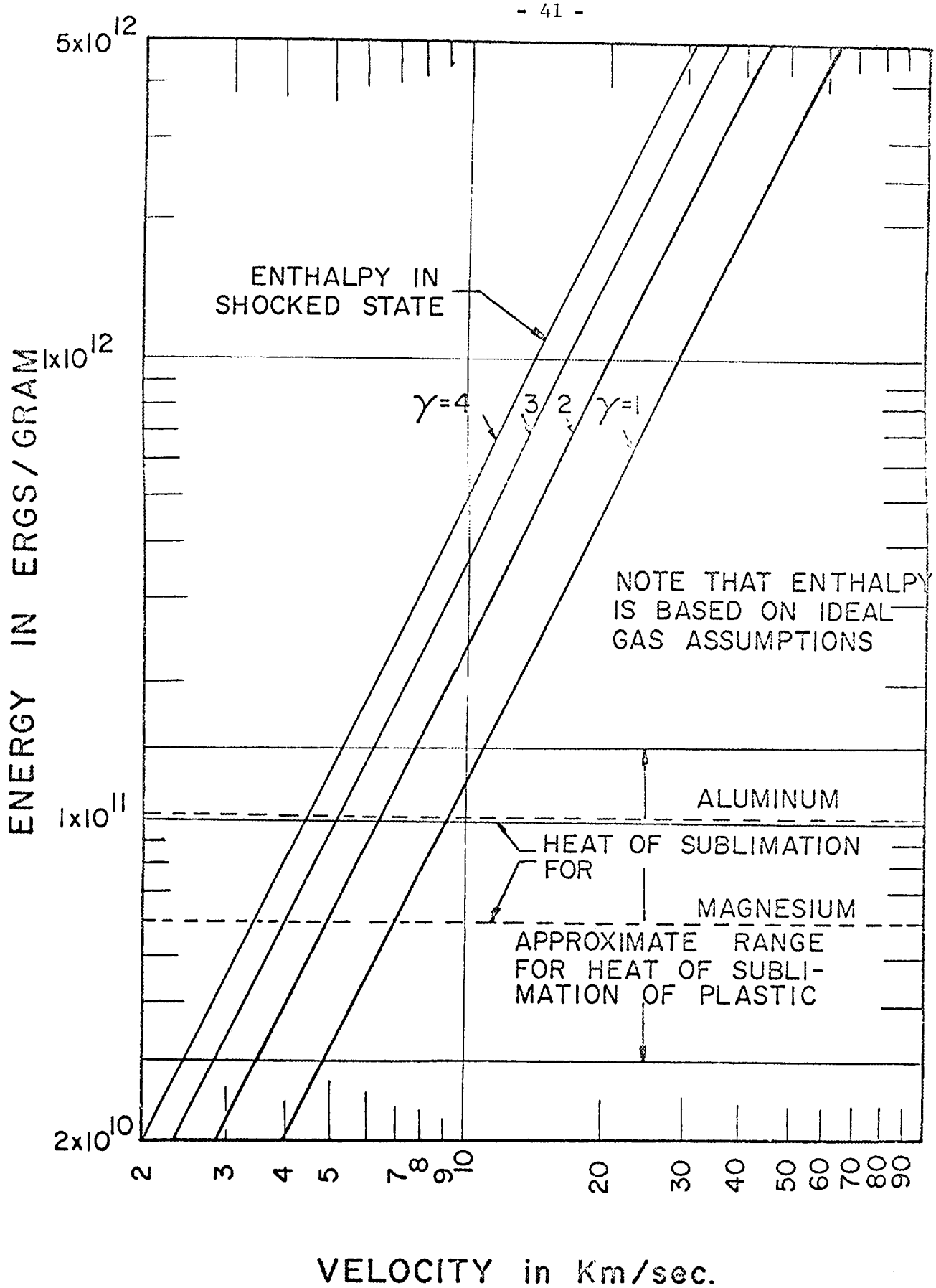


FIG. 3.8 Theoretical Plot of Shocked Energy vs Impact Velocity

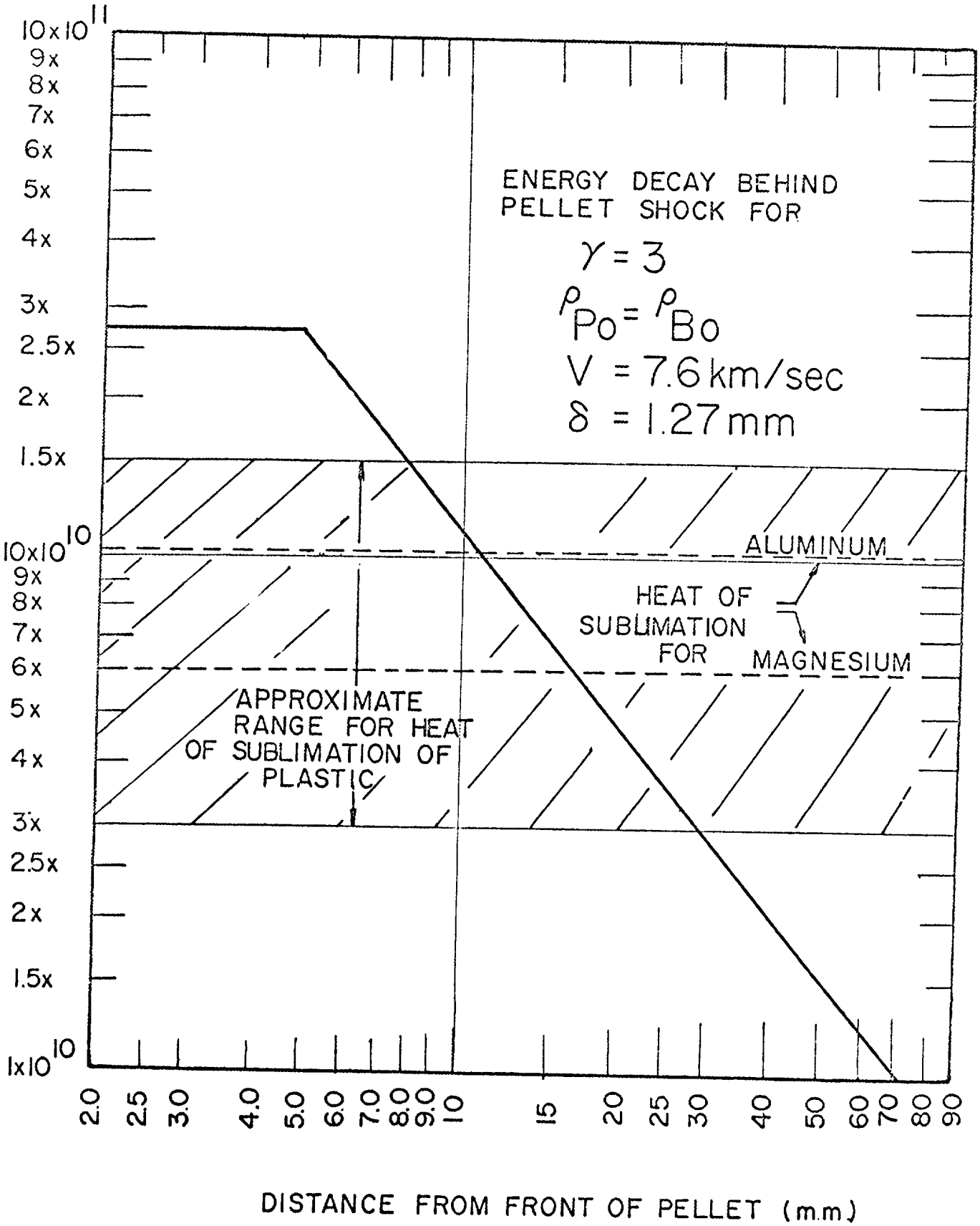


FIG. 3.9 Theoretical Plot of Shocked Energy Decay vs Distance Along Pellet

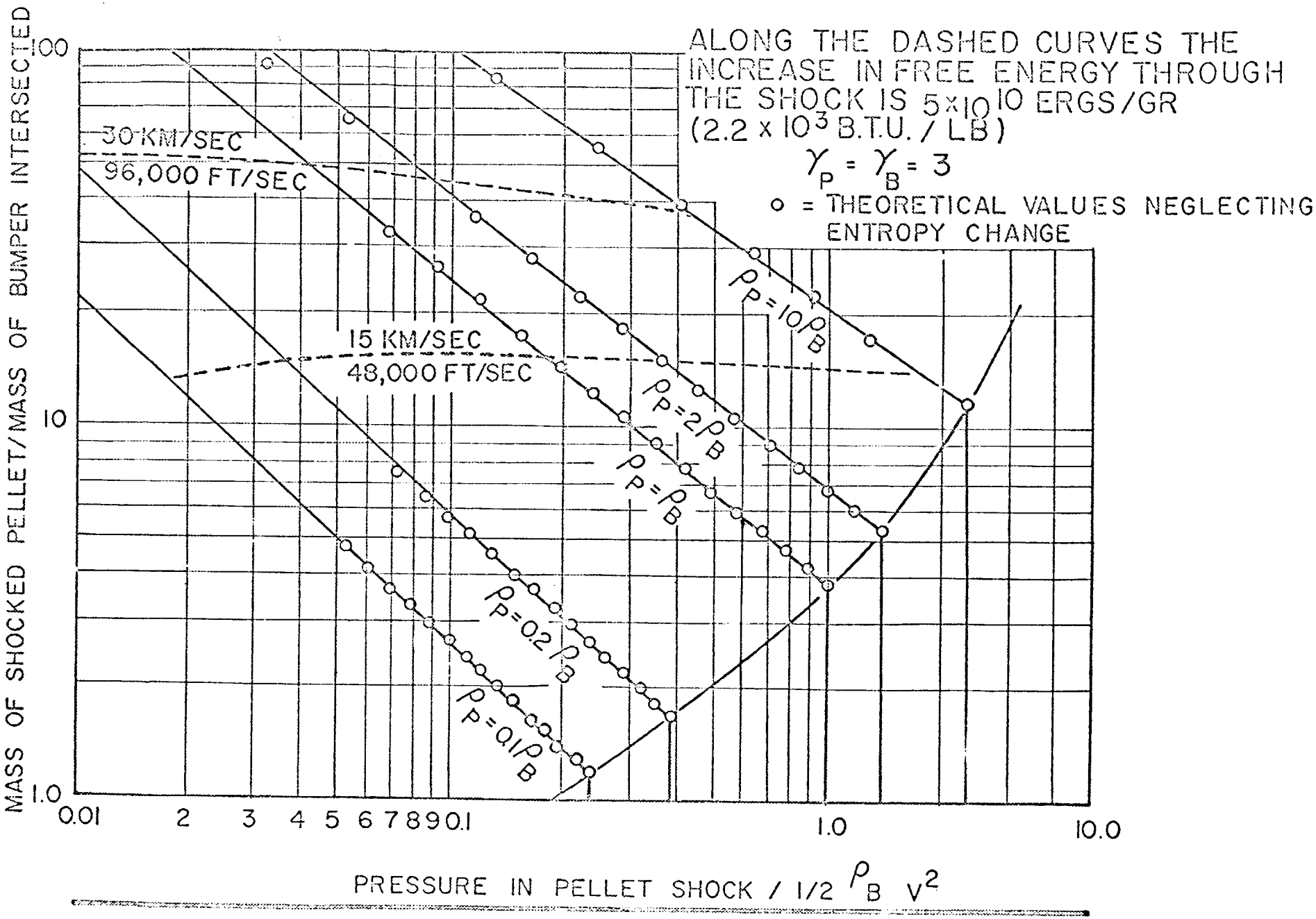


FIG. 3.10 PELLET SHOCK DECAY BY INTERACTION WITH ONE-DIMENSIONAL AXIAL RAREFACTION WAVES

$1.5 \times 10^{11}$ erg/gm).

In Figure 3.11 two additional pressure traces obtained during this series are presented. In Figure 3.11a the pressure trace shown is that from the impact of a 0.285 ins. (0.725 cms) long Lexan projectile onto a 0.010 ins. (0.025 cms) thick lead bumper at 30,200 ft/sec (9.20 km/sec). Note that a single pressure peak only is observed. At this velocity the one-dimensional analysis predicts that a total projectile length of 0.50 ins. (1.27 cms) (50 bumper thicknesses) will be completely vaporized. One pressure peak should therefore be expected, and one was observed.

Further substantiation of the incomplete vaporization explanation of the double peak pressure profile is seen when the pressure profiles for the impact of a Lexan projectile against a 0.010 ins. (0.025 cms) bumper at impact velocities of 30,000 and 25,000 ft/sec (9.15 and 7.62 km/sec) are compared. The second peak is observed only for the lower velocity case. The calculation of the shocked state enthalpy for the higher velocity case in the region near the rear face of the projectile indicates that complete vaporization is probable for this case.

## 3.3 IMPULSE LOADING ON SECONDARY SURFACE

Two series of firings were conducted in order to obtain secondary surface pressure distributions. The first consisted of firings of Lexan projectiles, 0.5 ins. (1.27 cms) in diameter by 0.285 ins. (0.725 cms) long, onto Lexan bumpers 0.030 ins. (0.076 cms) thick at velocities between 24,000 ft/sec (7.31 km/sec) and 30,000 ft/sec (9.15 km/sec). The witness sheet was spaced between 3 ins. (7.6 cms) and 12 ins. (30.5 cms) downstream of the bumper. The

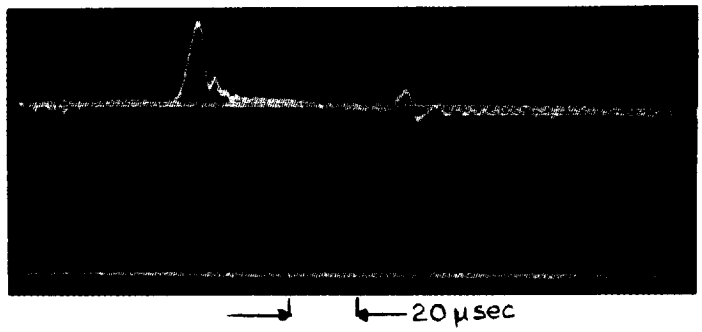


Fig. 3.11a Piezo-Bar Output Trace (Upper Beam) and Filter Probe Output Trace (Lower Beam) for Shot Number 300. The Impact is that of a 0.5 in.(1.27 cm) - Dia. by 0.285 in.(0.725 cm) - Long Lexan Pellet on a 0.010 in.(0.254 mm) - Thick Lead Bumper at a Velocity of 30,164 ft/sec (9.19 km/sec). The Probe was Located a Distance of 6 ins.(15.2 cm) Behind the Bumper. The Vertical Scale is 25,000 psi/cm and the Horizontal Scale is 20 μsecs/cm.

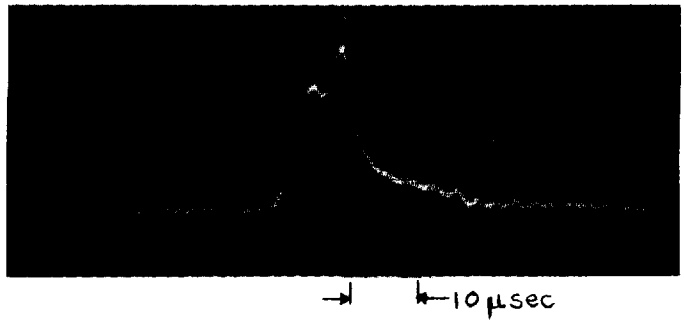


Fig. 3.11b Subtracted Pressure Signal for Shot Number 299. The Impact is that of a 0.5 in.-Dia. by 0.285 in. - Long Lexan Pellet on a 0.010 in. - Thick Lead Bumper at a Velocity of 30,100 ft/sec (9.17 km/sec). The Probe was Located a Distance of 3 ins. Behind the Bumper. The Vertical Scale is 42,800 psi/cm and the Horizontal Scale is 10 μsecs/cm.

second series was identical with the first except that the bumper was replaced by a lead sheet 0.010 ins. (0.025 cms) thick.

The experimental arrangement is shown in Figure 3.12. The secondary surface was an aluminum plate of thickness 0.25 ins. (0.64 cms). The four gauges were mounted in a horizontal plane, the tips being flush with the front of the secondary surface.

An example of one firing record of a Lexan/lead impact showing four pressure traces, the secondary surface and the cloud photographs is shown in Figure 3.13. The surface of Figure 3.14 represents the total pressure profile variation with time as the expansion cloud impacts against the secondary surface. The dotted lines on the profile surface "parallel" to the time axis are the three pressure traces obtained from Figure 3.13. Pressure is measured vertically from the zero pressure plane which contains the time and radial spacing axes, and which is outlined by the heavy line forming the base of the surface. Constant pressure profiles at intervals of 2,000 psi are shown on the figure as "horizontal" contours.

By integration of the pressure pulse over space and time one may calculate the total impulse experienced by the secondary surface. Such a calculation ignores the presence of any discrete particles in the flow. However, their contribution to the total impulse is expected to be small.

At any time after impact the cloud radius at the second surface may be determined photographically as R (t). Then the total impulse is given by

$$I = 2\pi \int_0^T dt \int_0^{R(t)} rp(r)\, dr$$

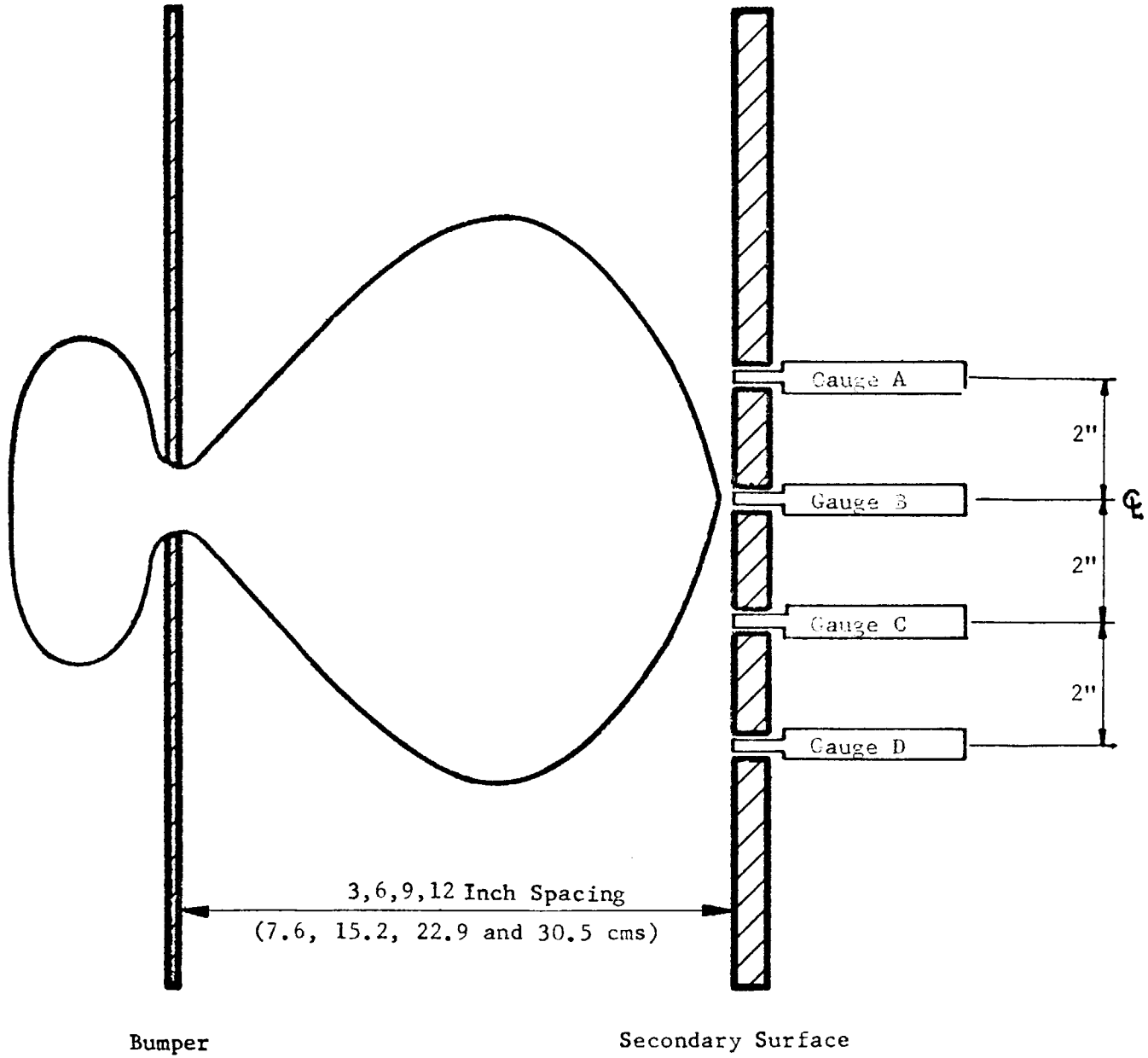


FIG. 3.12 Drawing of Pressure Probe Locations in Secondary Surface

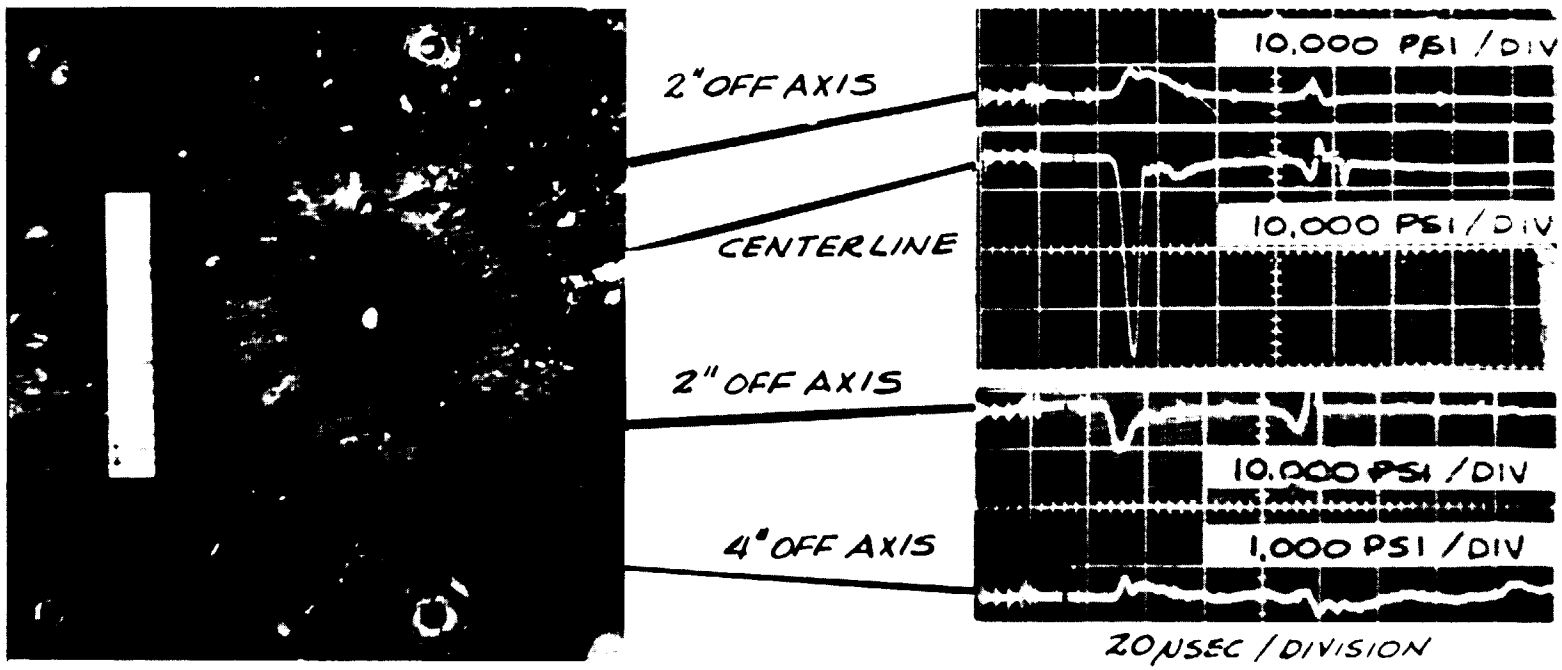


WITNESS SHEET - 6" SPACING

PRESSURE TRACES

SHOT Nº 391 V = 30,100 F.P.S. LEXAN → .010" Pb. BUMPER

FIG. 3.13a Piezo-Bar Traces for Off-Center Locations Shot 391. Lexan Cylinder 0.5 ins.(1.27 cm) Dia. 0.375 ins.(0.725 cm) long onto a 0.010 ins.(0.254 mm) Thick Lead Shield at 30,100 ft/sec (9.18 km/sec).

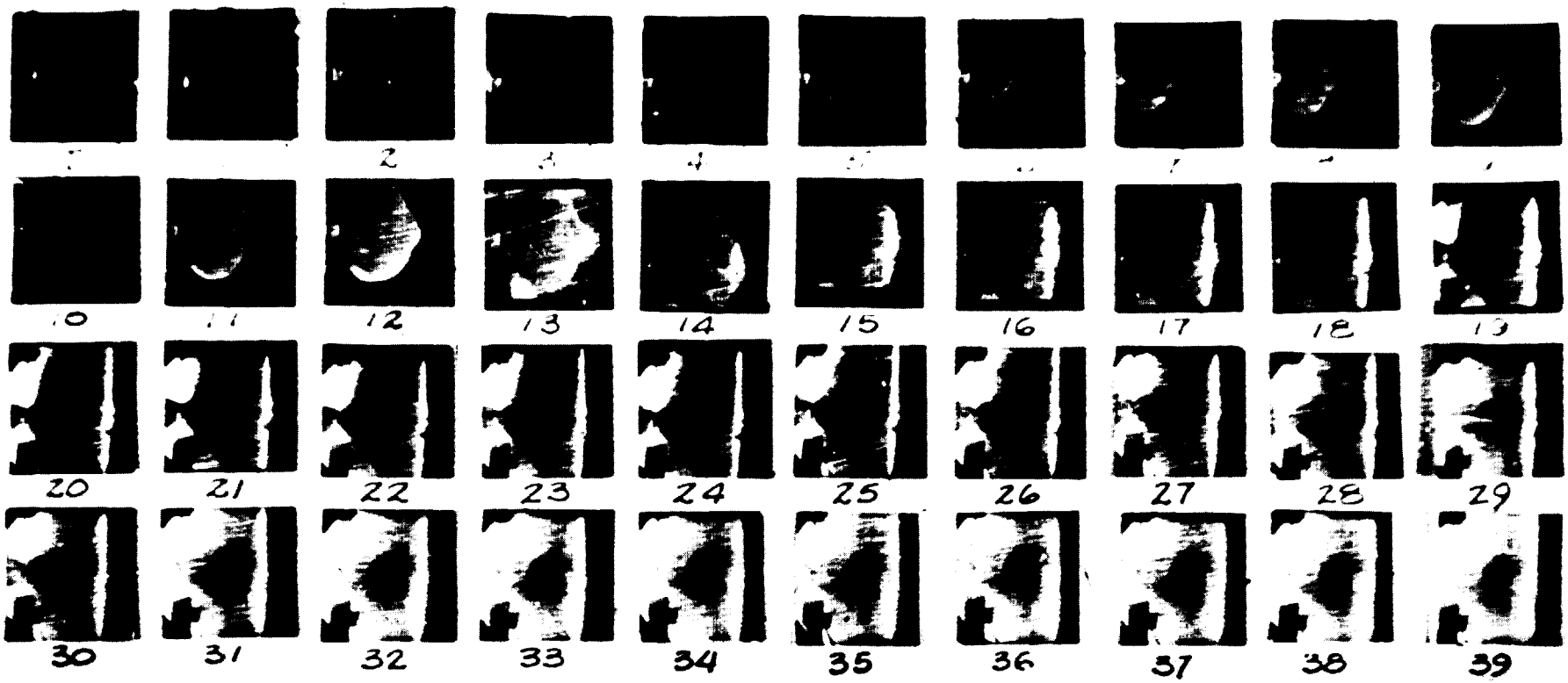


FIG. 3.13b Photographs of B and W 192 Coverage (Frames 1-39) Shot 391

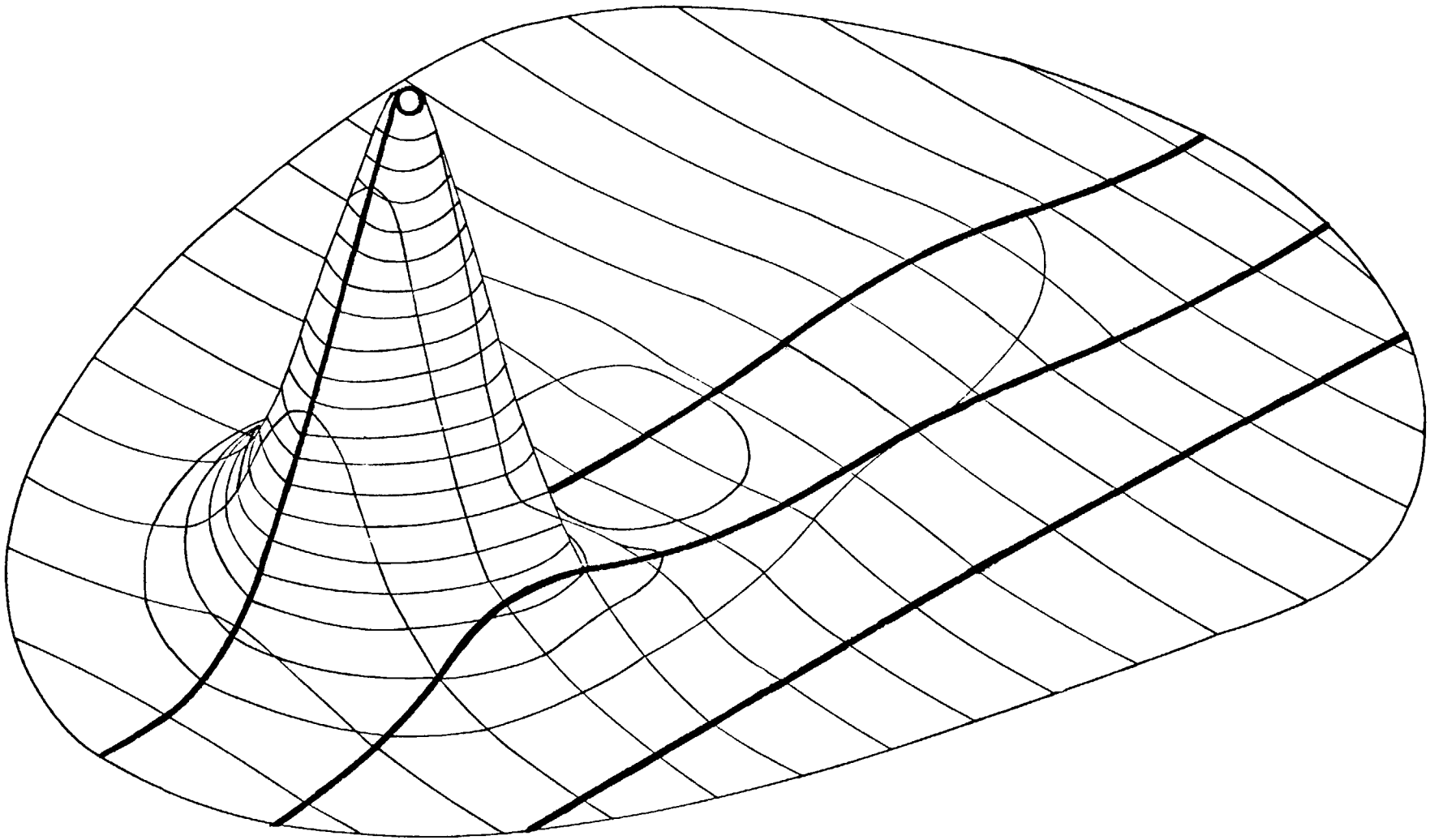

FIG. 3.14 Carpet Plot of Pressure Distribution in Impact Cloud

For the purpose of numerical integration we calculated the total force at a series of times and approximated the total impulse by

$$I = \sum_i \Delta t_i \left[ 2\pi \int_o^{R(t_i)} rp\ (r)\ dr \right]$$

The values of I determined in this manner are tabulated in Tables 3.2 and 3.3 for the Lexan/Lexan and Lexan/lead series respectively.

It is observed experimentally that the pressure distribution in a completely vapourized cloud may be approximated by a Gaussian in space and in time. Therefore we express the pressure distribution in the following manner.

$$p\ (r,t) = p_o \exp \{- \alpha r^2 - \beta (t - t_o)^2\}$$

where r is the radial spacing, t is the time and $p_o$ is the peak pressure on the centerline (i.e. at r = o and t = $t_o$) and $\alpha$, $\beta$ are constants to be determined.

The values of the constants $\alpha$, $\beta$ can be determined from plots of log $p/p_o$ versus $r^2$, $(t - t_o)^2$ respectively. Thus, having determined the constants in the expression, the value for the total pressure integrated over all time and space can be obtained.

$$\int_{-\infty}^{\infty} \int_o^{\infty} \int_o^{\infty} rp\ (r,t)\ d\theta\ dr\ dt = I$$

where I is total impulse and is given by

$$I = \frac{\pi p_o}{\alpha} \sqrt{\pi/\beta}$$

The results of this approach are given in Table 3.4. The total impulse for the Lexan/lead series obtained by this method agrees with that obtained

TABLE 3.2

Total Impulse on Second Surface From Pressure Gauge Measurements

| SHOT | VELOCITY (ft/sec) | SPACING (in) | PELLET MOM. (lb-sec) | IMPULSE (lb-sec) | MOM. MULT. FACTOR (Impulse/Pellet Mom.) |
|---|---|---|---|---|---|
| 434 | 24,000 (7.31 km/sec) | 3 ( 7.6 cm) | 2.15 | 3.15 | 1.46 |
| 430 | 25,500 (7.77 km/sec) | 6 (15.2 cm) | 2.05 | 2.43 | 1.19 |
| 433 | 24,000 (7.31 km/sec) | 9 (22.9 cm) | 1.93 | 3.05 | 1.58 |
| 437 | 30,500 (9.30 km/sec) | 12 (30.5 cm) | 2.44 | 2.91 | 1.19 |

TABLE 3.3

Total Impulse on Second Surface From Pressure Gauge Measurements

| SHOT | VELOCITY (ft-sec) | SPACING (in) | PELLET MOM. | IMPULSE (lb-sec) | MOM. MULT. FACTOR (Impulse/Pellet Mom.) |
|---|---|---|---|---|---|
| 421 | 25,400 (7.74 km/sec) | 3 ( 7.6 cm) | 2.07 | 5.56 | 2.70 |
| 391 | 30,000 (9.15 km/sec) | 6 (15.2 cm) | 2.47 | 2.61 | 1.06 |
| 394 | 30,600 (9.33 km/sec) | 9 (22.9 cm) | 2.53 | 2.11 | 0.83 |
| 399 | 25,800 (7.87 km/sec) | 12 (30.5 cm) | 2.13 | 1.44 | 0.68 |

TABLE 3.4

Total Impulse on Second Surface From Gaussian Approximation To Pressure Pulse

| SHOT | PELLET MOM. (lb-sec) | IMPULSE (lb-sec) | MOM. MULT. FACTOR (Impulse/Pellet Mom.) | $\alpha$ ($ins^{-2}$) | $\beta$ ($sec^{-2}$) $x10^{10}$ |
|---|---|---|---|---|---|
| 434 | 2.15 | 2.9 | 1.35 | 1.108 | 5.1 |
| 430 | 2.05 | 3.8 | 1.85 | 0.456 | 2.53 |
| 433 | 1.93 | 1.85 | 0.96 | 0.342 | 14.9 |
| 437 | 2.44 | 2.24 | 0.92 | 0.123 | 13.2 |
| 421 | 2.07 | 4.1 | 1.98 | 0.639 | 9.58 |
| 391 | 2.47 | 2.12 | 0.85 | 0.354 | 7.61 |
| 394 | 2.53 | 1.92 | 0.76 | 0.155 | 5.07 |
| 399 | 2.13 | 1.28 | 0.60 | 0.276 | 7.89 |

by the numerical technique, although the values are consistently smaller.

This is to be expected as no secondary peaks are included in the latter analysis. However, these secondary pulses could be included in a more elaborate mathematical expression which would give a better agreement.

The lack of agreement in the Lexan/Lexan series is due to the large secondary peak which corresponds to a particle-dominated flow resulting from incomplete vaporization of the projectile (see Section 3.2).

## 3.4 BAR AND DISC IMPACTS

A series of shots was performed, projecting cylindrical pellets onto cylindrical bumpers which were either comparatively thin (discs) or comparatively thick (bars). Projectile lengths were typically 0.5-in. (1.27-cm) while bumper thicknesses were 0.083-in. (0.21-cm) for discs and 1-in. (2.54-cm) for bars. The impacts were of like materials, namely Lexan on Lexan. Good Beckman and Whitley photographic records were obtained for some of these. Fig. 3.15 shows a time sequenced study of an impact onto a disc and Fig. 3.16 shows impact onto a bar. From the photographic records one is able to study visually shock propagation in the impacting media. One makes the assumption that as the shock wave progresses into either the pellet (Fig. 3.15) or the target bar (Fig. 3.16) the processed material behind it immediately expands into the ambient vacuum. One also supposes that the shock wave remains planar so that one-dimensional behavior is observed. Consequently, the position of the shock wave is considered to be indicated by the boundary separating solid from radially expanding material. The photographic data were reduced on a

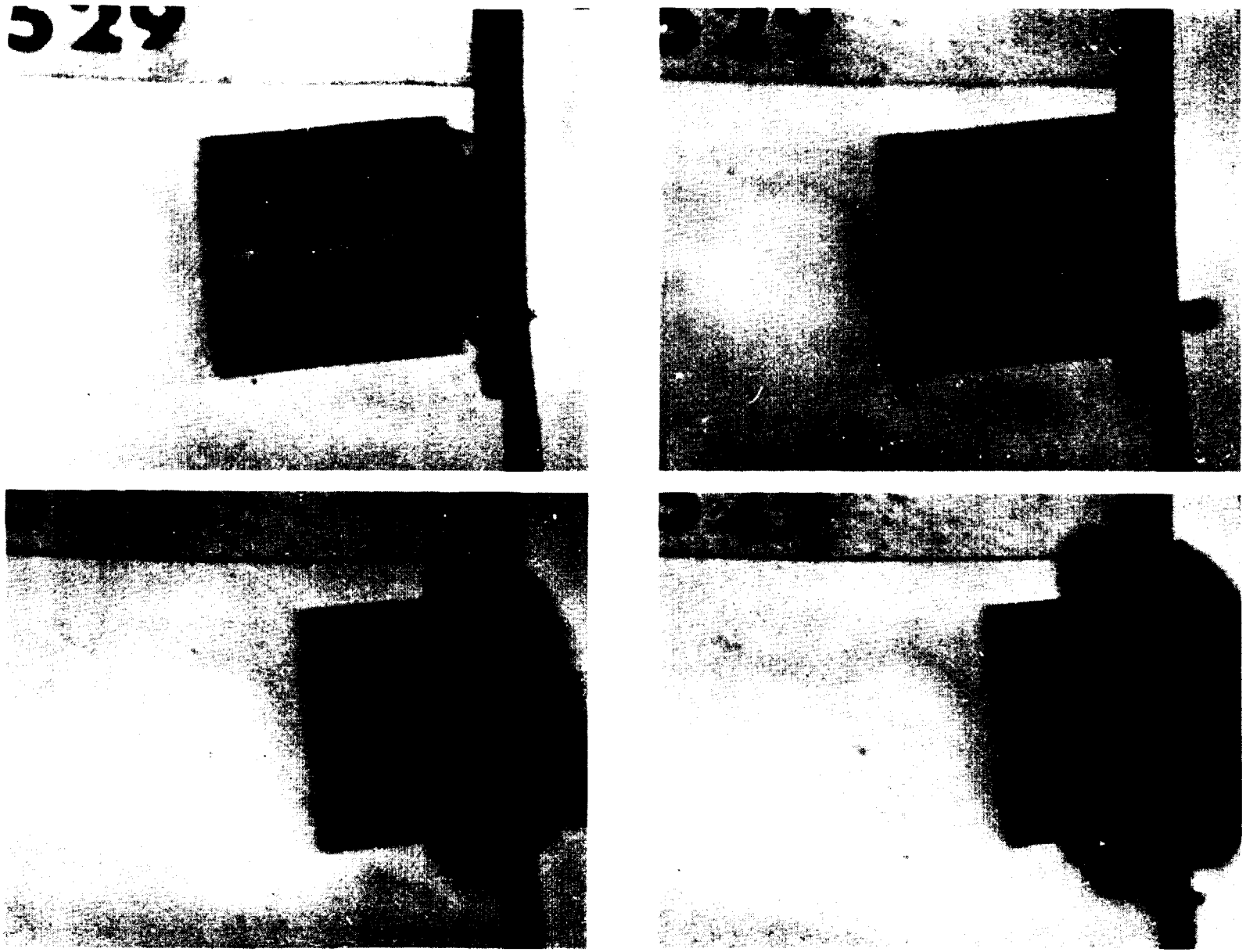


FIG. 3.15 Photographs of B and W 300 Coverage of a Pellet Impact on a Disc Shot 529

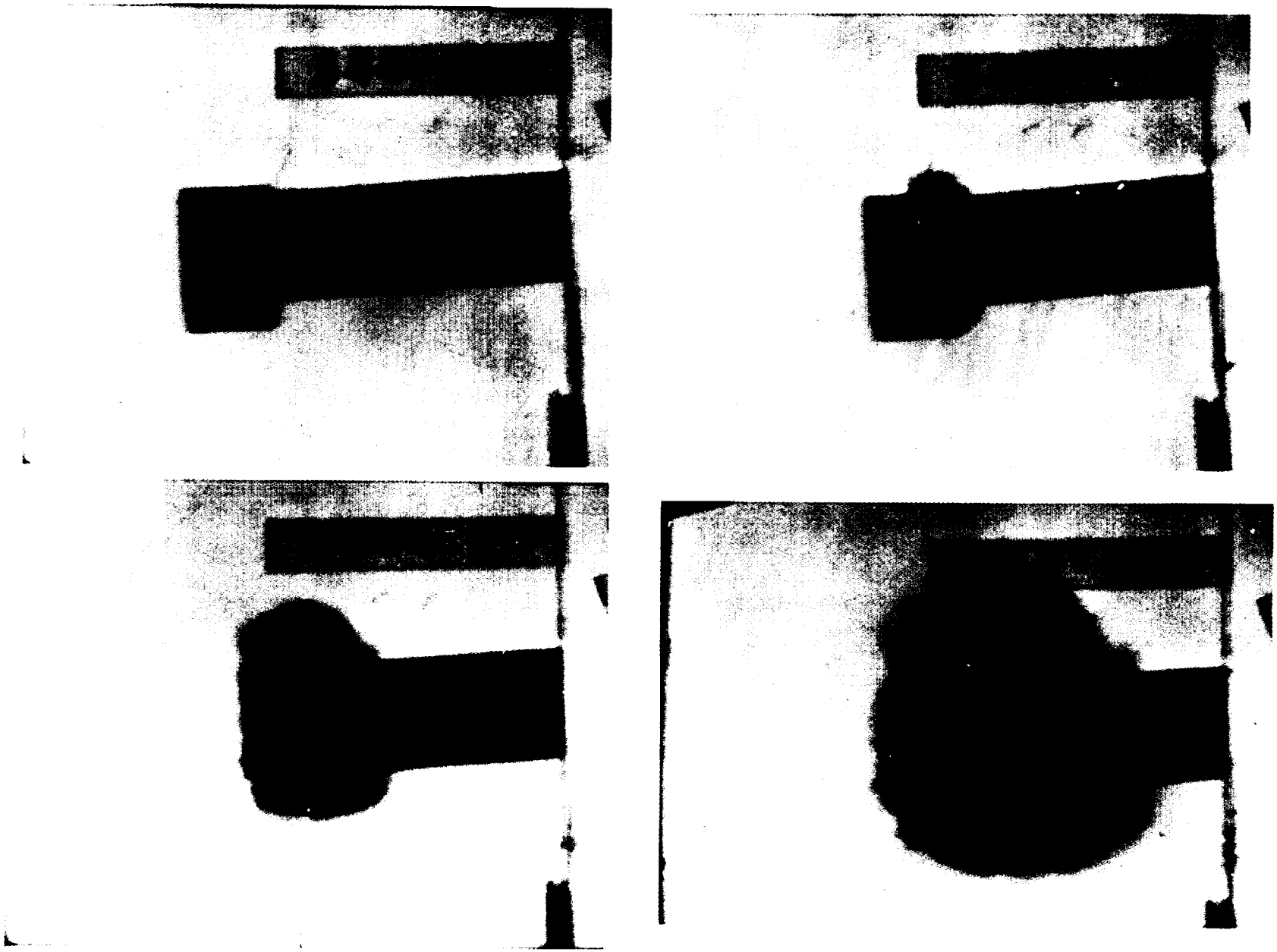

FIG. 3.16 Photographs of B and W 300 Coverage of a Pellet Impact on a Bar Shot 544

magnifying comparator and plotted in the one-dimensional wave diagram form of Fig. 3.17 (see Figs. 3.18 to 3.23). All quantities refer to the center-line of the cylindrical pellet.

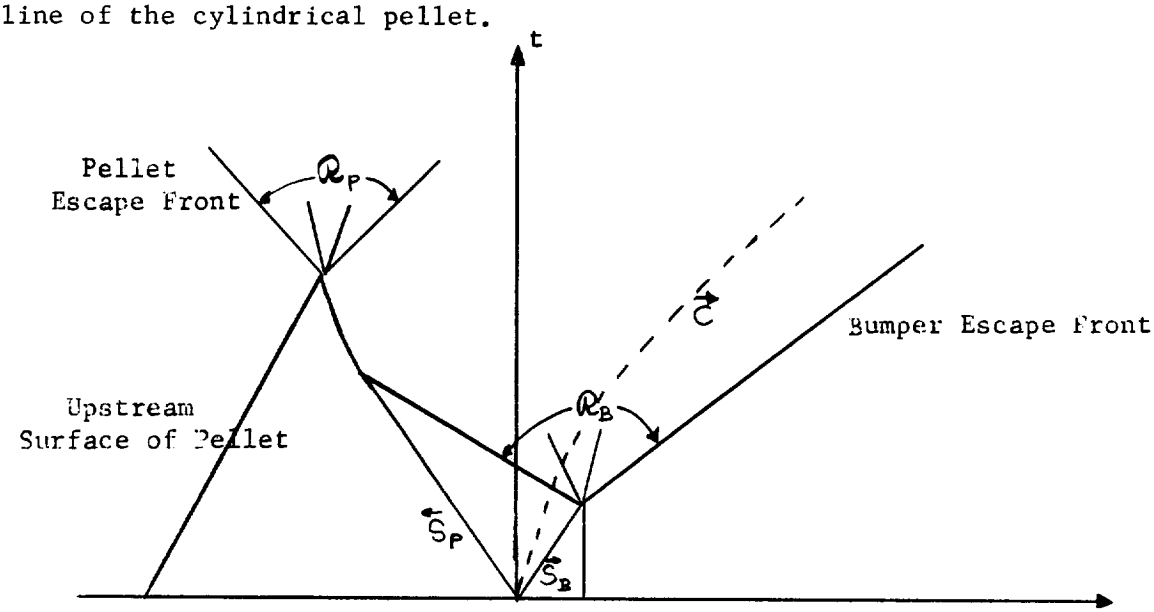


Figure 3.17 Wave Diagram For Impact Process

The surfaces which may be located photographically are the escape surfaces and the shock waves. We use the following notation: impact velocity = V; velocity of pellet shock = $\omega_P$ ; velocity of bumper shock = $\omega_B$ ; velocity of pellet escape front $U_{esc,p}$ ; velocity of bumper escape front $U_{esc,B}$ . All velocities are relative to the laboratory in which the bumper is initially at rest.

The data of Figs. 3.18 to 3.23 were analyzed on the basis of a one-dimensional hydrodynamic model (Ref. 4). In such a model the shocked density, pressure and velocity in the two media together with the shock wave velocities

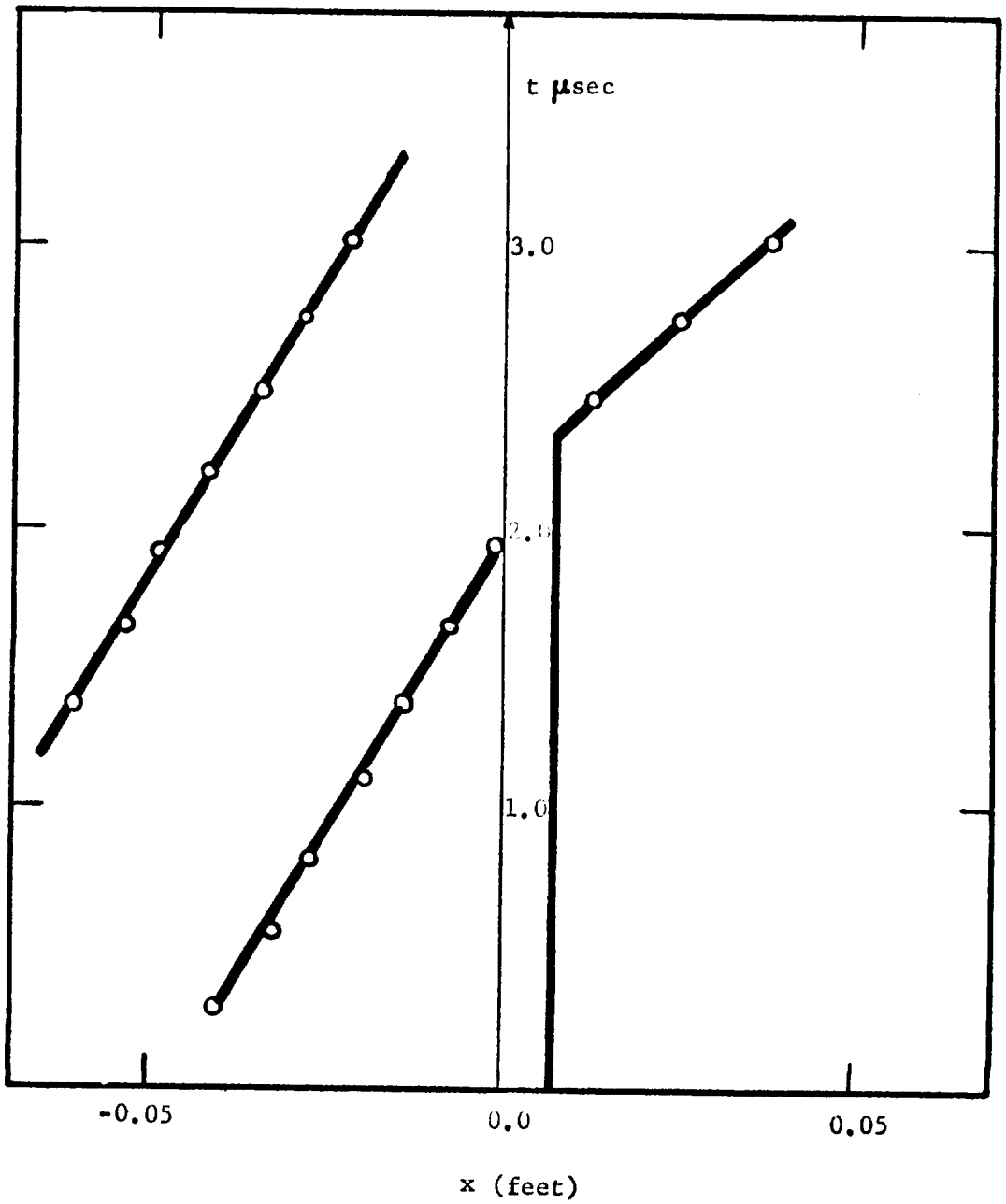


FIG. 3.18 Experimental Distance Time Diagram for Shot 528

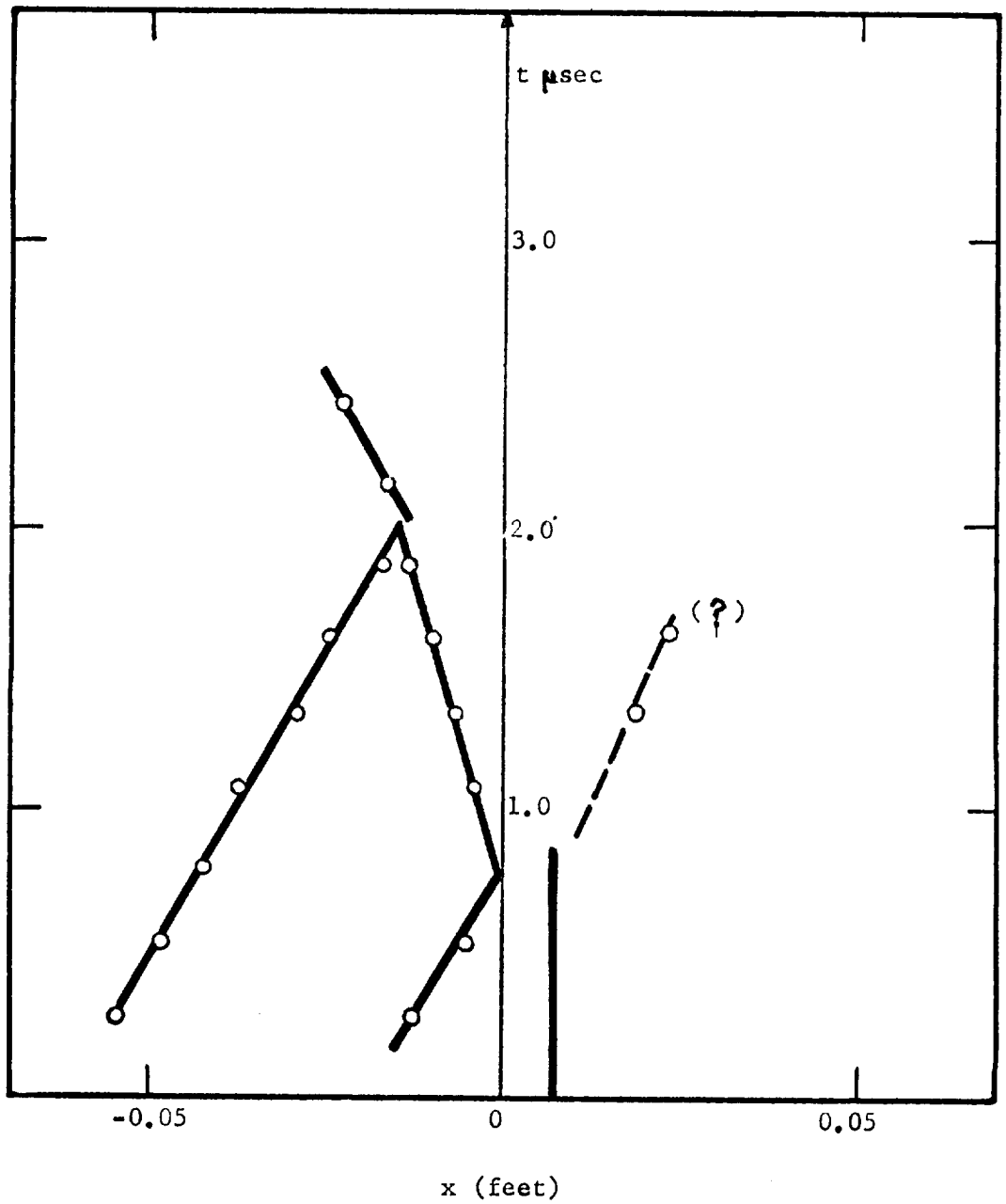


FIG. 3.19 Experimental Distance Time Diagram for Shot 529

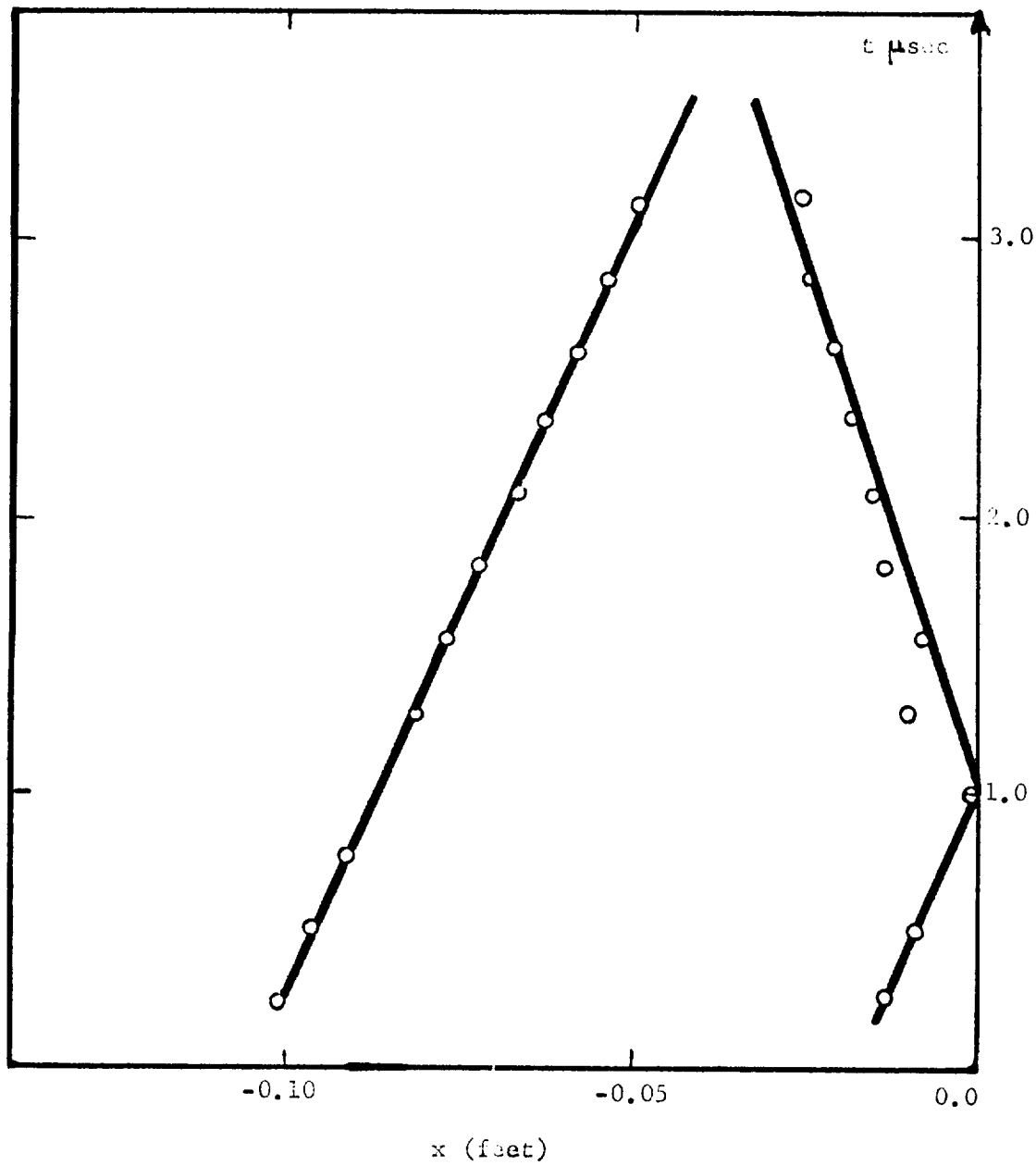


FIG. 3.20 Experimental Distance Time Diagram for Shot 533

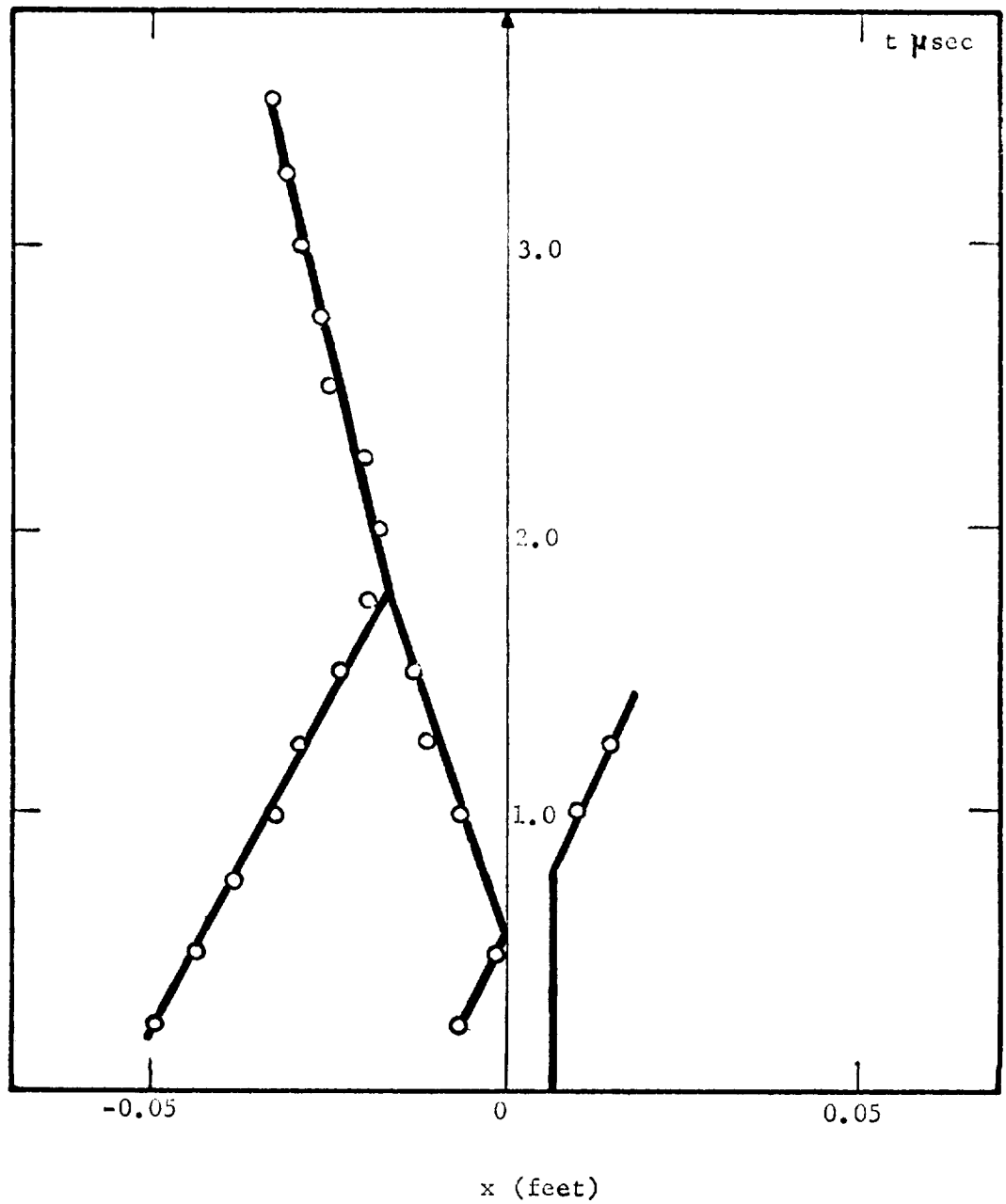


FIG. 3.21 Experimental Distance Time Diagram for Shot 538

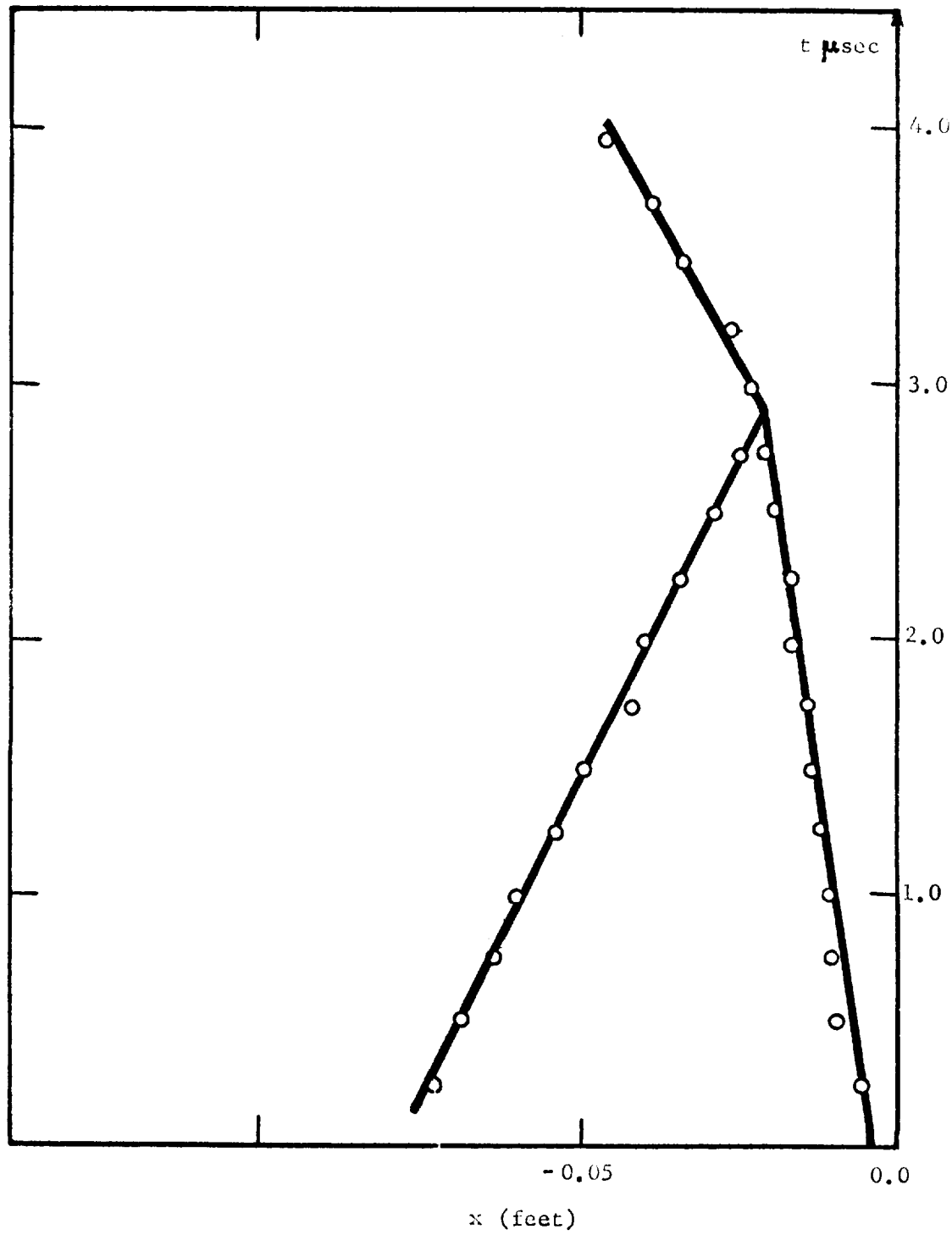


FIG. 3.22 Experimental Distance Time Diagram for Shot 539

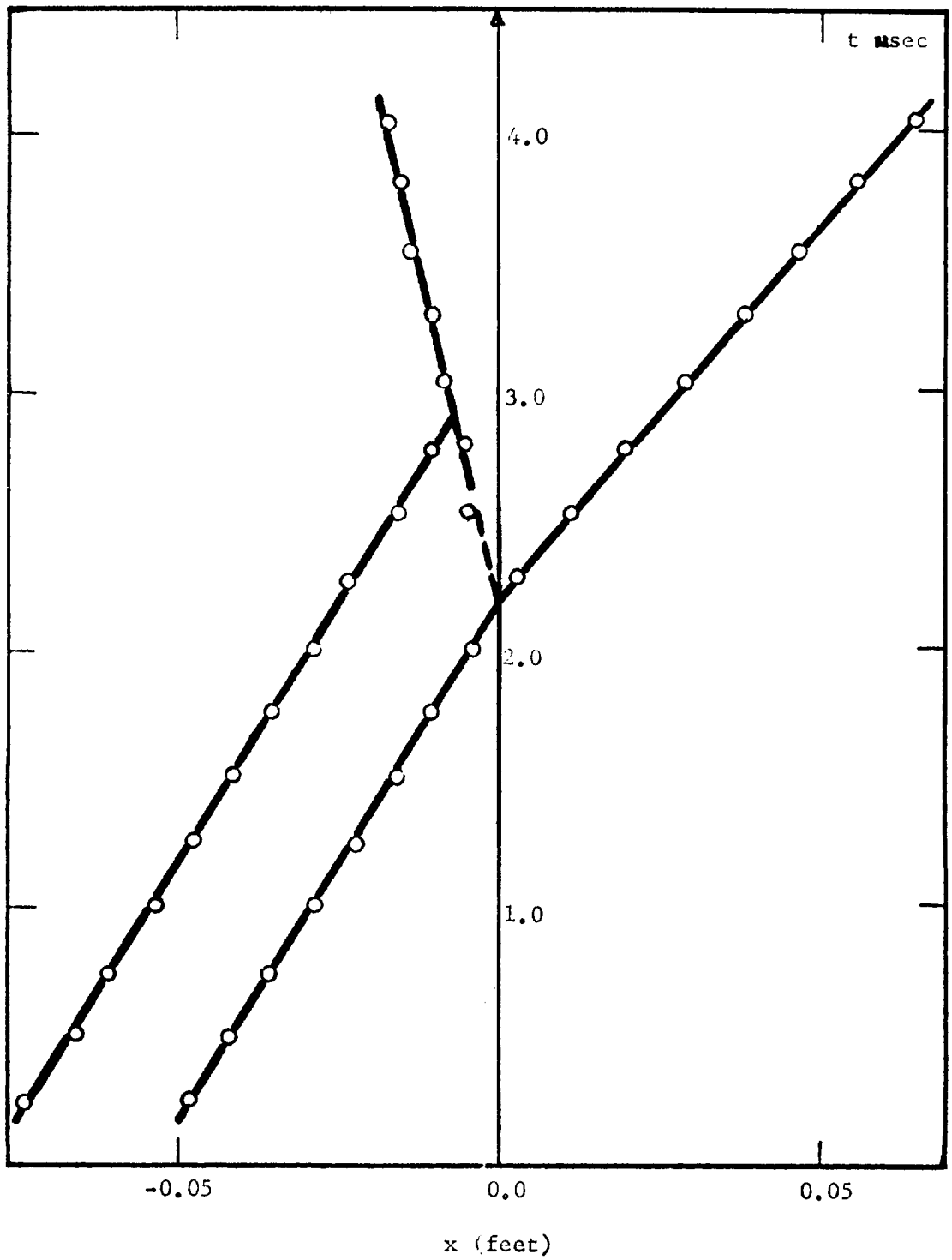


FIG. 3.23 Experimental Distance Time Diagram for Shot 544

constitute eight unknowns. From the continuity of pressure and particle velocity across the contact surface separating projectile and target media, and from the conservation of mass and momentum across each of the shock waves, one may determine the unknowns as functions of the shocked to unshocked density ratio in each medium. This may be done without reference to an equation of state. For the shots under consideration, the Mach number of the shock waves were of the order of 6 to 7 so that the wave may be regarded as a strong wave. If one wishes to use the ideal gas equation of state then one may write, in the strong shock approximation:

$$\frac{\rho_{final}}{\rho_{initial}} = \frac{\gamma+1}{\gamma-1} \qquad 3.4.1$$

where $\gamma$ is the polytropic gas constant. One may in any case make this identification so that the shocked quantities and the shock velocities are written in terms of the unknown $\gamma$ . One has, in particular, for a like material impact

$$\frac{\omega_B}{V} = \frac{\gamma+1}{4} \qquad 3.4.2$$

and

$$\frac{\omega_P}{V} = \frac{3-\gamma}{4} \qquad 3.4.3$$

Since the ratios on the left hand sides of equations (3.4.2), (3.4.3) may be determined from Figs. 3.18 to 3.23, values of $\gamma$ may be established empirically. It is to be expected that values of $\gamma$ determined in this way will produce nearly correct values for the density ratio (3.4.1) and for the

shocked pressure:

$$p = \frac{\gamma+1}{8} \rho_{initial} V^2 \qquad 3.4.4$$

Some deviation may be expected as the impact process will not be truly one-dimensional and the radial relaxation effects are not taken into account by this simple model. As a check on the one-dimensional nature of the process one may compare the density ratio determined from shock speed measurements with the ratio determined by estimating the compression directly from the photographs. The agreement is very good. In shot 544 (Fig. 3.23) for example, the density ratio from shock wave velocity measurements is 1.55 while that from compression measurments is 1.59. The values of $\gamma$ determined from measurments of wave speeds therefore enable one to specify the Hugoniot relation for the impacted material.

It is important to determine whether or not the value of $\gamma$ determined via (3.4.2), (3.4.3) may be actually interpreted as the polytropic gas constant in the ideal equation of state governing the compressed states of the impact process. A suitable test is provided by measurement of the escape velocities of projectile and target media along the impact velocity axis. A simple wave theory of expansion (Ref.5) predicts the following for a like material impact in which no shock decay occurs:

$$\frac{U_{escB}}{V} = \frac{1}{2} + \sqrt{\frac{\gamma}{2(\gamma-1)}} \qquad 3.4.5$$

and

$$\frac{U_{esc,p}}{V} = \frac{1}{2} - \sqrt{\frac{\gamma}{2(\gamma-1)}} \qquad 3.4.6$$

As in equations (3.4.2), (3.4.3), the left hand sides of equations (3.4.5), (3.4.6), may be determined from Figs. 3.18 to 3.23. Values of determined in this way may then be compared with the previous values for consistency. It is to be emphasized that equations (3.4.2), (3.4.3) do not depend on the equation of state, whereas (3.4.5) and (3.4.6) were derived under the explicit assumption of an ideal gas equation of state. In Fig. 3.24 we have plotted $\frac{\omega_B}{V}$ and $\frac{-U_{es,p}}{V}$ as functions of $\gamma$.

Due to the scattering of data in Figs. 3.18 to 3.23, the velocities determined in this way for the shock waves are accurate only to within 5 to 10%. An additional source of error in the Beckman and Whitley velocities arises from the determination of the interframe time. This may be alleviated by using the very accurate x-ray measurements to correct the Beckman velocities shot by shot.

In Table 3.5, we have reduced the graphical data of Figs. 3.18 to 3.23 to the velocities of the various waves and surfaces. (After correction by x-ray data).

TABLE 3.5

All Velocities are in ft/sec x $10^4$

| Shot No. | $V$ | $U_{es,B}$ | $U_{es,p}$ | $W_p$ | $W_B$ |
|---|---|---|---|---|---|
| 528 | 2.16 | 4.03 | - | - | - |
| 529 | 2.09 | 1.64 | - | 1.09 | - |
| 533 | 1.8 | - | - | 1.33 | - |
| 538 | 2.015 | 1.87 | 0.89 | 1.25 | - |
| 539 | 1.87 | - | 2.06 | 0.476 | - |
| 544 | 2.57 | - | 0.99 | 0.94 | 3.62 |

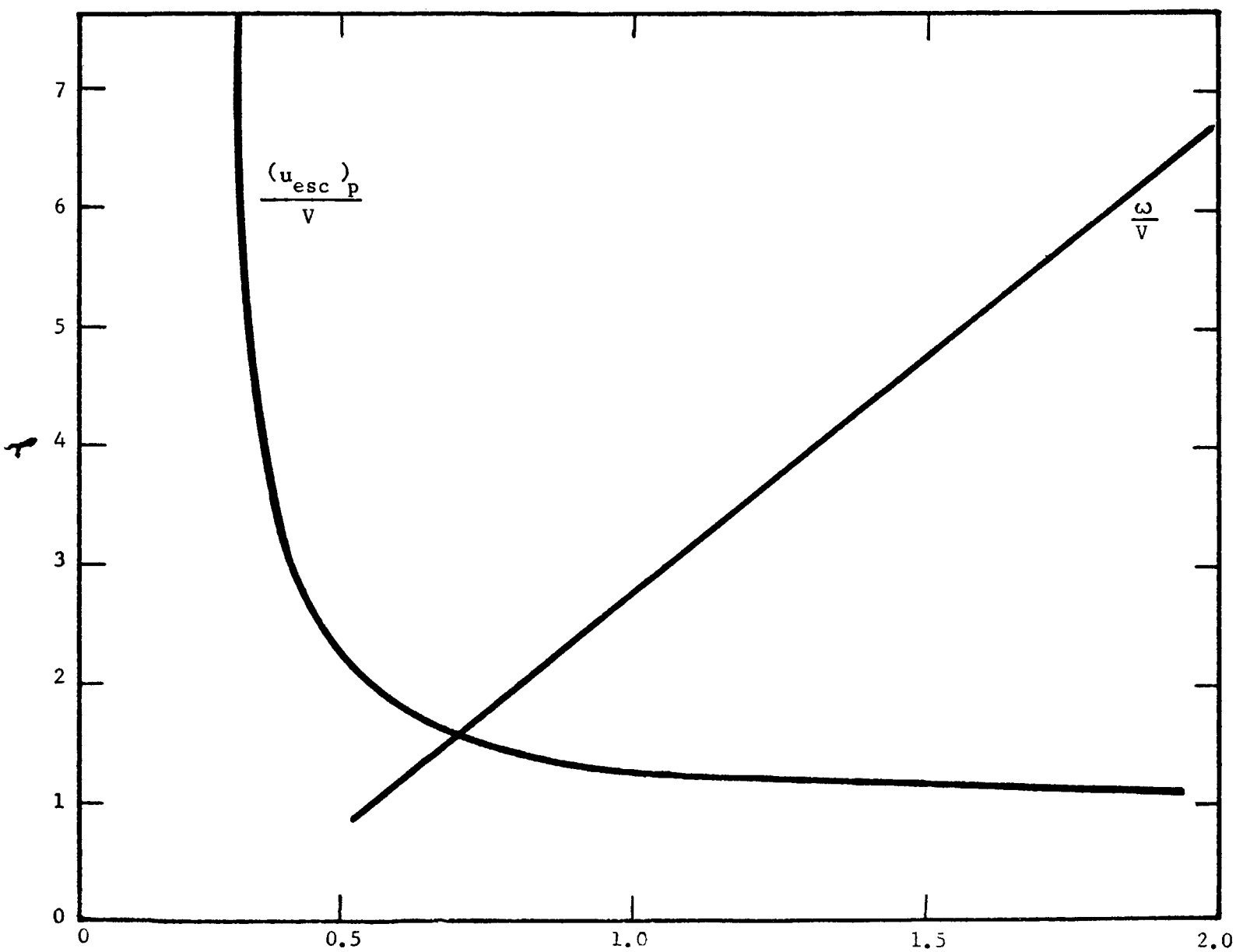


FIG. 3.24 Non-Dimensional Shock Velocity & Escape Velocity vs Polytropic Exponent $\gamma$

The data in Table 3.5 were further reduced by equations (3.4.2), (3.4.3), (3.4.5) and (3.4.6) to determine values of $\gamma$ . These values are listed in Table 3.6 in the column appropriate to their derivation. We have used a dash to indicate lack of source data while a question mark indicates that no physically real value of $\gamma$ could be found to agree with the source data.

TABLE 3.6
$\gamma$ Determined from

| Shot No. | $U_{es,B}$ | $U_{es,p}$ | $W_p$ | $W_B$ |
|---|---|---|---|---|
| 528 | 1.35 | - | - | - |
| 529 | ? | ? | 5.1 | - |
| 533 | - | - | 5.97 | - |
| 538 | ? | 2.3 | 5.53 | - |
| 539 | - | 1.22 | 4.05 | - |
| 544 | - | 2.8 | 4.5 | 4.65 |

As noted in equations (3.4.5), (3.4.6) the assumption has been made that no attenuation of the pellet shock has occurred. Obviously this cannot be true of the radial attenuation produced by lateral expansion. However, such an effect is not taken into account in a one-dimensional approximation. The model is capable, however, of commenting on attenuation due to the rarefaction generated at the bumper free surface. If $\delta$ is the bumper thickness, the bumper rarefaction will overtake the pellet shock at a time t after impact where

$$t = \frac{2 - \frac{4}{\gamma+1}\left[1 - \sqrt{\frac{\gamma(\gamma-1)}{2}}\right]}{\frac{1-\gamma}{2} + \sqrt{\frac{\gamma(\gamma-1)}{2}}} \frac{\delta}{V} \qquad 3.4.7$$

Consequently from equation (3.4.3) the minimum pellet length for decay to occur is given by

$$\ell = \frac{2 - \frac{4}{\gamma+1}\left[1 - \sqrt{\frac{\gamma(\gamma-1)}{2}}\right]}{\frac{1-\gamma}{2} + \sqrt{\frac{\gamma(\gamma-1)}{2}}} \frac{\delta(\gamma+1)}{4}$$

For a value of $\gamma$ equal to 6, $\ell/\delta$ is found to be 4.658. A smaller value of $\gamma$ would give a smaller value of $\ell/\delta$ so that we have used the largest likely value of $\gamma$. Consequently, shot number 533 (Fig. 3.18) should involve shock decay as this length criterion is more than satisfied. According to a one-dimensional finite difference model (Ref.5), although the subsequent decay in the shock pressure will be rapid, the trajectory of the pellet shock will deviate from a straight line very slightly. Hence we do not expect the graphical data (Figs. 3.18 to 3.23) to reveal any shock deceleration.. This would appear to contradict equation (3.4.4) which indicates that the value of p is dependent only on the compression which will be constant. However, p is coupled implicitly to the velocity of particles behind the shock. Equation (3.4.4) is only valid when there is no shock decay so that the shocked particle velocity for a like material impact is given by $\frac{V}{2}$. One should note, however, that the presence of axial decay in the strength of the pellet shock will invalidate the simple wave formula for the escape front velocity (equations 3.4.5. and 3.4.6). Also, as Zwarts has pointed out (Ref. 6), the $\gamma$ used in the density ratio formula is really a value averaged over all states intermediate between the initial and final states. The value of $\gamma$ used for the escape front velocities, on the other hand, refers exclusively to the impacted states. Consequently, even if the ideal gas formula governs the thermodynamics of the impacted media, one may expect inconsistencies in the values of $\gamma$ appropriate to the different phenomena.

From Table 3.6 we conclude that there is, in fact, very little correlation between values of $\gamma$ determined from shock wave velocities and those determined from escape speeds. In some cases no physically real $\gamma$ may be found to produce

the observed value of the escape speed. This may be due to shock decay as noted above. However, it is extremely unlikely that axial decay of the pellet shock occurs in shot number 544 as the bumper is three times the length of the pellet. Also, the escape speed of the pellet free surface is determined from data consisting of several measurements with comparatively little scatter. But the values of $\gamma$ in shot number 544 determined from the two shock wave velocities agree very poorly with those determined from the escape speed measurements.

The value of $\gamma$ determined from equations (3.4.2), (3.4.3) have been plotted in Fig.3.25 vs impact velocity. The trend is quite consistent except for that value of $\gamma$ corresponding to shot number 539 which is too low. But as is apparent from Fig. 3.22, the data for the pellet shock in shot number 539 scatters considerably. The decreasing value of $\gamma$ as the impact velocity increases indicates increasing compression with increasing impact velocity. Thus although the initial shocks may be regarded as being strong, we cannot describe the Hugoniot in terms of an ideal gas formulation, at least within the range of velocity discussed above. In order to employ an ideal gas Hugoniot it would be necessary that the polytropic exponent vary only slightly with velocity. It would be of great interest to extend the data to include higher velocities to see whether $\gamma$ actually does approach a limiting value within the experimental velocity regime.

In Fig. 3.26 we have plotted out the pressure against the compression to determine the Hugoniot relation for the shocked states in Lexan. It is recognized, of course, that the present data is limited both in quantity and in accuracy. It would be most desirable to instrument a target to determine

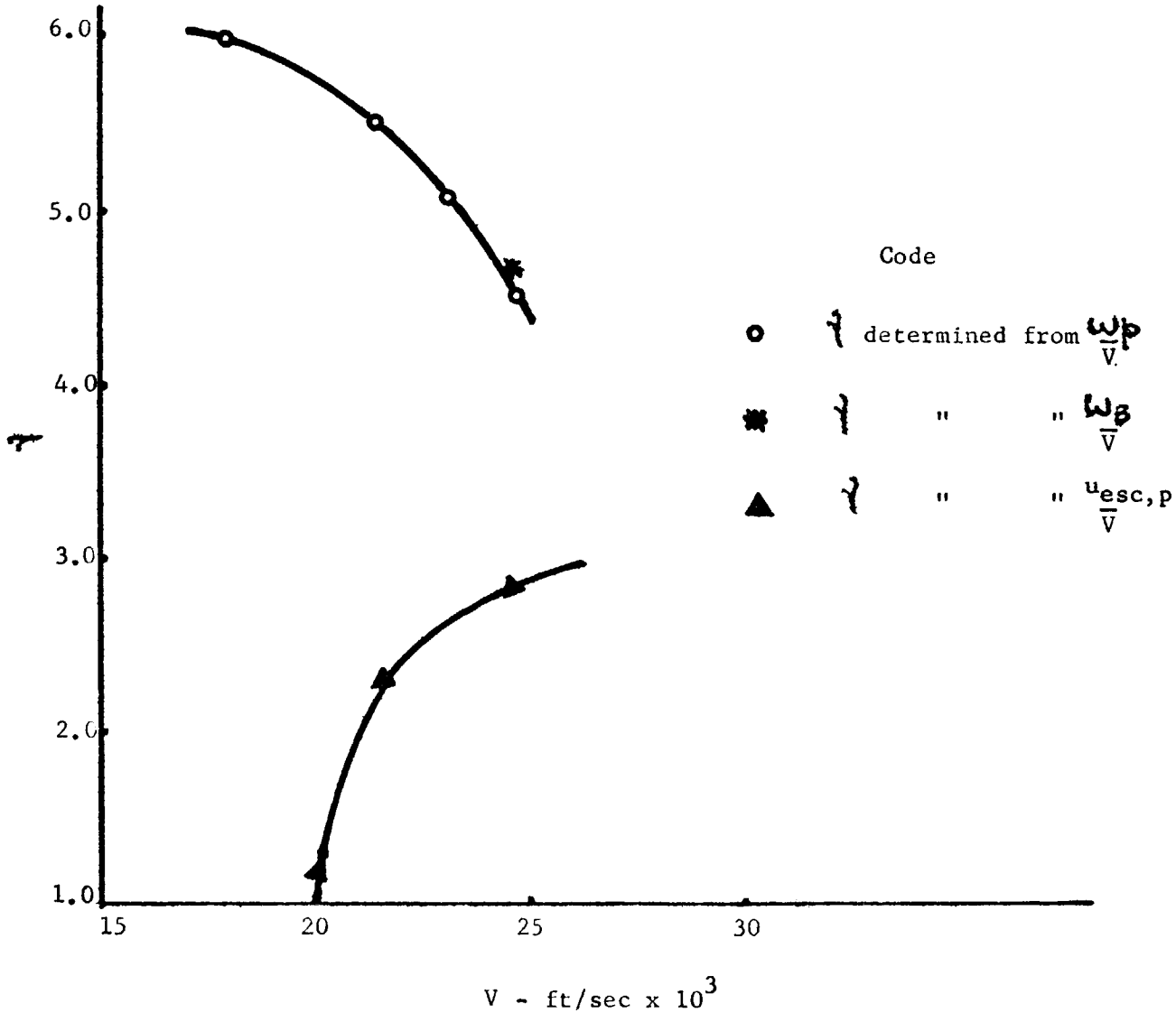


FIG. 3.25 Polytropic Exponent $\gamma$ vs Impact Velocity

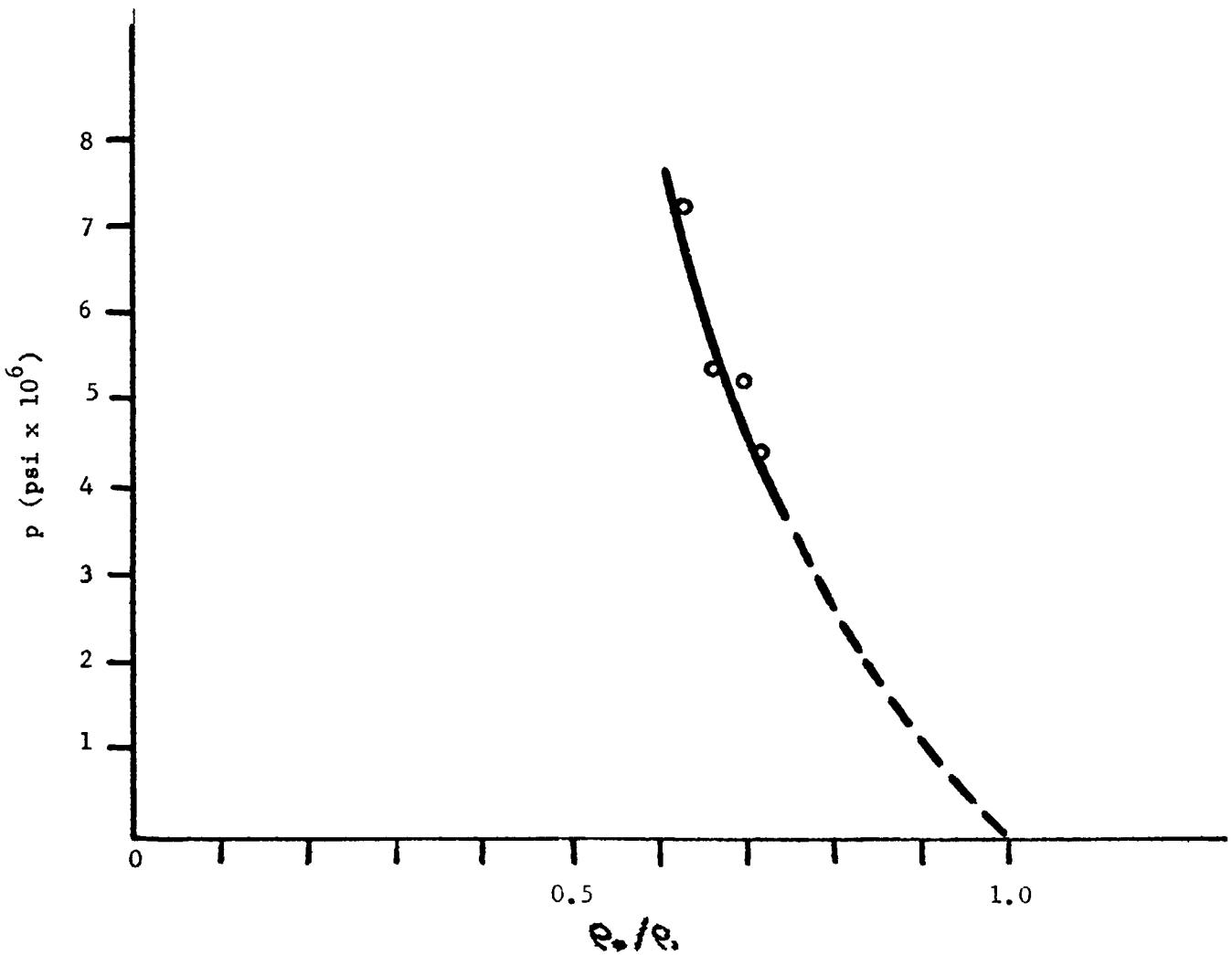


FIG. 3.26 Hugoniot for Lexan

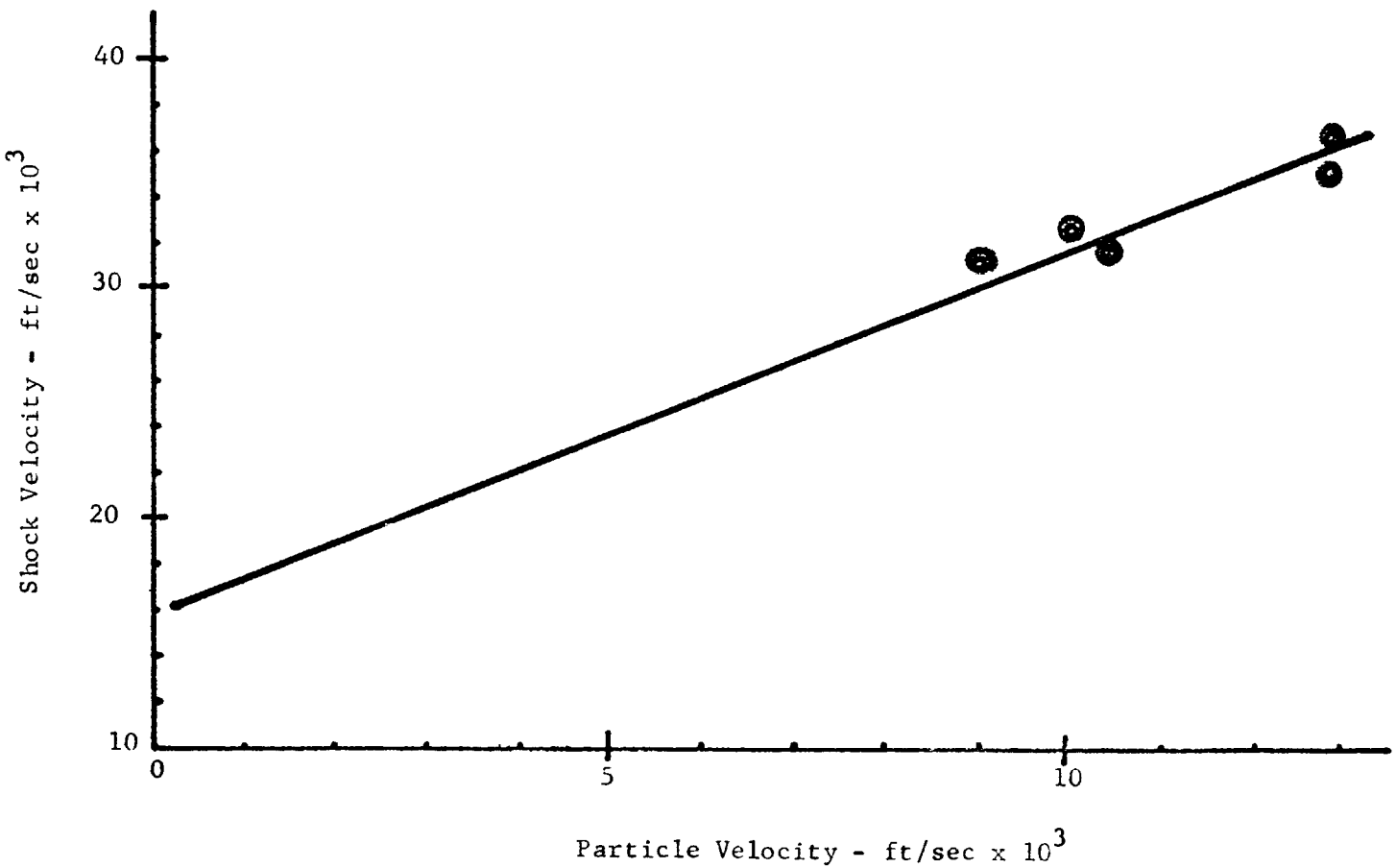


FIG. 3.27 Shock Velocity vs Particle Velocity for Lexan

the shock velocity more accurately and also to verify the assumption that the shock position is indeed denoted by the radial expansion boundary.

In Fig. 3.27 we have presented the data in a different form. For most materials the relationship between the shock velocity $\omega_s$ , and the shocked particle velocity, $u_p$ , takes the form

$$\omega_s = c + su_p$$

This linear relationship is valid over a wide range of shock strengths.

## 3.5 SHAPE EFFECTS

The series of firings in which lexan projectiles with conical and inverted conical front faces were impacted against lead bumper sheets, and the results compared with firings of cylindrical projectiles of the same mass yielded interesting results from both cloud pressure measurements and secondary damage distributions.

The program consisted of firing five projectile shapes, each having the same total mass, against 0.010 in. (0.25 cm) lead bumper sheets and comparing the spray and pressure distributions on a secondary surface. The projectile shapes are shown in Fig. 3.28 along with some representative centerline pressure profiles.

The inverted cone impacts are seen to "focus" the cloud material along the cloud centerline, whereas, the "pointed" projectiles resulted in substantially lower centerline peak pressures. These observations are in direct opposition to results predicted by numerical analyses which do not consider impact velocities sufficiently high to produce material vaporization, but are in good agreement with more recent calculations by Riney (Ref. 7) for impact

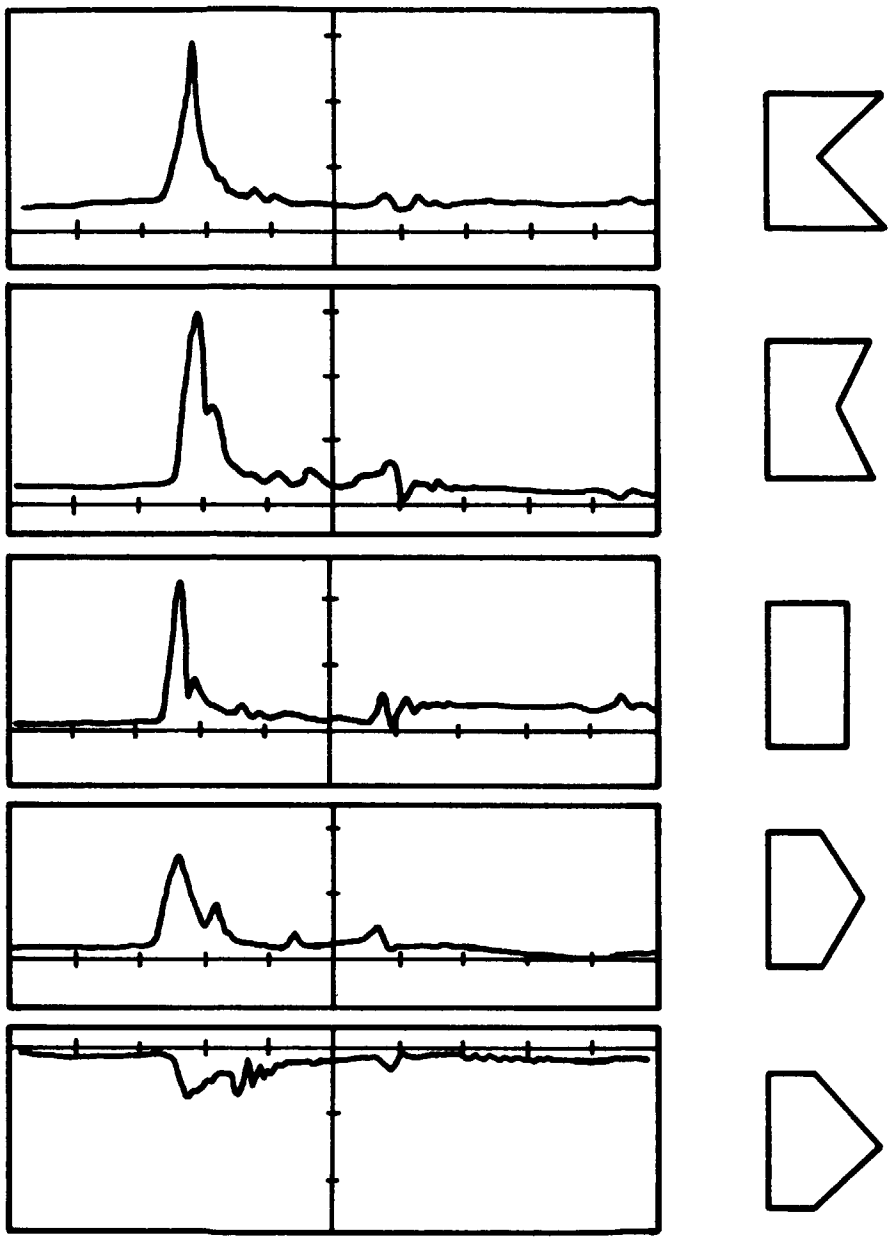



Shot 340 — Velocity 25,300 ft/sec (7.71 km/sec)
$90^{\circ}$ - Cone — Pressure 70,000 psi

Shot 341 — Velocity 26,000 ft/sec (7.92 km/sec)
$135^{\circ}$ - Cone — Pressure 70,000 psi

Shot 356 — Velocity 28,600 ft/sec (8.72 km/sec)
Cylinder — Pressure 40,000 psi

Shot 364 — Velocity 27,500 ft/sec (8.38 km/sec)
$135^{\circ}$ + Cone — Pressure 35,000 psi

Shot 337 — Velocity 27,000 ft/sec (8.23 km/sec)
$90^{\circ}$ + Cone — Pressure 18,000 psi

FIG. 3.28 Piezo-Bar Traces Showing Shape Effects Shots 340, 341, 356, 364, 337

velocities above minimum material vaporization requirements. The inverted cone impacts, in addition to concentrating the cloud material along the cloud centerline as shown by the pressure profile measurements and the witness plate damage, produced a high concentration of particles in a narrow region around the cloud core. The witness sheet damage observations showed that the "particle ring" diameter depended on the impact velocity as well as on the projectile shape. No particle concentrations were observed from the pointed projectiles, or from the control cylindrical projectile at the higher velocities.

That the particle ring concentration was less severe for the higher velocity impact cases suggests that shape effects may be less important at meteoroid velocities than at the lower velocities which are obtainable in the laboratory. At meteoroid velocities, the shocked state enthalpies of both projectile and bumper are much greater than the material vaporization energies; thus the generation of particles by incomplete vaporization of the projectile is not very likely. Particles originating from diffraction of the bumper shock will undoubtedly still be present in the cloud. However, results in the laboratory velocity range have shown that cloud particle sizes decrease with velocity. The fine "particles" produced when the shocked state enthalpy falls just below that required for vaporization appear to behave in a manner similar to the "true gas cloud", but with substantially lower expansion rates. These observations agree qualitatively with the observation by Murphy, based on his strip model theory, that shape effects should not be a dominant factor at meteoroid velocities, provided that the vehicle skin is separated from the bumper by several projectiles (or meteoroid) diameters.

## 4.0 THEORY

The theoretical studies carried out during the contract period have been reported in detail in References 5 and 8. This report contains a brief summary of these studies. In addition, some theoretical results are presented in Sections 3.2, 3.3 and 3.4 for comparison with experimental impact data.

The approximate strip model and the potentially more accurate finite difference model, the two theoretical approaches developed previously, have both been improved during the past year. The mathematical basis of the strip model has remained unaltered, however, the presence of bow waves and a variable $\gamma$ have been incorporated. A graphical print-out has also been incorporated into the program. The one-dimensional portion of the finite difference model was developed further during the course of this contract. The mathematical difficulties with the long term stability and the "jitters", associated with Von Neuman's artificial viscosity, have been overcome.

The theoretical effort has been largely devoted to a more accurate determination of the initial shocked conditions and expansion state relationships, including escape velocities. This work is applicable to both models and is presented in Section 4.1. The present state of the finite difference model is presented in Section 4.2, and that of the strip model in Section 4.3.

## 4.1 IMPACT SHOCKED AND EXPANDED STATES

### MODEL RESTRICTIONS

The theoretical models developed are only applicable to a hypervelocity impact under the following conditions:

1) The impact occurs in a vacuum.

2) The pellet velocity is great enough to generate sufficient energy to vaporize the impacting pellet material and that portion of the target material punched out by the pellet.

3) The pellet is cylindrical, and impacts on the target at a plane normal to the axis of the pellet and its velocity vector.

4) The pellet diameter is of the same order as its length, and the target thickness is less than 1/10 the pellet diameter.

In addition to the above initial restrictions placed on the model, it should be noted that for meteoroid protection systems, the emphasis is placed on the downstream expansion cloud characteristics some 5 to 50 pellet diameters downstream of the target.

A description of the impact and expansion processes will not be repeated here (Ref. 8), however, the implications of the restrictions are discussed as they provide the foundation for the theoretical determination of the shocked and expanded states.

A meteoroid impact in space occurs in a vacuum. This simplifies the boundary conditions, as the escape front velocities will remain constant once they have been initially determined. The initial determination of the escape velocities is thus extremely important in the prediction of the downstream expansion cloud characteristics. Experimental impacts are carried out at $10^{-1}$ to $10^{-2}$ torr. At these pressures the mean free path of the molecules is such that they have negligible effect on the expansion front, and indeed

constant velocity escape fronts are observed.

At meteoroid velocities, 65,000 ft/sec (20 km/sec), sufficient kinetic energy is available to vaporize most materials. At experimental impact velocities, 26,000 - 32,000 ft/sec (8-10 km/sec), the initial kinetic energy is sufficient to vaporize only a few materials with low vaporization energies (Section 3.2). If only the initial portions of the impacted materials are vaporized, little difference will be observed in the experimental photographs of the downstream expansion cloud. However, differences will show up in the experimental pressure traces. At meteoroid velocities vaporization energy is a small portion of the total energy and may be neglected without introducing appreciable error. For experimental impacts the vaporization energy is important and must be considered.

The cylindrical geometry of the pellet, and axi-symmetrical expansion assumed for the models, were obtained for the experimental impacts analysed. We cannot, of course, expect these assumptions to be valid in the case of a meteoroid impact. The model's geometrical restrictions do not limit its general application in analysing a meteoroid protection system. Oblique impacts should be less hazardous than normal impacts and therefore a design based on normal impact is conservative for a meteoroid protection system. The pellet geometry will not affect the downstream expansion flow appreciably at distances beyond five pellet diameters downstream. The geometry will influence the amount of upstream flow. At experimental impact velocities, where upstream expansion flow is important, a spherical pellet impact will result in more upstream expansion flow than a cylindrical normal impact. In either case the large amount of upstream flow experimentally observed cannot

be predicted by the strip model.

A thin target impact model allows assumptions to be made which greatly simplify the mathematics of the model. First, a one-dimensional analysis may be used during the time the pellet is being shocked. This will introduce very little error in predicting the downstream expansion cloud at later times. Secondly, curvature of the pellet shock and diffraction of the target shock may be neglected. (Reference 8).

The implications of the above restrictions, along with the usual homogeneous, inviscid fluid assumption for hydrodynamic impact models (Reference 9), provide the foundation for the thin target impact model. It now remains to determine the shocked pressure (p), density ( $\rho$ ), internal energy (e) and velocity (u), and their relationship during the expansion process. Most of the recent theoretical effort has been devoted to this problem.

Energy Conversions

The shock conditions may be determined directly from the conservation equations, experimental Hugoniot data for the density ratio $\rho_s/\rho_o$ , and a one-dimensional shock decay analysis. The method is discussed in detail in Reference 8. A summary of the method is presented here.

Figure 4.1 shows schematically the energy conversions which would occur for a small element, located symmetrically about the impact interface, during the impact shock and expansion processes. Initially before impact, the pellet half of the element would have a total energy equal to $\frac{1}{2}V^2$, and the target half zero energy. The enthalpy of the unshocked pellet and target material were neglected. A like material impact was assumed to simplify the analysis. Unlike material impacts are discussed in Reference 8.

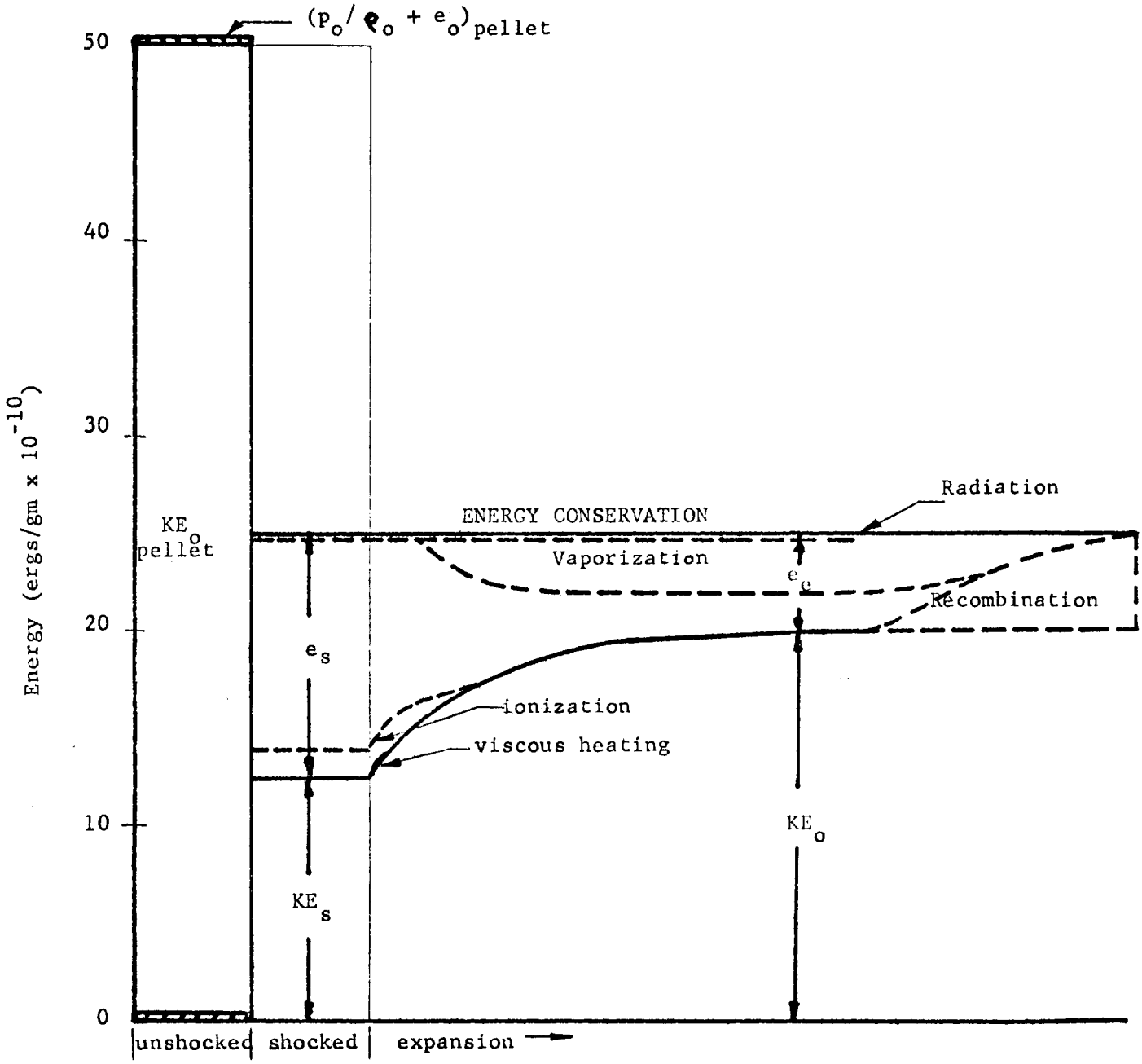


Fig.4.1 Schematic of energy conservation for element of target and equal initial mass of pellet. Values are approximately those for Mg/Mg impact at 10 km/sec

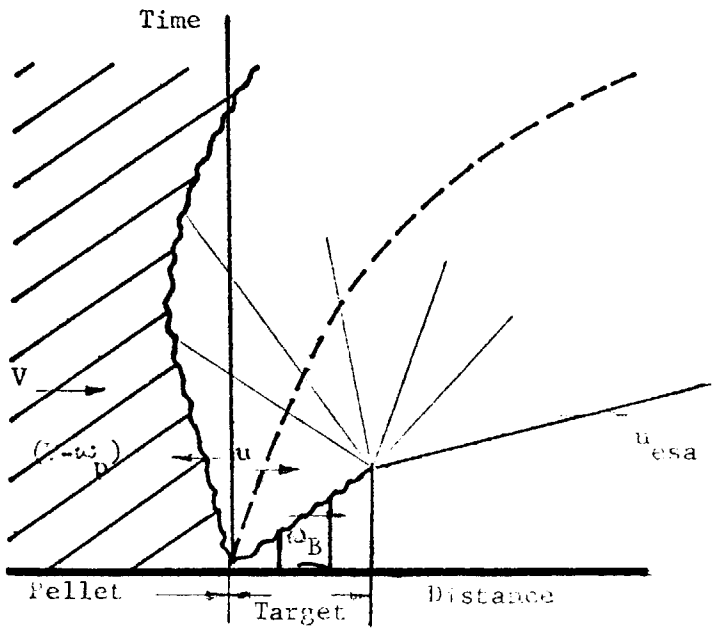


Stationary Target System

FIG. 4.2 Distance-Time Shock and Expansion Wave Diagram

On impact the shocks generated (Figure 4.2) must compress and accelerate the target material portion of the element, and compress and decelerate the pellet material. For a like material impact an equal mass of target and pellet material will initially be shocked, i.e. at any time before the target shock passes through the target. Therefore for any like material impact, the conservation of momentum implies that

$$u_s = \frac{V}{2} \tag{4.1}$$

for the initial impact conditions. Equation 4.1 will not apply for pellet material shocked after the axial rarefaction wave reaches the pellet shock (Fig. 4.2).

The initial shocked pressure ( $\rho_s$ ), density ( $\rho_s$ ), mechanical energy ( $p_s / \rho_s$ ), and internal energy ( $e_s$ ) must be obtained by applying the conservation equations across a stationary shock system as shown below.

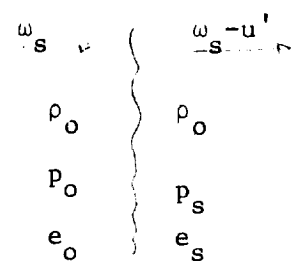


Stationary Shock System

It is clear that for such a flow system the total enthalpy must be conserved and:

mass $$\rho_o \omega_s = \rho_s(\omega_s - u') \tag{4.2}$$

momentum $$p_o + \rho_o \omega_s^2 = p_s + \rho_s(\omega_s - u')^2 \tag{4.3}$$

energy $$e_o + p_o/\rho_o + \frac{1}{2}\omega_s^2 = e_s + \frac{p_s}{\rho_s} + \frac{1}{2}(\omega_s - u')^2 \tag{4.4}$$

Equations 4.2 to 4.4 may be combined and rearranged to give:

$$\rho_s/\rho_o = \frac{\omega_s}{\omega_s - u'} \tag{4.5}$$

$$p_s - p_o = \rho_s \omega_s u' \tag{4.6}$$

$$e_s - e_o = \frac{1}{2}(p_s + p_o)\left(\frac{1}{\rho_o} - \frac{1}{\rho_s}\right) \tag{4.7}$$

From the two-shock system in Fig. 4.2 and equation 4.1 it can be seen that if $\omega_s = \omega_p = \omega_T$ then

$$u' = \frac{V}{2} \tag{4.8}$$

Equation 4.8 may be substituted into 4.5 to 4.7 to obtain:

$$\rho_s/\rho_o = \frac{\omega_s}{\omega_s - \frac{V}{2}} \tag{4.9}$$

$$p_s - p_o = \rho_o \omega_s \frac{V}{2} \tag{4.10}$$

and neglecting $p_o$ (i.e. $p_o/p_s \ll 1$)

$$e_s - e_o = V^2/8 \tag{4.11}$$

$$p_s/\rho_s = (\omega_s - \frac{V}{2})\frac{V}{2} \tag{4.12}$$

Further simplification can be obtained if it is assumed that $\omega_s = V$,

and equations 4.9 to 4.12 become, for $\omega_s = V$

$$\left.\begin{aligned} \rho_s/\rho_o &= 2 \\ p_s - p_o &= \frac{1}{2}\rho_o V^2 \\ e_s - e_o &= \frac{V^2}{8} \\ p_s/\rho_s &= \frac{V^2}{4} \end{aligned}\right\} \qquad (4.13)$$

Experimental shock Hugoniots (Reference 10) and impact photographs (Fig. 3.3) show that usually $\omega_s > V$ and equation 4.13 becomes for $\omega_s > V$

$$\left.\begin{aligned} \frac{\rho_s}{\rho_o} &< 2 \\ p_s - p_o &> \frac{1}{2}\rho_o V^2 \\ e_s - e_o &= V^2/8 \\ p_s/\rho_s &> \frac{V^2}{4} \end{aligned}\right\} \qquad (4.14)$$

The initial energy conversions illustrated in Fig. 4.1 may be expressed as a function of the initial kinetic energy $KE_o = \frac{V^2}{2}$ from equations 4.1 and 4.14 and;

$$KE_s = \frac{1}{4} KE_o \qquad (4.15)$$

neglecting $e_o$ i.e. $e_o/e_s << 1$

Then $$e_s = \tfrac{1}{4} KE_o \tag{4.16}$$

and $$p_s/\rho_s > \tfrac{1}{2} KE_o \tag{4.17}$$

The total energy to be conserved within the shocked element considered in Fig. 4.1 is

$$E_{TOT} = e_s + KE_s = \tfrac{1}{2} KE_o \tag{4.18}$$

Only the mechanical energy ( $p_s / \rho_s$ ) will be affected by the shock velocity or experimental Hugoniot curve. The initial shocked internal and kinetic energies will depend only on the initial kinetic energy of the pellet.

Considering the element chosen (Fig. 4.1), once it becomes free to expand it will cool, and the internal energy will decrease as it is reconverted into kinetic energy. Eventually the total energy of the element will be in the form of kinetic energy and equal to one-half the original kinetic energy of the element. The driving force for the expansion is the pressure, or flow work energy ( $p_s / \rho_s$ ), which will approach zero as the element expands into a vacuum.

The above analysis will be true only for the initial shocked elements. Elements which are shocked after the pellet shock starts to decay will have a higher total energy ( $e_s + KE_s$) and lower mechanical energy ( $p_s / \rho_s$ ). Eventually, if the shock strength is reduced down to an elastic wave, an

element will pass downstream with its total energy unaltered (i.e. equal to $KE_o$). It will thus have twice the energy of an initial element (Section 3.3) and no mechanical energy ( $p_s$ / $\rho_s$ ) will be generated.

In addition to the three energy forms mentioned so far, energy may also be converted into vaporization and ionization forms, as shown schematically in Fig. 4.1. Energy lost from a control volume due to radiation is thought to be negligible. Certainly at experimental impact velocities this is true (Reference 3). Some kinetic energy will be converted into internal energy in regions of the expansion where shear stresses are high. Such conversions due to viscous heating have been neglected because of their complex nature and the small effect they would have on the overall expansion cloud. Vaporization and ionization energies are the two additional energy forms then that could affect the downstream expansion flow.

Vaporization energies were obtained for various materials from experimental results at atmospheric conditions. These vaporization energies are of the same order of magnitude as the shocked internal energies generated on impact at experimental velocities, 23,000 ft/sec to 30,000 ft/sec (7 to 9 km/sec). At meteoroid impact velocities, 65,600 ft/sec (20 km/sec), the vaporization energies are small compared to the impact-generated internal energies and may be neglected (Reference 8).

There is uncertainty in determining when and how vaporization will occur in an element which is shocked by an impact. The conditions of high pressure and internal energy initially occurring behind the shocks will be such that the phase of the material will be indistinguishable, i.e. conditions will be

above the critical point. It is only after the element expands and cools that a distinguishable phase will occur and energy in the form of vaporization can then be evaluated. Exactly at what time this will occur during the expansion process is difficult to determine from the phase diagrams. Certainly it will not occur suddenly but gradually as the element continues to expand. Exactly how the energy will go into vaporization is dependent on the process, i.e. constant pressure, temperature or entropy.

In an attempt to allow for vaporization energies at experimental velocities, the vaporization energy was subtracted from the total shocked energy immediately after impact. However, when this was done in the strip model, it was found that the downstream escape velocities observed experimentally could not be obtained theoretically. It was initially hoped that by reducing the total energy in such a manner, the experimental escape velocities could be obtained by reducing $\gamma$ to a more realistic value around 1.4. It was found that even at $\gamma$ equal to 1.2 the experimental escape velocities could not be obtained. This method was then abandoned. After further consideration it was felt that the vaporization energy would not affect the escape front velocities appreciably in the hypervelocity impact regime, and so could be neglected.

Ionization occurs at experimental impact velocities and it is reasonable to assume that ionization energies would become significant at meteoroid impact velocities and would affect the expansion escape velocities. Ionization energies were neglected in the strip model. It was felt that little error would be introduced in predicting experimental impacts as the ionization level would be low. However, for meteoroid velocity impacts the degree of

ionization could be the dominant energy form.

If ionization is neglected in this case, then predicted escape velocities, and secondary surface loadings, will be too high. On the other hand, if the cloud expands out radially at a faster rate, the pressure will be reduced more quickly and the loading pressure will be less severe.

Equation of State

The previous section has been devoted mainly to energy conversions and the determination of the shocked conditions. The energy conversions are further complicated by state relationships between e, p and $\rho$ . For example, if the internal energy is reduced by vaporization and ionization, how will the pressure and density adjust to such a change?

Considering the initial shocked conditions, it is clear from equations 4.9 to 4.11 that $p_s, \rho_s$ , and $e_s$ may be determined without a state relationship, provided the initial unshocked conditions ($\rho_o$ , $p_o$ , $e_o$ , V) of the material are known along with the shock velocity $\omega_s$ . Usually it is more convenient to obtain a shock density ratio $\rho_s / \rho_o$ from experimental Hugoniot curves and then to calculate $\gamma$ from equation 4.9.

Initially the strip model was set up utilizing an ideal equation of state with an artificial $\gamma_s$ obtained to satisfy the appropriate density ratio ( $\rho_s$ / $\rho_o$ ). Essentially a theoretical Hugoniot curve was obtained from equation 4.7 by assuming;

$$\left.\begin{aligned} p/\rho &= RT \\ \delta e &= c_v \delta T \\ \gamma &= c_p/c_v \end{aligned}\right\} \qquad (4.19)$$

to eliminate $e_s - e_o$ from equation 4.7. The standard Hugoniot curve thus obtained was further reduced, with very little error (Reference 8) by assuming $p_o / p_s << 1$, and the strong shock approximation obtained.

$$\frac{\rho_s}{\rho_o} = \frac{\gamma_s + 1}{\gamma_s - 1} \tag{4.20}$$

From equation 4.20 it is obvious how $\gamma_s$ could be artificially fixed to satisfy the density ratio obtained from experimental Hugoniot points. Then from equations 4.9 and 4.20

$$\omega_s = \frac{\gamma_s + 1}{4} V \tag{4.21}$$

and substituting 4.21 into 4.10.

$$p_s - p_o = \frac{\gamma_s + 1}{8} \rho_o V^2 \tag{4.22}$$

Equation 4.11 will remain unchanged

$$e_s - e_o = \frac{V^2}{8} \tag{4.11}$$

Very small differences were found (Ref. 9) between experimental results and theoretical values of $\rho_s$, $\omega_s$ and $p_s$ obtained from equations 4.20 to 4.22, provided $\gamma_s$ was fixed from equation 4.20 so that $\rho_s / \rho_o$ agreed with the experimental results. No check was available for the theoretical calculation of internal energy $e_s$ except through the sound velocity.

A theoretical sound velocity may be obtained by assuming in the shocked state that

$$p_s / \rho_s^{\gamma} = \text{constant} \tag{4.23}$$

$$\text{and} \qquad a_s^2 = \left(\frac{\partial p_s}{\partial \rho_s}\right)_{\text{entropy}} \tag{4.24}$$

Then performing the differentiation

$$a_s^2 = \frac{\gamma p_s}{\rho_s} \tag{4.25}$$

and substituting for $p_s$ and $\rho_s$ from equations 4.20 and 4.22.

$$a_s = \sqrt{\frac{\gamma(\gamma_s - 1)}{2}}\ \frac{V}{2} \tag{4.26}$$

The theoretical sound velocity calculated from equation 4.26 with $\gamma = \gamma_s$ gives a value 10% higher than observed experimentally (i.e. 35,400 ft/sec (10.78 km/sec) cf. 32,500 ft/sec (9.90 km/sec)). The value of $\gamma$ in equation 4.23 does not necessarily bear any relation to the value of $\gamma_s$, which was obtained solely to satisfy the conversion of mass across the shock. However, it is expected that $\gamma$ will have a high value for a material in a highly condensed shock state, i.e. a small increase in volume would result in a very large decrease in pressure.

A theoretical value for $\gamma$ may be obtained at experimental velocities from measured downstream escape velocities ( $u_{es}$ ). Using a method of characteristics, the escape velocity for unsteady flow into a vacuum may be expressed as a function of the conditions of the material before pressure release occurs.

$$u_{es} = u_s \pm \frac{2}{\gamma - 1} a_s \tag{4.27}$$

For the axial downstream escape front ( $u_{es,a}$ ); $u_s = \frac{V}{2}$ ; for like material impacts, the positive sign is correct, and $a_s$ may be expressed

from equation 4.26 to give

$$\frac{u_{es}}{V} = \frac{1}{2} + \sqrt{\frac{\gamma(\gamma_s-1)}{2(\gamma-1)^2}} \tag{4.28}$$

A plot of $\frac{u_{es,a}}{V}$ vs $\gamma$ for different values of $\gamma_s$ is shown in Fig. 4.3.

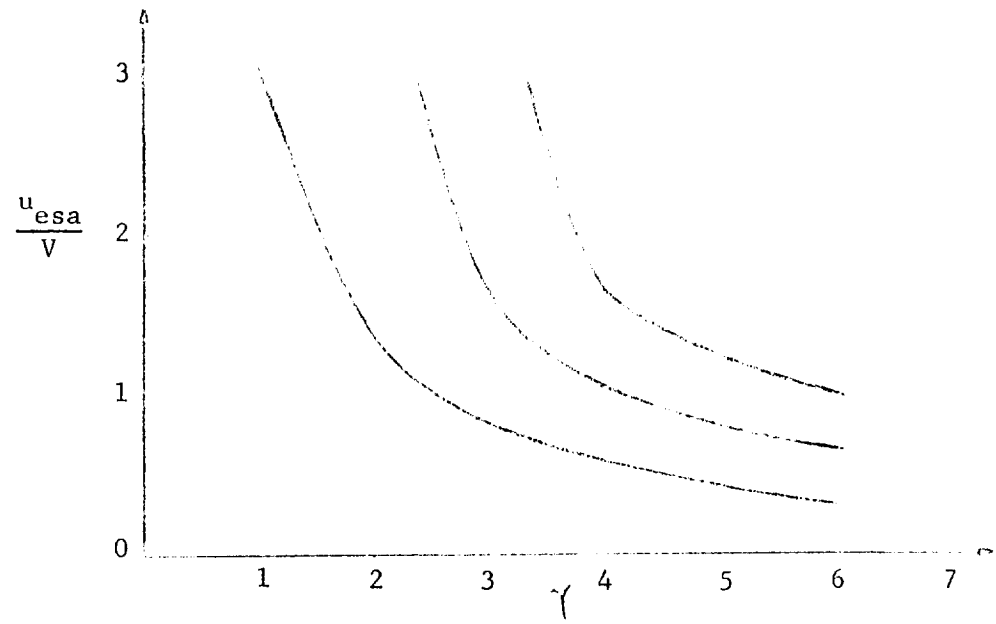


Figure 4.3 Escape Velocity as a Function of V, $\gamma_s$, $\gamma$

It was found experimentally that for like material impacts up to 29,500 ft/sec (9 km/sec) that $u_{es,a}/V = 1.5$ (Reference 1). For the experimental Al on Al impact, discussed in reference 8, $\gamma_s = 4.7$ was required to satisfy the density ratio $\rho_s/\rho_o$. Thus from Fig. 4.4 with $\gamma_s = 4.7$ and $\frac{u_{es,a}}{V} = 1.5$, $\gamma$ is found to equal 3.5. Then substituting values for $\gamma_s$, $\gamma$, and V into equation 4.26, $a_s$ = 32,100 ft/sec (9.8 km/sec). The strip model allows for two different $\gamma$'s; $\gamma_s$ to satisfy experimental

Hugoniot data, and $\gamma$ to satisfy experimental escape front velocities.

At meteoroid velocities $\gamma$ was assumed to be equal to $\gamma_s$, and the value of $\gamma_s$ was obtained from extrapolated experimental Hugoniot curves. The validity of assuming $\gamma = \gamma_s$ cannot be justified. In fact, if the escape front velocity remains the same ($u_{es,a}/V \simeq 1.5$), then $\gamma$ would be somewhat less than $\gamma_s$, even at the lower values of $\gamma_s$ expected ($\gamma_s \simeq 3$). Thus, predicted meteoroid impact escape velocities would be too low, i.e. from equation 8.28 if $\gamma$ is larger, then $u_{es,a}$ will be lower. However, more accurate predictions of $\gamma$ for meteoroid impacts are not warranted until a more accurate determination of the sound velocity, or internal energy is obtained. As mentioned previously, a statistical approach seems to be a good one to predict the shocked internal energy allowing for ionization effects.

A variable $\gamma$ was introduced in an attempt to predict theoretically the large upstream escape velocities observed experimentally. As each strip element was shocked, a $\gamma_s$ was computed from the density ratio ($\rho_s/\rho_o$). As the pellet shock decayed, $\rho_s/\rho_o$ decreased, and $\gamma_s$ increased (equation 4.20). This increase in $\gamma_s$, predicted lower upstream escape velocities than those with a constant $\gamma_s$. The variation in $\gamma_s$ was noted to be small, and because of its adverse effect on the upstream expansion cloud, this method was abandoned in favor of the constant $\gamma_s$.

In summing up this section it may be stated that:

1. An ideal equation of state with an appropriate choice of $\gamma_s$ and $\gamma$, obtained from experimental Hugoniots and escape front velocities,

can be used to predict adequately experimental impacts and the resulting downstream expansion clouds.

2. At meteoroid velocities, impacts and expansions are predicted (Section 4.3) by assuming an ideal equation of state with $\gamma_s = \gamma$. The value of $\gamma_s$ was obtained from extrapolated Hugoniot data. "Puff ball", or aerated material impacts are difficult to analyse due to the non-monotonic nature of the Hugoniot curves (Reference 11).

3. It is suggested for predicting meteoroid impacts with more confidence that more accurate state relationships be obtained which allow for ionization and impacts of aerated materials. A statistical approach to the solution seems fruitful at this time.

## 4.2 THE FINITE DIFFERENCE MODEL

### 4.2.1 Introduction

It is the purpose of this chapter to study a one-dimensional hydrodynamic model of the meteoroid-bumper interaction. In this section we will indicate the basic assumptions of the model and outline the qualitative analysis of the flow. The governing equations will be presented in Section 4.2.2 and some results will be discussed in Section 4.2.3. For brevity the derivations and proofs are omitted and reference may be made to the author's topical report NASA CR-54725 (Ref. 5).

The approach taken to the problem is that initiated by Dr. G. V. Bull (Ref. 4). A hydrodynamic model is proposed and the kinetic energy assumed sufficiently high that vaporization energy may be ignored. At typical meteoroid velocities, 65,600 to 229,000 ft/sec (20-70 km/sec), these assumptions should be valid. However, plasma effects due to the stripping

of outer orbital electrons may then become important. Such effects are not considered in this report.

The model is one-dimensional in that radial effects are ignored. Such an assumption can only be valid for short times after impact. If we interpret the study made here as applying to the centerline for impact by a cylindrical pellet, then by a short time we mean a time necessary for radial attenuation waves to penetrate to the center. Hence, if the length of the pellet is small compared to the radius, we will expect the one-dimensional model to be valid during the period in which the pellet is being vaporized. It is useful to visualize the one-dimensional model as describing the impact of one plate onto another. Here the radial effects are removed to infinity and the motion is truly one-dimensional.

While the assumption that the energy of vaporization is negligible is appropriate for impacts at typical meteoroid velocities, the simplified model is difficult to confirm experimentally. The upper limit to the experimental velocity range is roughly 32,800 ft/sec (10 km/sec). Consequently, it does not seem reasonable to ignore the binding energy in comparison with the kinetic energy corresponding to such a velocity. The ideal gas equation of state is used for simplicity. We use the polytropic gas exponent $\gamma$ as a free parameter which may be determined experimentally.

We consider the normal impact of a moving plate (the pellet) onto one at rest in the laboratory (the bumper). At the moment of impact strong shock waves are produced which propagate through the pellet and bumper decelerating the former and accelerating the latter. In the shocked regions high thermodynamic energies will be produced at the expense of the pellet

kinetic energy. As noted above it is assumed that the kinetic energy involved is sufficiently high that the resulting thermodynamic energy will be large compared with the intermolecular binding force of the pellet and bumper materials. The hydrodynamic equations are presumed to apply throughout the pellet and bumper materials. Consider Fig. 4.4.

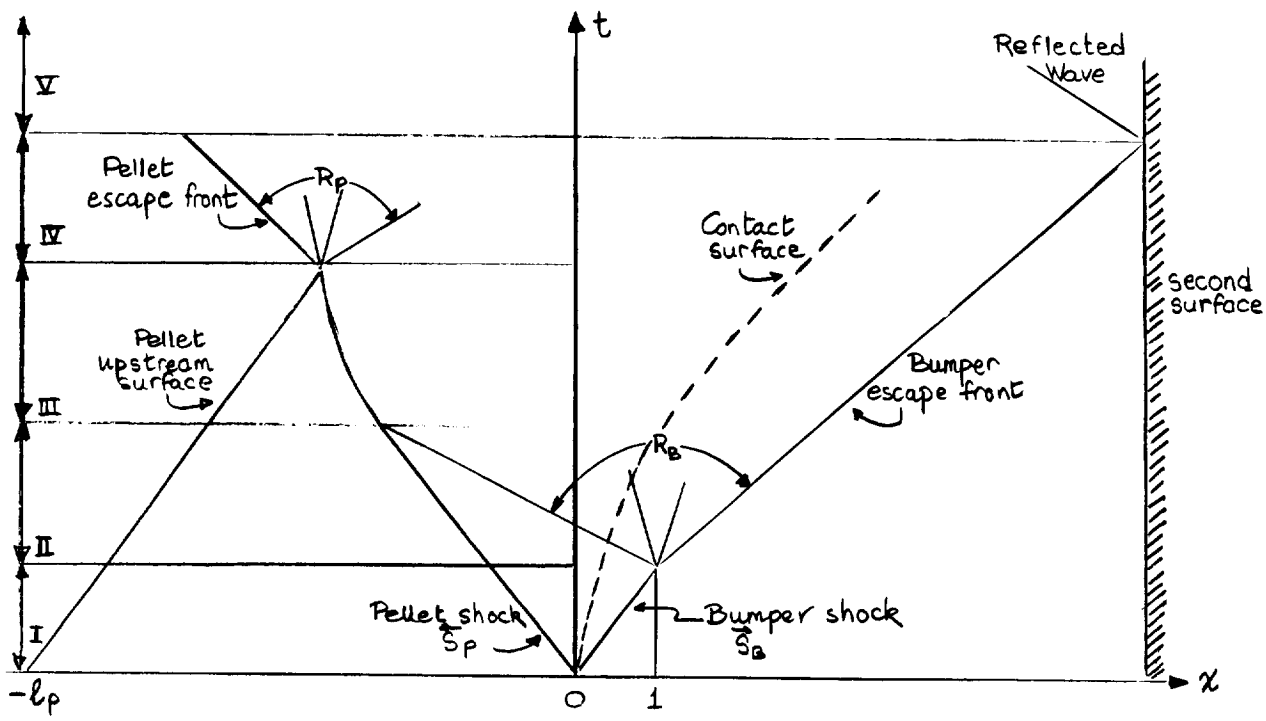


Figure 4.4 Wave Diagram of Impact Process

We may divide the flow into five characteristically different periods, I-V. In period I, both shocks are progressing with undiminished strength. The profiles may be determined in terms of the polytropic exponent $\gamma$ from the Rankine-Hugoniot relations across $\overrightarrow{S}_B$ and $\overleftarrow{S}_p$, the continuity of pressure and particle velocity across the contact front C and the assumption of a

limiting density ratio.

In period II, $\vec{S}_B$ has reached the downstream free surface of the bumper and generated a rarefaction $R_B$. As $R_B$ does not overtake $\overleftarrow{S}_p$ during this period, the flow is isentropic in each zone of shocked or unshocked fluid. The isentropic equations govern the flow and in many cases, especially for like material impacts, a simple analytic solution is available.

Period III denotes the interaction between $R_B$ and $\overleftarrow{S}_p$. Evidently period III will only occur if $R_B$ overtakes $\overleftarrow{S}_p$ before the latter reaches the upstream free surface of the pellet. Since the resulting shock decay is of primary interest, it will always be assumed that period III does occur. The governing equations are, of course, non-isentropic. In period IV the pellet shock has generated the rarefaction $R_p$. The entire system is considered to have vaporized and to be in state of expansion. In this period the one-dimensional assumption loses validity. However, to test the stability of the finite difference code and to make a preliminary study of the interaction of the gas cloud with a secondary surface the analysis was continued. The governing equations were isentropic or non-isentropic depending on whether or not period III occurred.

Period V indicates the interaction of the gas cloud with a secondary surface. We expect the governing equations to be non-isentropic as the reflected shock wave will propagate into a non-uniform region.

In general we have resorted to finite difference techniques for solving the governing equations. Consequently a considerable effort has been directed towards the establishment of a successful finite difference code.

Difference equations of the "open" kind in which discontinuities are handled automatically were employed. We used the artificial dissipation term of Richtmyer and Von Neumann. In addition to establishing a stable code we succeeded in largely eliminating "jitters" associated with inefficient dissipation. These jitters are familiar to users of artificial dissipation terms. We used a technique of "smoothing" (Ref. 12) familiar to meteorologists but which does not appear to have been applied to this type of problem. Judiciously applied, a smoother not only eliminates unmeaningful local disturbances but also enhances the stability of the program.

### 4.2.2 Governing Equations

(i) Period I

The following non-dimensionalization is performed:

$$\begin{aligned} \rho &\longrightarrow \rho/\rho_{Bo} \\ p &\longrightarrow p/\rho_{Bo}V^2 \\ u &\longrightarrow u/V \end{aligned} \qquad 4.2.1$$

where $\rho$, p, u are the density, pressure, and particle velocity respectively. V is the impact velocity of the pellet in the reference frame of the bumper. The subscripts B and P will be used to distinguish bumper from pellet properties. The further subscript o will indicate unshocked states. The unit of length is taken to be the bumper thickness. Consequently

$$\text{time} \longrightarrow \text{time} \times \frac{\text{impact velocity of pellet}}{\text{bumper thickness}} \qquad 4.2.2$$

We fix our coordinate system by choosing the origin of the x-axis at the contact front at the instant of impact ( t = 0 ). The length of the pellet in non-

dimensional units is taken to be $\ell_p$ .

At the end of Period I when $\bar{S}_B$ reaches the downstream bumper free surface, one finds the following (Ref. 5):

$$t = t_o = \frac{2}{\gamma_B+1}\left\{1 + \sqrt{\frac{\gamma_B+1}{\gamma_p+1}\,\frac{\rho_{Bo}}{\rho_{po}}}\right\} \qquad 4.2.3$$

The contact front is located at:

$$x_c = \frac{2}{\gamma_B+1} \qquad 4.2.4$$

The pellet shock is at:

$$x_{sp} = \frac{\gamma_p+1}{\gamma_B+1} - \frac{\gamma_p-1}{\gamma_B+1}\left\{1 + \sqrt{\frac{\gamma_B+1}{\gamma_p+1}\,\frac{\rho_{Bo}}{\rho_{po}}}\right\} \qquad 4.2.5$$

The shocked fluid profiles are given by:

$$u(x,t_o) = \frac{1}{1 + \sqrt{\frac{\gamma_B+1}{\gamma_p+1}\,\frac{\rho_{Bo}}{\rho_{po}}}} \qquad x_{sp} \le x \le 1 \qquad 4.2.6$$

$$p\,(x,t_o) = \frac{\gamma_B+1}{2}\,\frac{1}{\left\{1 + \sqrt{\frac{\gamma_B+1}{\gamma_p+1}\,\frac{\rho_{Bo}}{\rho_{po}}}\right\}^2} \qquad x_{sp} \le x \le 1 \qquad 4.2.7$$

$$\rho(x,t_o) = \frac{\gamma_p+1}{\gamma_p-1}\left(\frac{\rho_{po}}{\rho_{Bo}}\right) \qquad x_{sp} \le x \le x_c \qquad 4.2.8$$

$$\rho(x,t_o) = \frac{\gamma_B+1}{\gamma_B-1} \qquad x_c \le x \le 1 \qquad 4.2.9$$

The upstream pellet free surface is located at:

$$x_p = -\ell_p + \frac{2}{\gamma_B+1}\left\{1 + \sqrt{\frac{\gamma_B+1}{\gamma_p+1}\,\frac{\rho_{Bo}}{\rho_{po}}}\right\} \qquad 4.2.10$$

The unshocked fluid profiles are given by:

$$u(x,t_o) = 1 \qquad x_p \leq x < x_{sp} \qquad 4.2.11$$

$$p(x,t_o) = o \qquad x_p \leq x < x_{sp} \qquad 4.2.12$$

$$\rho(x,t_o) = \frac{\rho_{po}}{\rho_{Bo}} \qquad x_p \leq x < x_{sp} \qquad 4.2.13$$

All quantities in equations (4.2.3) to (4.2.13) are in the non-dimensional form of (4.2.1) and (4.2.2).

(ii) Period II

The governing equations are the isentropic equations.

$$\frac{2}{\gamma-1}\frac{\partial c}{\partial t} + c\frac{\partial u}{\partial x} + \frac{2u}{\gamma-1}\frac{\partial c}{\partial x} = o \qquad 4.2.14$$

$$\frac{\partial u}{\partial t} + u\frac{\partial u}{\partial x} + \frac{2c}{\gamma-1}\frac{\partial c}{\partial x} = o \qquad 4.2.15$$

The rarefaction $R_B$ is characterised by two surfaces, the expansion and the escape fronts, moving back into the shocked gas and out into the vacuum respectively. As long as the expansion front moves into a uniform region, the solution for $R_B$ is a simple wave. Let $x_o$ (= 1) signify the initial position of the downstream surface of the bumper and to be the time at which $R_B$ is generated (given by (4.2.3)). At a later time t, the positions of the expansion and escape fronts are given by $x_{exp}$ and $x_{esc}$ where

$$x_{exp} = x_o + (u_o - c_o)\ (t - t_o) \qquad 4.2.16$$

and

$$x_{esc} = x_o + \left[ \frac{2}{\gamma-1} c_o + u_o \right] (t - t_o) \qquad 4.2.17$$

Here $u_o$ and $c_o$ are the constant values of the particle and sound velocities at the expansion front. The distributions of c and u in the rarefaction zone are given by:

$$c(x,t) = \frac{\gamma-1}{\gamma+1} \left[ u_o - \frac{(x - x_o)}{(t - t_o)} \right] + \frac{2c_o}{\gamma+1} \qquad 4.2.18$$

$$u(x,t) = \frac{2}{\gamma+1} \left[ \frac{x - x_o}{t - t_o} + c_o \right] + \frac{\gamma-1}{\gamma+1} u_o \qquad 4.2.19$$

valid for $t \geq t_o$ and $x_{exp} \leq x \leq x_{esc}$.

The solution (4.2.16) to (4.2.19) will be valid until the expansion front interacts with the contact surface or, in the case of a like material impact, until it interacts with the pellet shock $S_p$. It is useful then to have a finite difference representation of the isentropic equations.

With a space-time grid for which the respective grid point intervals are $\Delta x$ and $\Delta t$ we write:

$$u_j^n = u(j\Delta x, n\Delta t)$$
$$c_j^n = c(j\Delta x, n\Delta t) \qquad 4.2.20$$

Substituting the appropriate differences into (4.2.14), (4.2.15) leads one to the finite difference scheme:

$$c_j^{n+1} = \frac{1}{2} \left[ c_{j+1}^n + c_{j-1}^n \right] - \frac{\gamma-1}{2} \frac{\Delta t}{\Delta x} \left[ c_j^n \frac{u_{j+1}^n - u_{j-1}^n}{2} + \frac{2u_j^n}{\gamma-1} \frac{c_{j+1}^n - c_{j-1}^n}{2} \right] \qquad 4.2.21$$

$$u_j^{n+1} = \frac{1}{2}\left[u_{j+1}^n + u_{j-1}^n\right] - \frac{\Delta t}{\Delta x}\left[u_j^n \frac{u_{j+1}^n - u_{j-1}^n}{2} + \frac{2c_j^n}{\gamma-1}\frac{c_{j+1}^n - c_{j-1}^n}{2}\right]$$

4.2.22

With full knowledge of u, c at time n $\Delta t$, one may use equations (4.2.21), (4.2.22) to determine u, c at the later time (n + 1) $\Delta t$. The treatment at the boundaries is discussed in Ref. 5. The stability condition for (4.2.21), (4.2.22) which must be satisfied if the computed profiles are to be in approximate agreement with the exact solution of equations (4.2.14), (4.2.15), is given by:

$$\frac{\Delta t}{\Delta x}(u \pm c) < 1$$

4.2.23

One may use the simple wave solution (4.2.16 to (4.2.19) to eliminate the initial discontinuity at the bumper free surface and complete the solution in Period II by means of (4.2.21), (4.2.22). A special technique is required at the contact surface. Using the isentropicity of particles on either side of the contact surface, one may write the following relationship between the values of c on either side:

$$c_p = Ac_B^B$$

4.2.24

where $A = \left[\frac{\rho_{Bo}}{\rho_{po}}\frac{\gamma_p}{\gamma_B}(\lambda\gamma_B)^{\frac{\gamma_p - \gamma_B}{\gamma_p(1-\gamma_B)}}\right]^{1/2}$

$$B = \frac{\gamma_B(\gamma_p - 1)}{\gamma_p(\gamma_B - 1)}$$

$\lambda = p/\rho_B^{\gamma_t}$ (evaluated at the contact surface)

Equation (4.2.24) is only valid for a perfect gas. Using (4.2.24) one may represent $\partial c/\partial x$ at the points adjacent to the contact surface. If the grid point labelled (j-1) is to the left of the contact surface (i.e. in the pellet region) and that labelled (j+1) is to the right, one may form the centered difference at j:

$$\frac{\partial c}{\partial x}\Big|_{j\Delta x} \cong \frac{A[c^n_{j+1}]^B - c^n_{j-1}}{2\Delta x} \qquad 4.2.25$$

and similarly for grid points lying in the bumper region. We chose the convention that when the contact front coincided with a grid point, that grid point assumed pellet properties.

(iii) Period III

The governing equations are the equations for conservation of mass, momentum, and energy, together with the equation of state.

$$\frac{\partial \rho}{\partial t} + \nabla\cdot(\rho \underline{u}) = o \qquad 4.2.26$$

$$\frac{\partial \underline{u}}{\partial t} + (\underline{u}\cdot\nabla)\underline{u} + \frac{1}{\rho}\nabla p = o \qquad 4.2.27$$

$$\frac{\partial \varepsilon}{\partial t} + (\underline{u}\cdot\nabla)\varepsilon + \frac{p}{\rho}\nabla\cdot\underline{u} = o \qquad 4.2.28$$

$$\varepsilon = \frac{p}{(\gamma-1)\rho} \qquad 4.2.29$$

A finite difference of (4.2.26 to (4.2.29) is given by (Ref. 5).

$$\frac{\rho^{n+1}_j - \rho^n_j}{\Delta t} + u^{n+1}_j \frac{\rho^n_j - \rho^n_{j-1}}{\Delta x} = -\rho^n_j \frac{u^{n+1}_{j+1} - u^{n+1}_{j-1}}{2\Delta x}, \quad u^{n+1}_j \geq o \qquad 4.2.30$$

$$\frac{u^{n+1}_j - u^n_j}{\Delta t} + u^n_j \frac{u^n_j - u^n_{j-1}}{\Delta x} = -\frac{1}{\rho^n_j} \frac{p^n_{j+1} - p^n_{j-1}}{2\Delta x}, \quad u^n_j \geq o \qquad 4.2.31$$

$$\frac{\varepsilon_j^{n+1} - \varepsilon_j^n}{\Delta t} + u_j^{n+1} \cdot \frac{\varepsilon_j^n - \varepsilon_{j-1}^n}{\Delta x} = - \frac{p_j^n}{\rho_j^n} \frac{u_{j+1}^{n+1} - u_{j-1}^{n+1}}{2\Delta x}, \quad u_j^{n+1} \geq o \qquad 4.2.32$$

$$\varepsilon_j^n = \varepsilon(p_j^n, \rho_j^n) \qquad 4.2.33$$

Note that convective terms of the form $u\frac{\partial}{\partial x}$ have been represented by backward differences (Ref. 5) whenever the corresponding velocity is positive. If the velocity is negative, such terms are represented by forward differences.

i.e.

$$u\frac{\partial \rho}{\partial x} \simeq u_j^{n+1} \frac{\rho_j^n - \rho_{j-1}^n}{\Delta x} \quad \text{if} \quad u_j^{n+1} \geq o$$

$$u\frac{\partial \rho}{\partial x} \simeq u_j^{n+1} \frac{\rho_{j+1}^n - \rho_j^n}{\Delta x} \quad \text{if} \quad u_j^{n+1} < o \qquad 4.2.34$$

Equation (4.2.31) is used first to determine new values of u. The advanced values of u are then used to determine p and $\rho$ from (4.2.30), (4.2.32), (4.2.33). Although we made provision for an arbitrary equation of state, all calculations to date have been made for a perfect gas equation of state. The stability condition for the above scheme is:

$$(u \pm c) \frac{\Delta t}{\Delta x} < 1 \qquad 4.2.35$$

An artificial viscosity term may be introduced by making the transformation in (4.2.31) and (4.2.32);

$$p_j^n \rightarrow p_j^n + q_j^n$$

where

$$q_j^n = \begin{cases} \frac{a^2}{8} (\rho_j^n + \rho_j^{n-1}) (u_{j+1}^n - u_{j-1}^n)^2 & \text{if } u_{j+1}^n - u_{j-1}^n \le o \\ o & \text{if } u_{j+1}^n - u_{j-1}^n > o \end{cases} \qquad 4.2.36$$

and in which a is a dimensionless constant of order unity. If one writes $\ell = a\ \Delta x$ and one solves the problem of a plane steady state shock moving in an ideal gas with artificial dissipation corresponding to (4.2.36), one finds the following (Ref. 5). The flow is as for an ideal shock wave of no thickness, except for a transition zone centered about the position of the ideal, discontinuous shock and with width.

$$\Delta = \frac{\pi \ell \sqrt{2}}{\gamma+1} \qquad 4.2.37$$

Let $x_o$ be the "exact" instantaneous position of the shock wave. Denote properties before and behind the shock wave by subscripts 1 and 2 respectively. Then one has in the transition zone:

$$u = \frac{u_2+u_1}{2} + \frac{u_2-u_1}{2} \sin\left\{\sqrt{\frac{\gamma+1}{2}}\ \frac{x - x_o}{\ell}\right\} \qquad 4.2.38$$

$$\frac{1}{\rho} = \frac{1/\rho_2+1/\rho_1}{2} + \frac{1/\rho_2-1/\rho_1}{2} \sin\left\{\sqrt{\frac{\gamma+1}{2}}\ \frac{x-x_o}{\ell}\right\} \qquad 4.2.39$$

$$p+q = \frac{p_1+p_2}{2} - \frac{p_1-p_2}{2} \sin\left\{\sqrt{\frac{\gamma+1}{2}}\ \frac{x-x_o}{\ell}\right\} \qquad 4.2.40$$

$$q = \frac{p_1 - p_2}{2}\ \frac{\gamma+1}{2}\ \frac{\left[\cos\left\{\sqrt{\frac{\gamma+1}{2}}\ \frac{x-x_o}{\ell}\right\}\right]^2}{\frac{\rho_1+\rho_2}{\rho_1-\rho_2} + \sin\left\{\sqrt{\frac{\gamma+1}{2}}\ \frac{x-x_o}{\ell}\right\}} \qquad 4.2.41$$

where
$$x_o - \frac{\Delta}{2} \leq x \leq x_o + \frac{\Delta}{2}$$

From (4.2.37) one may select a value of $\ell$ (and hence a) so that the shock transition region corresponds to 3 or 4 grid intervals. If shocks are present in the initial data of the problem, (4.2.38) to (4.2.41) may be used to approximate them.

The viscous term has the effect of making the stability condition somewhat more stringent than (4.2.39). We used (Ref. 5)

$$\frac{\Delta t}{\Delta x} (|u|+c) < \frac{1}{2} \qquad 4.2.42$$

Thus the solution in period III is obtained by approximating $\overleftarrow{S}_p$ according to (4.2.38) to (4.2.41) and continuing with equations (4.2.33) using the viscous term (4.2.36). The treatment of the boundaries is contained in Ref. 5. The contact surface was handled in a fashion analogous to that indicated previously (equation (4.2.25)) except that the transition relation was:

$$\left(\frac{\rho_B}{\rho_{Bo}}\right)^{\gamma_B} = \left(\frac{\rho_p}{\rho_{po}}\right)^{\gamma_p} \qquad 4.2.43$$

As was noted previously "jitters" or unphysical oscillations may be associated with the artificial dissipation term (see Ref. 1.4). These were eliminated by means of the operator defined in equation (4.2.44) below. The regions known to be free of shock waves were swept every few time steps with the operator

$$\bar{f}_k = f_k + \frac{\nu}{2}\left[f_{k+1} + f_{k-1} + 2f_k\right] \qquad 4.2.44$$

This operator, known as a "smoother" or "filter" (Ref. 12) was applied three successive times in each application and $\nu$ was taken to have the three successive values.

$$\nu_1 = 0.45965$$
$$\nu_2 = -0.22227 + 0.64240\ i \qquad 4.2.45$$
$$\nu_3 = -0.22227 - 0.64240\ i$$

and the subscript k in (4.2.44) was allowed to run over all grid point values in the regions of continuous flow.

(iv) Period IV

The difference scheme (4.2.30) to (4.2.33) may be used in period IV. The dissipation term is not really required since no shock waves occur during this period. The only difficulty is initializing the rarefaction $R_p$. This is discussed in Ref. 5. For the cases under study, period II always occurred and use was made of the finite distribution of the shock wave $\overleftarrow{S}_p$.

We arbitrarily determine the escape time as that instant when the leading edge of $\overleftarrow{S}_p$ reaches the upstream pellet edge. At that time, boundary conditions at the escape front are determined from the values of the flow parameters at the point of maximum pressure and values at intermediate points are determined by linear interpolation between values at the point of maximum pressure and the predicted values at the pellet boundary.

If we write $x_o$ as the position of the pellet boundary at the chosen escape time and $x_1$ for the position of the pressure maximum, the boundary conditions at the escape front are:

$$\rho(x_o) = o \qquad p(x_o) = o$$
$$u(x_o) = u(x_1) - \frac{2}{\gamma_p - 1}\sqrt{\gamma_p \frac{p(x_1)}{\rho(x_1)}} \qquad 4.2.46$$

(v) Period V

As in IV and III one may use the difference scheme (4.2.30) to (4.2.33). One has, however, to initialize the reflected shock wave. Advantage was taken of the finite thickness of the shock. Let $x_1$ be the position of the secondary surface. Then $x_1$ is identified with the back of the reflected wave and the front of the wave is located at $x_o$ given by:

$$x_o = x_1 - \Delta \qquad 4.2.47$$

where $\Delta$ is determined from (4.2.37). The fluid properties $\rho_o = \rho(x_o)$, $p_o = p(x_o)$, $u_o = u(x_o)$ are known at $x_o$. We then take $u_1 = u(x_1) = o$ and use the Rankine-Hugoniot relations to determine $p_1 = p(x_1)$ and $\rho_1 = \rho(x_1)$. One finds:

$$\rho_1 = \rho_o \frac{(u_o - D)}{(u_1 - D)} \qquad 4.2.48$$

$$p_1 = p_o + \rho_o(u_o - D)^2 - \rho_1(u_1 - D)^2 \qquad 4.2.49$$

where $$D = u_o + \frac{(u_1 - u_o) + \sqrt{(u_1 - u_o)^2 + \frac{2c_o^2}{\gamma+1}}}{4/(\gamma+1)} \qquad 4.2.50$$

The calculation then proceeds automatically via equations (4.2.30) to (4.2.33) with the viscous term included. The boundary value

$$u(x_1) = o \qquad 4.2.51$$

is maintained and values of p, $\rho$ at the secondary surface are obtained by interpolation from the interior.

### 4.2.3 Discussion of Results

The model described in the previous section was incorporated into a fortran computer code called "Impaka". Impaka was successfully run with the following data: for like material impacts with $\gamma_p = \gamma_B$ taken successively to be 1.4, 3.0, and 7.0; and for unlike material impacts with $\gamma_p = \gamma_B = 3.0$ and an initial pellet-to-bumper density ratio of 2, 0.5 and 0.1. In this report we do not present the profiles calculated with the above initial data. We will briefly describe the results and discuss in some detail the results of the calculation of the interaction with a secondary surface and the calculation of the decay of the shock wave moving into the pellet. Sample profiles at various times after impact are given in Ref. 5. All the calculations discussed above were terminated when the pellet was completely vaporized except for the like material impact with $\gamma = 3$, in which the expansion of the vapor was followed up to and including interaction with a secondary surface located first 5 and later 100 bumper thicknesses downstream from the point of impact.

Computational stability was observed in all these calculations. The grid ratio was generally taken to be $\Delta x/\Delta t = 5$, the coefficient of artificial viscosity $\ell = 2.5$ and smoothing was generally performed every 25 time steps. The two most important features of the expansion flow were the tendency of the pressure maximum to move to the front of the cloud and the early establishment of self-similar flow. During the period of vaporization, two maxima may be observed for the profile of total pressure. The upstream peak is due to the high pressure behind the shock wave moving into the pellet while the downstream peak is due to the kinetic contribution. Once

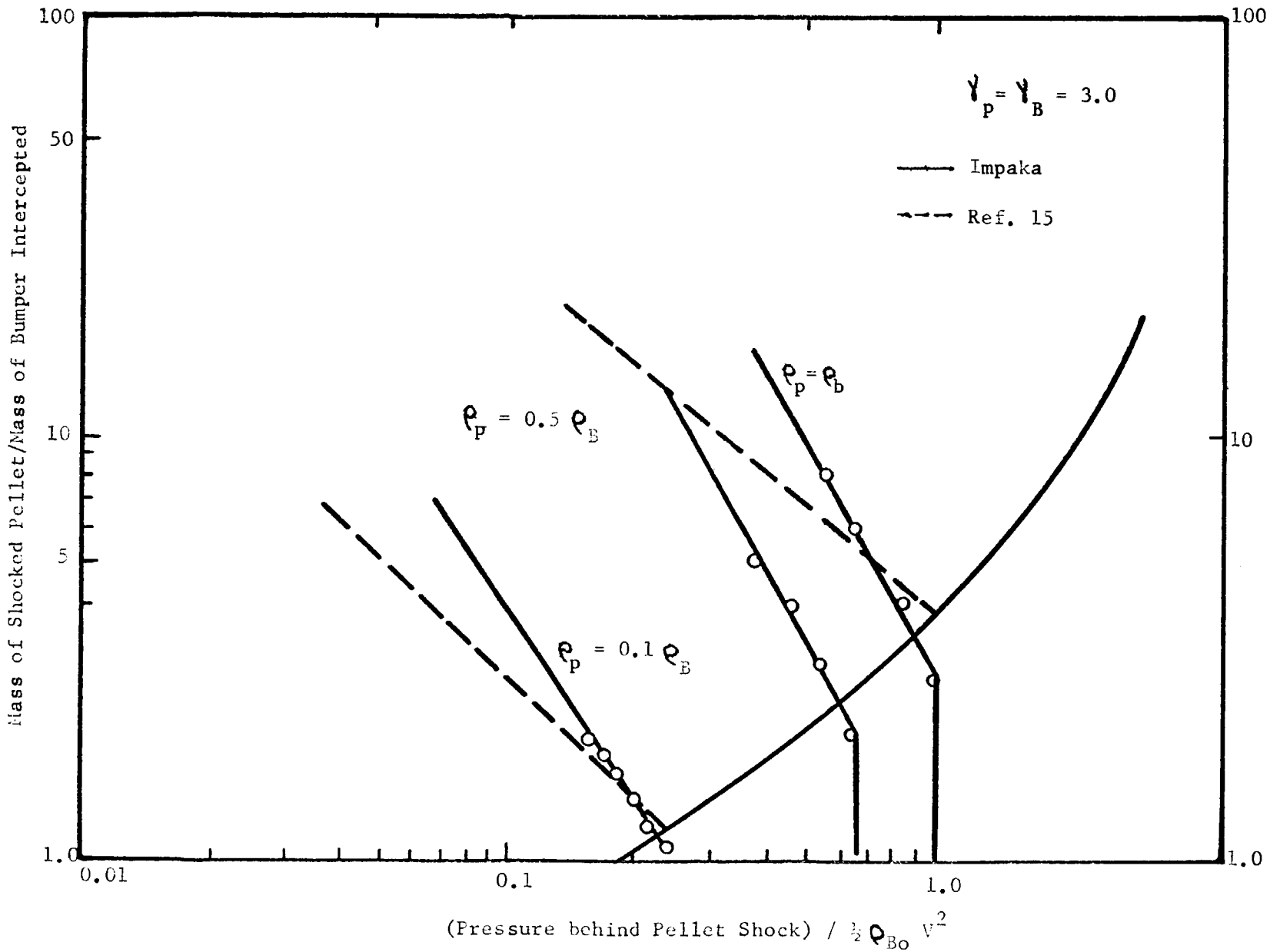


FIG. 4.5 Pressure vs Ratio of Mass of Pellet Shocked to Mass of Bumper

the pellet is completely vaporized the static pressure quickly becomes negligible and only the downstream peak remains. We found that once the cloud had expanded to roughly two or three times its original size, the motion became self-similar. While the late-stage self-similarity of the motion is well known, it is useful to determine how quickly this state is arrived at. One would also expect that the estimate of a one-dimensional model would be conservative in this regard. A two-dimensional model would possess a new degree of freedom for decay of the static pressure. Consequently we conclude that the motion becomes self-similar very shortly after the entire system has vaporized.

In Fig. 4.5 we have plotted as solid line the log of the pressure behind the pellet shock vs the log of the mass of shocked pellet over the mass of bumper intercepted for different pellet-to-bumper density ratios. We took $\gamma_p = \gamma_B = 3$ and $\rho_{po}/\rho_{Bo}$ successfully equal to 1, 0.5 and 0.1. The dotted lines represent results of Friend, Millar, and Murphy (Ref. 15). Their results do not take into account the changing entropy jump across the shock wave during the period in which it is decaying. Consequently the decay in pressure is considerably more rapid than in the present work. Whereas in Ref. 2 the constant $p/\rho^{\gamma}$ required decreasing density with decreasing pressure, the present work maintained the limiting density ratio across the shock. This is consistent with the assumption of negligible pressure ahead of the shock wave. It should also be noted that the current work predicts an earlier commencement of shock decay than does the previous one. This is an error induced by the finite distribution of the shock transition zone. Since the shock wave is spread out, the rarefaction wave

generated at the free surface of the bumper overtakes the pellet shock more quickly than it should.

Fig. 4.6 compares the pressure at a secondary surface with the pressure at the same point in undisturbed flow. As may be seen the maxima of the two distributions are of the same order of magnitude, differing by a factor of 3 or 4. Experimentally one finds very little difference indeed. However, the "free-stream" measurement always involves a bow wave around the tip of the probe. In many cases, the bow wave may be seen clearly on the photographic records accompanying the pressure measurement. Because of the presence of the bow wave it is not surprising that the experimental "free-stream" pressure measurement yields values close to those obtained with a rigid secondary surface. The durations of the calculated pulses are substantially greater than those observed experimentally. The durations observed experimentally are of the order of 10-30 μsec as compared with the duration of ~ 70 μsec indicated in Fig. 4.6. The discrepancy in pulse duration is probably due to the one-dimensional nature of the model. In practice radial motion should provide an important mechanism for diminishing the duration (as well as the amplitude) of the pressure pulse.

The assumption of a perfectly reflecting wall led to enormous reflected pressures when the bumper and wall were very close to each other. The pressures were of the order of the shock pressures. Therefore, the presence of an internal filler between a bumper and the spacecraft hull could produce disastrous results if the shock wave is able to propagate through the filler to the hull or if the filler is sufficiently shocked to vaporize, producing gas under very high pressures in a confined volume. These pressures could

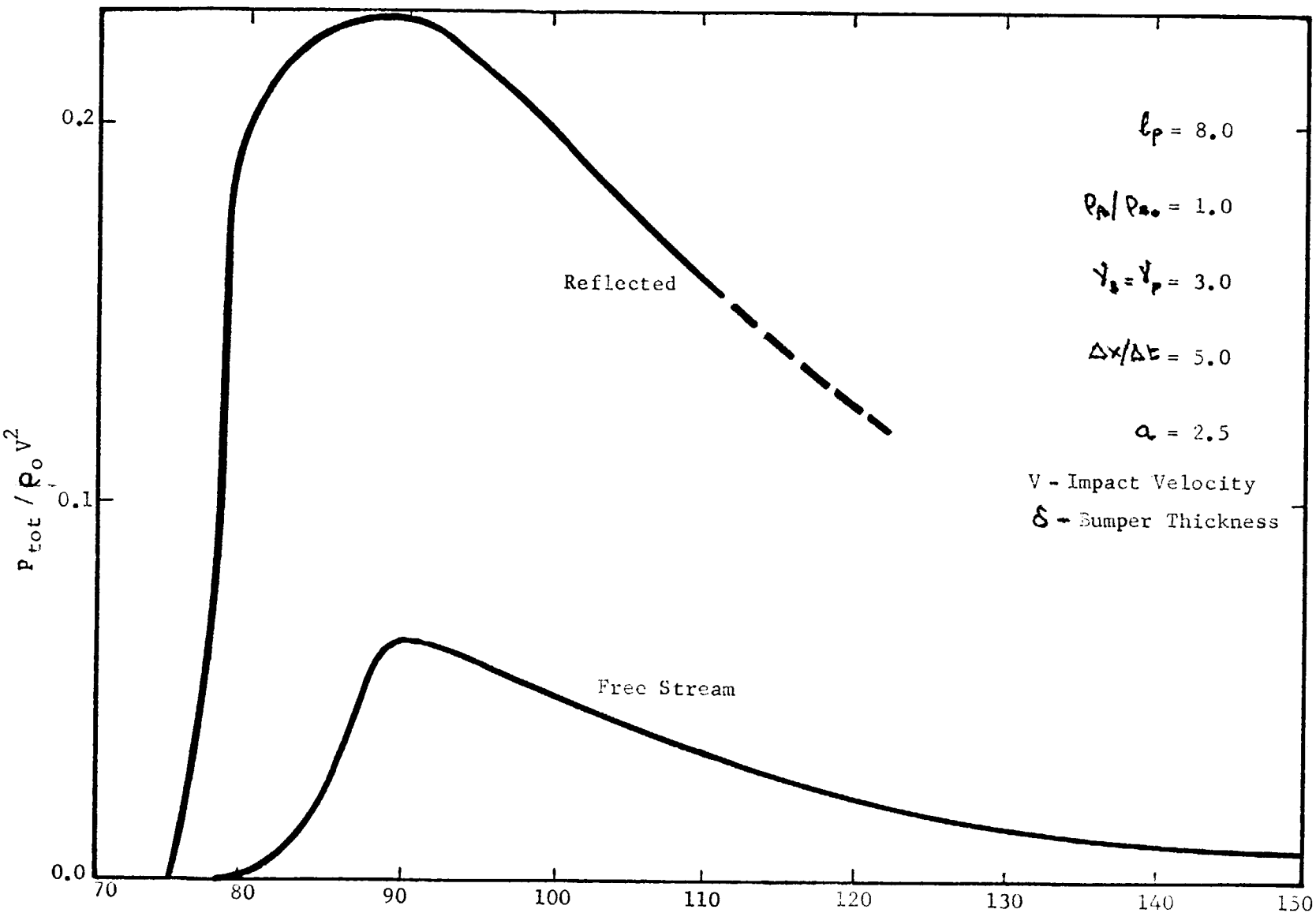


FIG. 4.6 Comparison of Pressure at a Secondary Surface with that of the Undisturbed Flow

produce very large ruptures in the adjacent hull. The differences in impact pressures between lower velocity experimental impacts and the higher velocity meteoroid impacts may produce very different results with filler materials. Even at currently available laboratory velocities, a catastrophic rupture due to filler vaporization may be observed. Friend et al. (Ref. 16) describe impacts onto a system consisting of two parallel sheets filled with polyurethane. The expanding vapor cloud from the outer sheet induced pyrolysis of the filler, producing a high pressure gas in a confined volume. The resulting rupture was far more violent than that observed in the unfilled system.

## 4.3 THEORETICAL STRIP MODEL

A complete analysis of the development of the stip model is given in Reference 8, which was prepared during the past contract period and covers all the theoretical work done on the strip model during the past four years. The state of the strip model at the close of the contract period may be summarized as follows:

Limitations:

1. The hypervelocity impact is axi-symmetrical.
2. Only a thin target (i.e. target thickness 1/10 pellet diameter impact) is applicable.
3. Only like material impacts are considered. Unlike material impact may be approximated by a like material impact with appropriate change in target thickness provided limitation 2 is not exceeded.

4. The accuracy of predicting an ideal equation of state with an artificial polytropic compression exponent $\gamma_s$ obtained to satisfy experimental Hugoniot data and extrapolation of the Hugoniot curve. Very little experimental data is available for the expansion of a highly condensed medium so the polytropic expansion exponent $\gamma_e$ was obtained to satisfy the experimentally determined downstream expansion velocity. The strip model will then satisfy experimental shock Hugoniot data, the downstream expansion boundaries, and conserve mass, momentum and energy within these limits. The resulting pressures within the downstream expansion cloud predicted by the strip model will be within an order of magnitude of the actual pressure, as indeed they are shown to be from experimental pressure probe results (Reference 1).

The supersonic nature of the gas flow within the expansion cloud will result in a bow wave in front of the pressure probe. The resulting pressure loss across the bow wave was allowed for in comparing theoretical and experimental results.

The greatest source of error in the strip model predictions is due to the upstream expansion flow observed experimentally. Much time was spent trying to predict theoretically upstream expansion flows. A variable $\gamma$ and pellet shock decay were allowed for without success. The effect on the stagnation pressure if upstream flow is not predicted is uncertain. Qualitatively, the pressure will be greater due to momentum conservation on a

total integrated basis, and the mass will be less.

Impacts at projected meteoroid velocities may, and have been predicted using the strip model with the previously outlined restrictions (limitation no. 4). The accuracy of these predictions may be altered due to ionization effects which could be large at projected meteoroid velocities. If large amounts of energy are initially converted into ionizing the compressed material, then the initial escape front velocities would be lower than those predicted with a model which neglects ionization effects. In other words the escape velocity would no longer be equal to 1.5 times the impact velocity, as found in the experimental range, but would be somewhat less. At present ionization energies are not allowed for in the model and hence pressures at specified spacings downstream of the target would tend to be too high due to the higher axial velocities predicted.

As mentioned at the beginning of this section, most of the theoretical work on the strip model during the past year was directed towards a more accurate determination of the initial impact conditions. A better insight into the initial physics of the shock processes was obtained, and in particular the failure of the model to predict the large experimentally observed upstream expansion flows was recognized. However, despite this failure, relatively close agreement was obtained between the theory and experimental results for peak centerline pressures vs spacing (Ref. 1).

Fig. 4.7 presents theoretical stagnation pressures, densities, and velocities along the axis of symmetry for three time increments after impact. The initial impact conditions for these figures are for an impact of 65,000 ft/sec (20 km/sec). No information is available for comparing

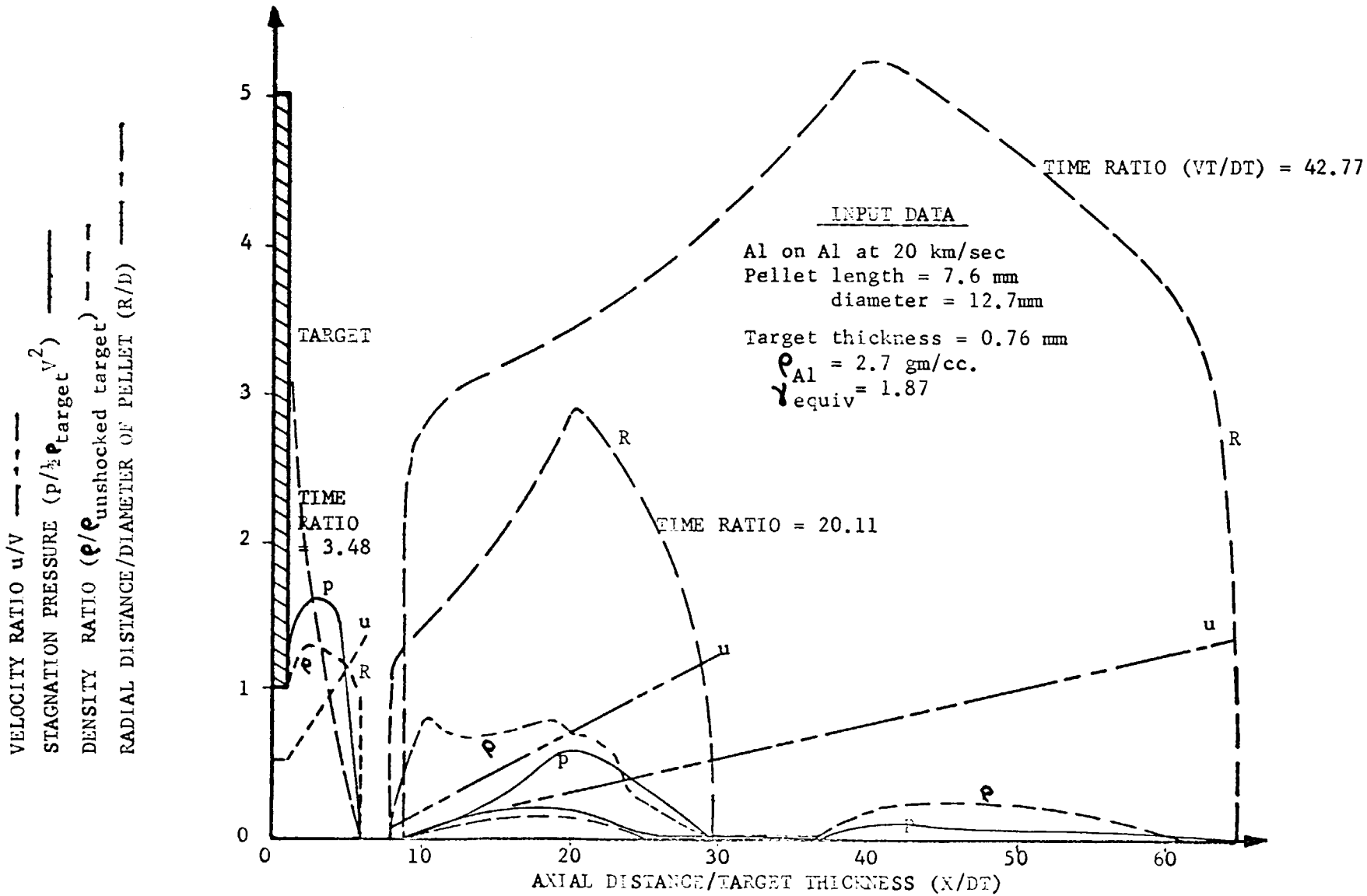


Fig.4.7 Theoretical Expansion Cloud Characteristics at three different times. Al on Al impact at 20 km/sec.

these results of a predicted meteoroid impact. Reservations on the accuracy of these results are mainly limited to the effect of ionization, which was discussed previously. The results were presented in this form for convenience as this is the form obtained from the programmed graph routine. In addition to this information, peak pressure vs spacing and radial distributions at various axial positions within the expansion cloud may also be obtained. Only 3 of some 20 time increments after impact were shown as relatively smooth transitions occurred between the three time increments shown.

## 5.0 THE GRID BUMPER

The possibility of substituting a wire mesh or grid for the standard solid Whipple bumper has been investigated. The analysis was based on a bumper weight equivalent to a solid .001 in. (.00255 cm) thick lead bumper which is the design thickness for an 0.1 gm mass, 0.44 gm/cm$^3$ density, 30.48 km/sec meteoroid.

The grid bumper could be constructed from woven wire strands of solid metal, metal coated mylar, perforated sheets of solid metal, or metal deposit on a mylar mesh or perforated mylar sheet. There are many possibilities, but for simplicity solid lead wire was chosen. Obviously the strand or metal density will influence the wire diameter and grid spacings so that virtually any value of open to closed area is possible. Assuming that the thickness of the equivalent solid bumper had been determined from the design limit considerations, and the required wall thickness to withstand the vapor/debris cloud pressure is known, one can compute the maximum size of meteoroid which will not penetrate an unprotected wall from ballistic limit calculations. This would then fix the spacing requirement for the grid bumper strands (equal to, or slightly less than the maximum diameter of the meteoroid which will not penetrate the unprotected wall). Radiative efficiency or solar flux intensity permissible on the spacecraft wall considerations would then be used to compute the open area to closed area requirements and thus the wire size and mean density would be fixed.

The grid bumper could, therefore, serve a double purpose; it protects the spacecraft from meteoroid impacts and serves as a heat shield to control solar heating and/or heat losses to outer space.

The efficiency of the grid as a thermal barrier has not been considered in other than a qualitative way. The purpose of this note is to outline the possibilities of the system and to compute some typical examples from meteoroid protection considerations only.

Calculations of Specific Bumper Grid Sizes

a) Control bumper, 0.001" thick Pb. (0.00255 cm)

b) Wire density, 11.3 $gm/cm^2$

c) Weight of control bumper = 0.0291 $gm/cm^2$

d) Weight of wire grid bumpers = 0.0291 $gm/cm^2$ (constant)

e) Typical section

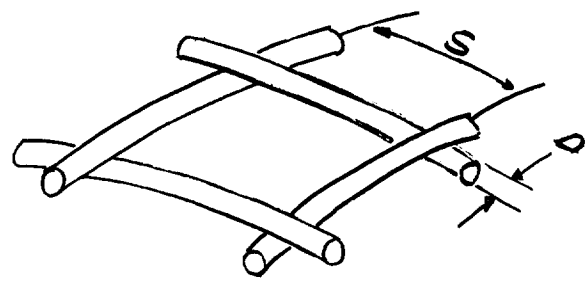


f) Weight of grid bumper is given by

$\frac{\pi D^2}{4}\rho\left(\frac{1}{s+D}\right)$ $gm/cm^2$ for a single parallel strand construction, or

$\frac{\pi D^2}{4}\rho\left(\frac{2}{s+D}\right)$ $gm/cm^2$ for woven construction

g) Ratio of open to closed area for woven construction is given by $\{s/(s+D)\}^2$

h) Results $s = 610D^2 - D$ for S,D in cm,

$\rho = 11.3\ gm/cm^3$. $m = .0291$ gm

A Preliminary Analysis of the Grid Bumper

The purpose of this section is to describe a new bumper system which appears to be as effective in spreading meteoroid momentum as an equivalent weight "Whipple" bumper, and which, in addition, offers minimum interference with existing super-insulation schemes. The bumper system consists of a grid or screen of fine, dense wires which will prevent dangerously large meteoroids from impacting directly against the spacecraft hull or super-insulation panels, and yet transmit significant radiation to or from the spacecraft surface or insulation panels. Typical grid sizes and wire dimensions for specific spacecraft protection were discussed in a previous section. Some experimental results of a laboratory size grid bumper are presented and compared with the equivalent "Whipple" bumper. A tentative discussion of the physical mechanism leading to the significantly different results is presented.

The laboratory test is illustrated by the following sketch.

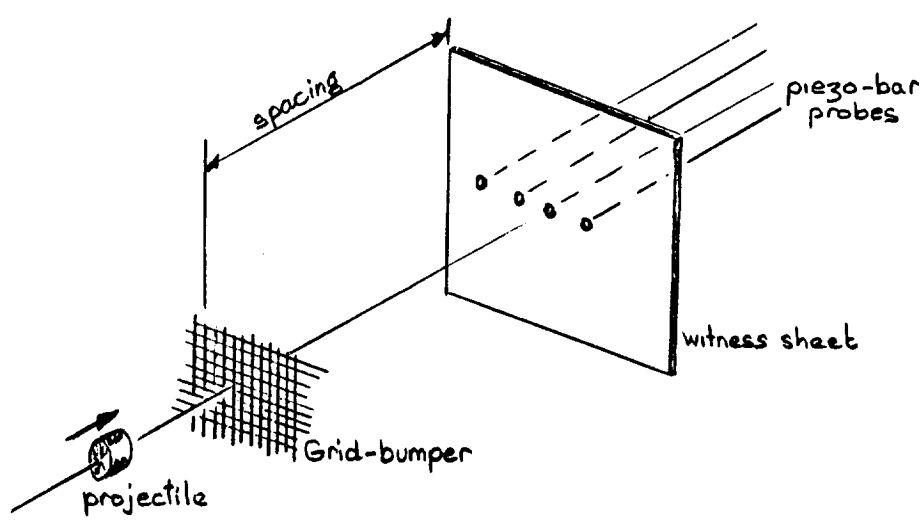

Conditions

a) Projectile: Lexan cylinder 0.500 in. (1.27 cm) dia. x .285 in (0.725 cm) long.

b) Bumper: Grid wire diameter .015 in (.038 cm) lead

Grid spacing .020 in (.051 cm)

Grid weight .291 $gm/cm^2$

Equivalent solid bumper .010 in (.025 cm) lead foil

c) Witness sheet: Spacing from bumper 6 in (15.2 cm)

Material ¼ in (.635 cm) aluminum

d) Pressure probes: One on centerline

One 2 in (5.08 cm) off-axis in second surface

e) Camera: B & W 192

Qualitative Results

The simplest method of interpreting the effectiveness of the grid bumper is to compare the experimental results obtained in the present test series (five shots) with the equivalent Whipple bumper tests. The significant differences are immediately apparent if one compares the cloud shape and pressure traverse results.

1. Cloud Shape: The most apparent difference is the absence of significant upstream flow. The overall cloud shape is similar to that obtained with a solid lexan bumper, except that the axial expansion appears to be much more rapid. Preliminary measurements of axial velocities indicate that the cloud expansion front is travelling at approximately twice the impact velocity. Little change is observed, however, in radial velocities.

2. Pressure Profiles: The measurement made at the same spacing with the equivalent weight solid lead bumper indicates a peak pressure of 40,00 psi on the centerline, and approximately one-quarter of the peak value at a position 2 in. off-axis. The present series indicates a peak pressure of 30,000 psi on the centerline, and approximately one eighth of the peak value at the 2 in. off-axis position. In addition, the "grid" pressure profile does not have the same overall shape with time. The pressure pulse has a longer duration, approximately 25 μsec and does not exhibit two maxima. The latter observation suggests either more complete vaporization of the pellet, or possibly turbulent mixing within the cloud, or both.
3. Witness Sheet: The witness sheet shows no significant particle impacts.

Discussion of Results

The scant experimental data precludes a detailed analysis of this time. Certainly, pellet vaporization appears to be more complete. However, it is difficult to estimate how the different pressure distribution will affect protection. This question is best answered experimentally, by a comparative ballistic limit series.

Interpretation

The interaction between the pellet and the grid bumper is obviously much more complex than that of a solid thin sheet, particularly since the

wires are arranged in two orthogonal layers. No simple shock wave system can describe the behaviour or properties of the shocked bumper grid, nor can a simple analysis be applied directly to the pellet shock system. The system of individual cylindrical shock waves emanating from each grid wire intersected by the pellet (in this case, fourteen from each layer) must interact to form a single destructive wave, yet the flow field behind the wave is not simple. The pellet shock appears not to advance upstream into the pellet, since no significant upstream flow is observed. This suggests a weaker pellet shock; however, since the vaporization appears to be, if anything, more complete, there is an apparent contradiction.

The flow of pellet material through the shocked bumper grid may well be highly turbulent, with the result that considerable energy is transformed into vortex flow and eddy currents. The hypothesis is consistent with the state of the cloud boundary, i.e. locally irregular as compared with the smooth surface seen on clouds resulting from standard bumper tests.

The internal cloud turbulence which should result in the complete mixing of the bumper and pellet materials may well be the main factor influencing the drastically different results obtained with the grid bumper. If this is the case, it is unlikely that the particular choice of grid employed in these experiments is the optimum. An extensive program to investigate such factors as the particle size and density in relation to grid wire diameter and density and grid spacing as well as grid geometry and particle velocity is required before any general description of the ultimate effectiveness of the grid bumper as a minimum weight protection system can be made. The effectiveness of the system to defeat meteoroids which are smaller and slower than

the specific design case should be studied. Since, in general, the grid wire diameter is larger than the thickness of the equivalent weight solid bumper, the grid bumper may be more effective in fragmenting or pulverizing meteoroids impacting at relatively low velocities.

The potential value of the grid system over the conventional "Whipple" bumper appears to be enormous. It offers improved protection with less weight, with the added flexibility of controllable optical and radiative transmissivity.

Applications

In Section 2 the application of the grid bumper as a combined meteoroid screen and radiation shield was suggested. An obvious extension is the potential application of the grid bumper as a meteoroid screen over window areas for extended manned spacecraft missions where both meteoroid protection and external visual observations are required.

Of more direct application to fuel storage vehicles is the distinct possibility of incorporating the grid bumper in the outer insulation layer. For fuel storage modules of the Apollo class where exposures of 200 to 400 $ft^2$ for 30 to 60 days are anticipated ($6 \times 10^3$ to $2.5 \times 10^4$ $ft^2$ days), Section 2 indicated that a solid lead bumper 0.0001 in. (.000254 cm) thick would be sufficient to ensure total vaporization of the design meteoroid (.01 gm at 30.5 km/sec). The subsequent vehicle surface pressure loading was computed to be 1 and 0.1 kb at 7.2 and 15.5 cm spacings respectively (15,000 and 1500 psi at 2.85 and 6.1 in. spacing).

Application of the equivalent mass principle outlined in Section 2 suggests that a grid bumper constructed of 0.02 mm diameter lead wires with

0.232 mm mean spacing could be utilized as an equivalent system (approximately .001 in. diameter x .010 in. spacing). The impacting (design) meteoroid would strike approximately fourteen grid strands from each layer. Many alternate grids are also possible, i.e. .01 mm diameter x .05 mm spacing with approximately 60 (sixty) grid strands from each layer.

Incorporating the grid bumper in the outer insulation layer, spaced 3 to 6 inches from the next inner layer, appears to be reasonable and possible. The total weight of the metallic grid surrounding a 200 $ft^2$ exposed surface is approximately 1.5 lb. If, in incorporating the grid bumper in the insulation system no extra support system is required, complete meteoroid protection is possible with no significant weight penalty.

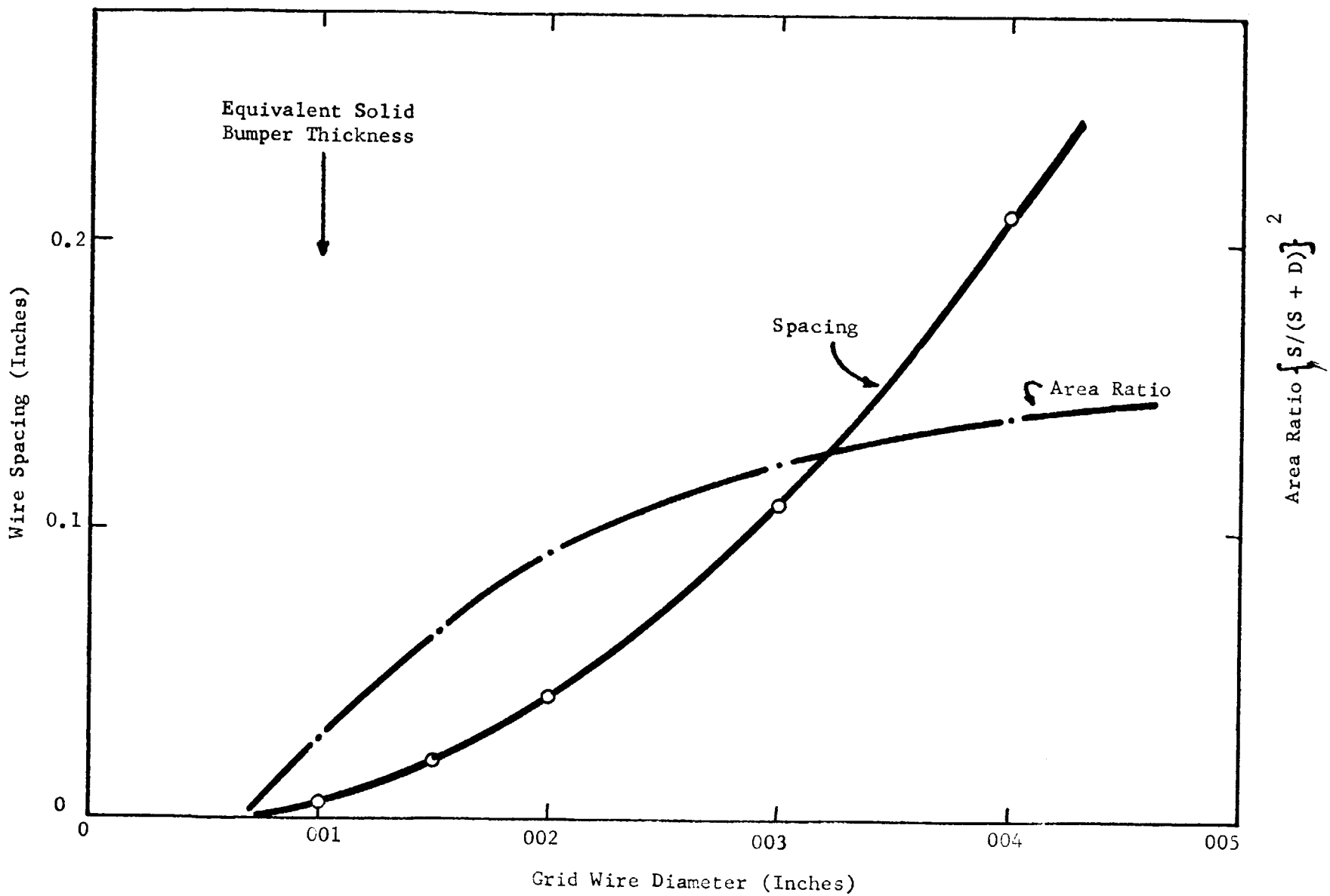


FIG. 5.1 Grid Bumper Characteristics Equivalent to a .001 in. Lead Sheet Bumper

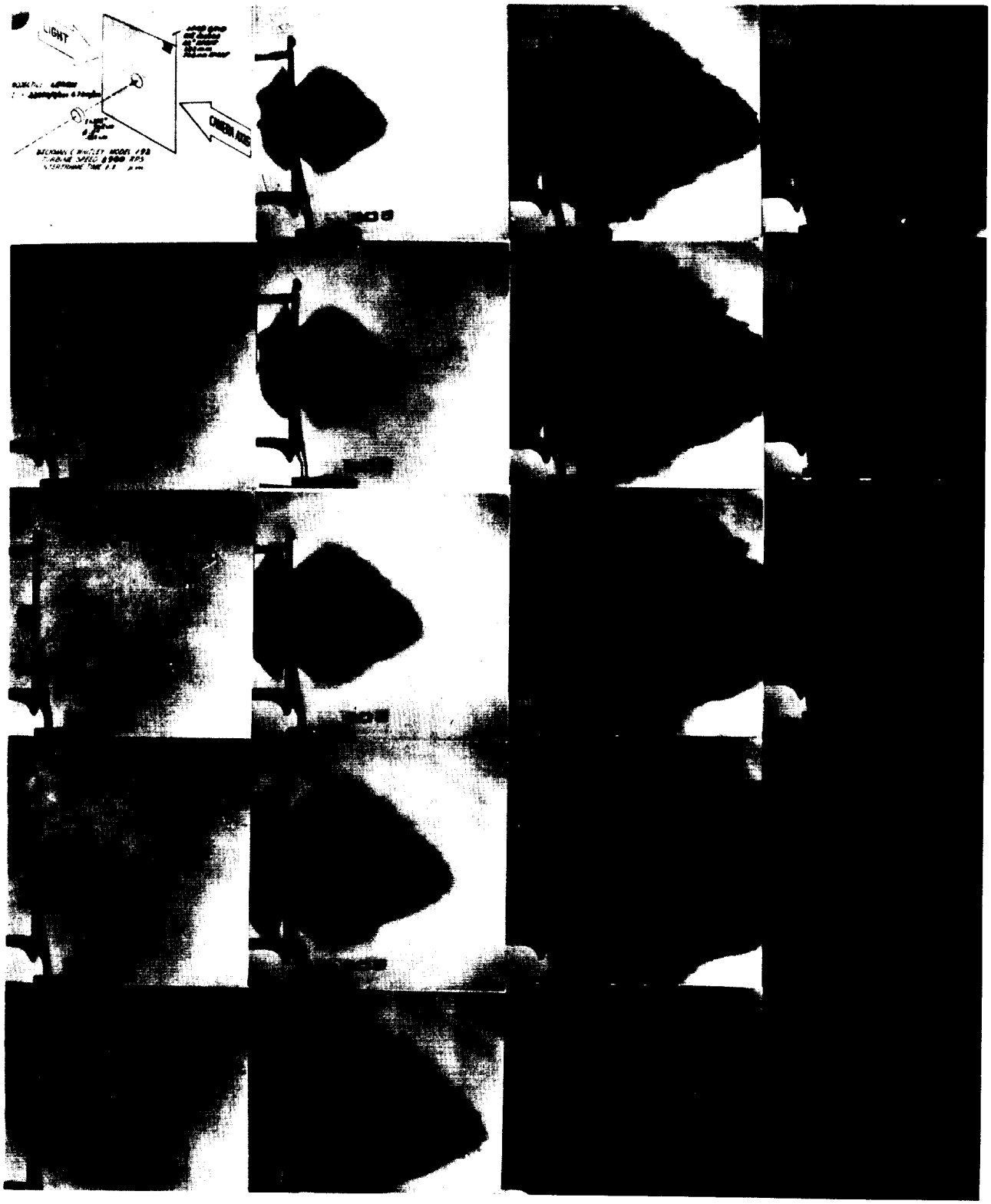


FIG. 5.2 Photographs of B and W Coverage of Impact of Lexan Projectile Impacting on Lead Wire Grid

## CONCLUDING REMARKS

From the investigation into the properties of the expansion cloud generated by the hypervelocity impact of a pellet into a thin shield the following observations and recommendations may be made:

1. The piezo-bar pressure gauge may be used to obtain reliable measurements of the pressure in a plasma. The measurements are not affected by high temperatures or by the presence of small particles or free electrons within the debris cloud.

2. The secondary peak frequently observed in the pressure probe measurements is due to unvaporized material.

3. In a completely vaporized cloud the pressure pulse may be approximated by a Gaussian distribution in space and time.

4. From Beckman and Whitley photographic data, one may obtain useful information concerning the modes of failure of secondary surfaces loaded by the debris cloud.

5. One may determine the Hugoniot for an impacting or impacted material by photographic location of the impact generated shock waves at any time.

6. At meteoroid velocities shape effects should be unimportant for downstream spacings greater than five to ten projectile diameters.

7. The multifoil system possesses distinct advantages over the double wall system under impact conditions such that the projectile is not vaporized. However, once the projectile is vaporized, the double wall structure becomes a more efficient protection scheme for any given weight.

8. It appears that substitution of a grid for a solid bumper involves no loss in protection, while providing a window for radiation. An investigation into the properties of the grid-bumper is recommended.

9. The Hugoniot curve for Lexan should be obtained by more precise measurements and for pressures corresponding to maximum attainable velocities.

10. It is desirable to extend gun launch capabilities to the 15 to 20 km/sec range.

## REFERENCES

1. FRIEND, W.H.; MURPHY, C.L.; and SHANFIELD, I.
"Review of Meteoroid - Bumper Interaction Studies at McGill University". NASA CR-54857, August 1966.

2. FRIEND, W.H.; MILLAR, D.A.J.; and MURPHY, C.L.
"The Hypervelocity Impact of Pellets with Thin Plates Theoretical Considerations, Part II". McGill University Report 62-8, October 1962.

3. BULL, G.V., MURPHY C.L., ZWARTS, F.J.; and FRIEND, W.H.
"Review of Hypervelocity Impact Studies at McGill University". McGill University Report 63-15, December 1963.

4. BULL, G.V.
"On the Impact of Pellets with Thin Plates"
McGill University TN-1-10/61, October 1961.

5. GOUGH, P.S.
"A One-dimensional Analysis of the Hypervelocity Impact of a Pellet into a Thin Bumper". NASA CR-54725, November 1967.

6. ZWARTS, F.
"The Initial One-Dimensional Expansion of the Shocked States Generated by the Impact of Cylindrical Pellets with Thin Plates". McGill University TN-64-6, August 1964.

REFERENCES CONT'D

7. RINEY, T.D. and Heyda, J.F.
"Hypervelocity Impact Calculation Proceedings". 7th Hypervelocity Impact Symposium Vol. 2, February 1965.

8. MURPHY, C.L.
"Theoretical Strip Model for Hypervelocity Impact". (Progress Report) To be published.

9. RAE, W.J. and KIRCHNER, H.P.
"Final Report on a Study of Meteoroid Impact Phenomena". Cornell Aeronautical Laboratory, Report RM-1655-M-4, February 1963.

10. WALSH, J.M. and JOHNSON, W.F.
"On the Theory of Hypervelocity Impact". 7th Hypervelocity Impact Symposium Vol. IV.

11. WAGNER, N.H., BROOKS, N.B., and BJORK, R.L.
"Impact of a Porous Aluminum Projectile on Aluminum at 20 and 72 km/sec". 7th Hypervelocity Impact Symposium Vol. III.

12. SHUMAN, F.G.
"Numerical Methods in Weather Prediction: II Smoothing and Filtering". Monthly Weather Review (November, 1957).

13. RICHTMYER, R.D.
"Difference Methods for Initial-Value Problems". Interscience Publishers, Inc. (New York).

14. RICHTMYER, R.D.
"A Survey of Difference Methods for Non-Steady Fluid

REFERENCES CONT'D

Dynamics". National Centre for Atmospheric Research, Boulder Colorado 80301 NCAR Tech. Note 63-2.

15. FRIEND, W.H.; CARON, A.P., MOLDER, S.; CHEPURNIY, N.; and WATKINS, W.A.
"An Investigation of Explosive Oxidations Initiated by Hypervelocity Impacts". AFFDL-TR-67-92.

DISTRIBUTION LIST

| | COPIES |
|---|---|
| **National Aeronautics and Space Administration**<br>Lewis Research Center<br>21000 Brookpark Road<br>Cleveland, Ohio 44135 | |
| Attention: Contracting Officer, MS 500-313 | 1 |
| Liquid Rocket Technology Branch, MS 500-209 | 8 |
| Technical Report Control Office, MS 5-5 | 1 |
| Technology Utilization Office, MS 3-16 | 1 |
| AFSC Liaison Office, MS 4-1 | 2 |
| Library | 2 |
| Office of Reliability and Quality Assurance, MS 500-111 | 1 |
| E. W. Conrad, MS 500-204 | 1 |
| D. L. Nored, MS 500-209 | 1 |
| **National Aeronautics and Space Administration**<br>Washington, D.C. 20546 | |
| Attention: Code MT | 1 |
| RPX | 2 |
| RPL | 2 |
| SV | 1 |
| RV-2 | 2 |
| **Scientific and Technical Information Facility**<br>P.O. Box 33<br>College Park, Maryland 20740 | |
| Attention: NASA Representative<br>Code CRT | 6 |
| **National Aeronautics and Space Administration**<br>Ames Research Center<br>Moffett Field, California 94035 | |
| Attention: Library | 1 |
| **National Aeronautics and Space Administration**<br>Flight Research Center<br>P.O. Box 273<br>Edwards, California 93523 | |
| Attention: Library | 1 |

| | COPIES |
|---|---|
| National Aeronautics and Space Administration<br>Goddard Space Flight Center<br>Greenbelt, Maryland 20771 | |
| Attention: Library | 1 |
| W. M. Alexander | 1 |
| National Aeronautics and Space Administration<br>John F. Kennedy Space Center<br>Kennedy Space Center, Florida 32899 | |
| Attention: Library | 1 |
| National Aeronautics and Space Administration<br>Langley Research Center<br>Langley Station<br>Hampton, Virginia 23365 | |
| Attention: Library | 1 |
| Robert Hayduk | 1 |
| National Aeronautics and Space Administration<br>Manned Spacecraft Center<br>Houston, Texas 77001 | |
| Attention: Library | 1 |
| Paige B. Burbank | 1 |
| B. Cour Palais | 1 |
| National Aeronautics and Space Administration<br>G. C. Marshall Space Flight Center<br>Huntsville, Alabama 35812 | |
| Attention: Library | 1 |
| Keith Chandler, R-P&VE-PA | 1 |
| R. Naumann, R-RP-P | 1 |
| Orlo K. Hudson, R-RP-J | 1 |
| Jet Propulsion Laboratory<br>4800 Oak Grove Drive<br>Pasadena, California 91103 | |
| Attention: Library | 1 |
| Charles Campen | 1 |
| Dr. V. Jaffe | 1 |
| C. L. Robillard | 1 |
| Dwayne F. Spencer | 1 |

| | COPIES |
|---|---|
| Office of the Director of Defense Research & Engineering<br>Washington, D.C. 20301 | |
| Attention: Dr. H. W. Schulz, Office of Assistant Director (Chem. Technology) | 1 |
| RTD (RTNP)<br>Bolling Air Force Base<br>Washington, D.C. 20332 | |
| Attention: J. Minette | 1 |
| E. A. Kritzer | 1 |
| Arnold Engineering Development Center<br>Air Force Systems Command<br>Tullahoma, Tennessee 37389 | |
| Attention: Library | 1 |
| Advanced Research Projects Agency<br>Washington, D.C. 20525 | |
| Attention: D. E. Mock | 1 |
| Wright-Patterson Air Force Base<br>Dayton, Ohio 45433 | |
| Attention: AFML (MAAE) | 1 |
| AFML (MAAM) | 1 |
| Air Force Office of Scientific Research<br>Washington, D.C. 20333 | |
| Attention: SREP, Dr. J. F. Masi | 1 |
| Office of Research Analyses (OAR)<br>Holloman Air Force Base,<br>New Mexico 88330 | |
| Attention: RRRT | 1 |
| U.S. Army Missile Command<br>Redstone Scientific Information Center<br>Redstone Arsenal, Alabama 35808 | |
| Attention: Chief, Document Section | 1 |

| | COPIES |
|---|---|
| Commanding Officer<br>Ballistic Research Laboratories<br>Aberdeen Proving Ground, Maryland 21005 | |
| Attention: AMXBR-1 | 1 |
| Department of the Army<br>U.S. Army Materiel Command<br>Washington, D.C. 20315 | |
| Attention: AMCRD-RC | 1 |
| Bureau of Naval Weapons<br>Department of the Navy<br>Washington, D.C. 20360 | |
| Attention: DLI-3 | 1 |
| Commander<br>U.S. Naval Missile Center<br>Point Mugu, California 93041 | |
| Attention: Technical Library | 1 |
| Commanding Officer<br>Office of Naval Research<br>1030 E. Green Street<br>Pasadena, California 91101 | 1 |
| Commander<br>U.S. Naval Ordnance Test Station<br>China Lake, California 93557 | |
| Attention: Technical Library | 1 |
| Commander<br>U.S. Naval Weapons Laboratory<br>Dahlgren, Virginia 22448 | |
| Attention: Technical Library | 1 |
| Director (Code 6180)<br>U.S. Naval Research Laboratory<br>Washington, D.C. 20390 | |
| Attention: W. W. Atkins | 1 |
| M. A. Persechino | 1 |
| Acrojet-General Corporation<br>P.O. Box 296<br>Azusa, California 91703 | |

| | COPIES |
|---|---|
| Attention: Librarian | 1 |
| Aerojet-General Corporation<br>11711 S. Woodruff Avenue<br>Downey, California 90241 | |
| Attention: F.M. West, Chief Librarian | 1 |
| J. F. Collinane | 1 |
| Aerospace Corporation<br>P.O. Box 95085<br>Los Angeles, California 90045 | |
| Attention: Library - Documents | 1 |
| Aero-Space Corporation<br>El Segundo, California | |
| Attention: Verne C. Frost | 1 |
| Avco Corporation<br>Wilmington, Massachusetts 01887 | |
| Attention: Robert R. McMath - RAD | 1 |
| Arthur D. Little, Inc.<br>Acorn Park<br>Cambridge 40, Massachusetts | |
| Attention: Reed H. Johnston | 1 |
| ARO, Incorporated<br>Arnold Engineering Development Center<br>Arnold AF Station, Tennessee 37389 | |
| Attention: Dr. B. H. Goethert, Chief Scientist | 1 |
| Julium Lukasiewicz | 1 |
| Battelle Memorial Institute<br>505 King Avenue<br>Columbus, Ohio 43201 | |
| Attention: Report Library, Room 6A | 1 |
| Bell Aerosystems, Inc.<br>Box 1<br>Buffalo, New York 14205 | |
| Attention: T. Reinhardt | 1 |

| | COPIES |
|---|---|
| Boeing Company<br>Aero-Space Division<br>P.O. Box 3707<br>Seattle, Washington 98124 | |
| Attention: Ruth E. Peerenboom (1190) | 1 |
| Jack Lundeberg | 1 |
| Chemical Propulsion Information Agency<br>Applied Physics Laboratory<br>8621 Georgia Avenue<br>Silver Spring, Maryland 20910 | 1 |
| Chrysler Corporation<br>Space Division<br>P.O. Box 26018<br>New Orleans, La. | |
| Attention: Librarian | 1 |
| Cornell Aeronautical Laboratory, Inc.<br>Buffalo, New York | |
| Attention: Dr. William Rae | 1 |
| Canadian Commercial Corporation<br>70 Lyon Street<br>Ottawa 4, Ontario | |
| Attention: W. J. Washburn, Air Services Branch | 1 |
| Computing Devices of Canada Limited<br>P.O. Box 508<br>Ottawa 4, Canada | |
| Attention: Ron Montgomery | 1 |
| Chance Vought Corporation Library<br>Box 5907<br>Dallas, Texas | 1 |
| Douglas Aircraft Company, Inc.<br>Santa Monica Division<br>3000 Ocean Park Blvd.<br>Santa Monica, California 90405 | |
| Attention: H. H. Dixon | 1 |

| | COPIES |
|---|---|
| Drexel Institute of Technology<br>Dept. of Mechanical Engineering<br>Philadelphia 4, Penna. | |
| Attention: Prof. Pei Chi Chou | 1 |
| University of Denver<br>Denver Research Institute<br>P.O. Box 10127<br>Denver, Colorado 80210 | |
| Attention: Security Office | 1 |
| R.E. Recht, Mechanics Division | 1 |
| General Dynamics/Astronautics<br>P.O. Box 1128<br>San Diego, California 92112 | |
| Attention: Library & Information Services (128-00) | 1 |
| General Dynamics/Convair<br>P.O. Box 1128<br>San Diego, California 92112 | |
| Attention: J. Fager, Dept. 512-2 | 1 |
| General Electric Company<br>Valley Forge Space Technology Center<br>P.O. Box 8555<br>Philadelphia, Penna. 19101 | |
| Attention: Library | 1 |
| J. F. Heyda (TEMO) | 1 |
| Grumman Aircraft Engineering Corporation<br>Bethpage, Long Island<br>New York | |
| Attention: Library | 1 |
| Joseph Gavin | 1 |
| John Tlasmati | 1 |
| IIT Research Institute<br>Technology Center<br>Chicago, Illinois 60616 | |
| Attention: C. K. Hersh, Chemistry Division | 1 |
| Dr. R. H. Kornish | 1 |

| | COPIES |
|---|---|
| Institute for Defense Analyses<br>400 Army-Navy Drive<br>Arlington, Virginia 22202 | |
| Attention: Classified Library | 1 |
| Harvard College Observatory<br>Cambridge, Massachusetts | |
| Attention: Prof. F. L. Whipple | 1 |
| Fundamental Methods Associates<br>31 Union Square West<br>New York 2, N.Y. | |
| Attention: Dr. Carl Klahr | 1 |
| General Motors Corporation<br>Manufacturing Development<br>General Motors Technical Center<br>Warren, Michigan 48090 | |
| Attention: Dr. C.J. Maiden | 1 |
| Lockheed Missiles & Space Company<br>P.O. Box 504<br>Sunnyvale, California 94087 | |
| Attention: Library | 1 |
| Lockheed Missiles and Space Company<br>Palo Alto, California | |
| Attention: P.E. Sandorff | 1 |
| Lockheed Missiles & Space Company<br>Propulsion Engineering Division (D.55-11)<br>1111 Lockheed Way<br>Sunnyvale, California 94087 | 1 |
| Marquardt Corporation<br>16555 Sticoy Street<br>Box 2013-South Annex<br>Van Nuys, California 91404 | |
| Attention: Librarian | 1 |
| Martin Company<br>P.O. Box 179<br>Denver, Colorado | |
| Attention: Dr. Arthur Ezra | 1 |

| | COPIES |
|---|---|
| Martin Company<br>Science Technology Library<br>Mail 398<br>Baltimore 3, Maryland | 1 |
| McDonnell Aircraft Corporation<br>P.O. Box 6101<br>Lambert Field, Missouri | |
| Attention: R. A. Herzmark | 1 |
| North American Aviation, Inc.<br>Space & Information Systems Division<br>12214 Lake wood Blvd.<br>Downey, California 90242 | |
| Attention: E. R. Mertz | 1 |
| Technical Information Center, D/096-722(AJ01) | 1 |
| New York University<br>College of Engineering<br>Research Division<br>University Heights<br>New York 53, N.Y. | |
| Attention: Dr. Paul F. Winternite | 1 |
| Republic Aviation Corporation<br>Farmingdale, Long Island<br>New York | |
| Attention: Sol Saul, Space Systems Structures | 1 |
| Republic Aviation<br>333 West 1st Street<br>Dayton 2, Ohio | |
| Attention: Paul Rossow | 1 |
| Rocketdyne Division of NAA, Inc.<br>6633 Canoga Avenue<br>Canoga Park, California 91304 | |
| Attention: Library, Dept. 596-306 | 1 |

| | COPIES |
|---|---|
| Rand Corporation<br>Santa Monica, California | |
| Attention: Robert A. Popetti | 1 |
| James Rosen | 1 |
| Jack E. Whitener | 1 |
| Sandia Corporation<br>Albuquerque, New Mexico | |
| Attention: Walter Herrmann | 1 |
| University of California<br>Los Alamos Scientific Laboratory<br>P.O. Box 1663<br>Los Alamos, New Mexico | 1 |
| Institute of Aerospace Studies<br>University of Toronto<br>Toronto 5, Ontario | |
| Attention: Dr. I. I. Glass | 1 |
| Utah Research and Development<br>2175 South 3270 West<br>Salt Lake City, Utah | |
| Attention: Boyd Baugh | 1 |
| United Aircraft Corporation<br>United Technology Center<br>P.O. Box 358<br>Sunnyvale, California 94088 | |
| Attention: Librarian | 1 |
| TRW Systems, Inc.<br>1 Space Park<br>Redondo Beach, California 90200 | |
| Attention: G. W. Elverum | 1 |
| STL Technical Library Document Acquisitions | 1 |
| United Aircraft Corporation<br>Corporation Library<br>400 Main Street<br>East Hartford, Connecticut 06118 | |
| Attention: Dr. David Rix | |